

Development of a Rapid Compression Controlled-Expansion Machine for Chemical Ignition Studies

John Neuman
Marquette University

Recommended Citation

Neuman, John, "Development of a Rapid Compression Controlled-Expansion Machine for Chemical Ignition Studies" (2015).
Master's Theses (2009 -). Paper 290.
http://epublications.marquette.edu/theses_open/290

DEVELOPMENT OF A RAPID COMPRESSION CONTROLLED-EXPANSION
MACHINE FOR CHEMICAL IGNITION STUDIES

by

John Neuman, B.S.M.E.

A Thesis submitted to the Faculty of the Graduate School,
Marquette University,
in Partial Fulfillment of the Requirements for
the Degree of Master of Science

Milwaukee, Wisconsin

May 2015

ABSTRACT
DEVELOPMENT OF A RAPID COMPRESSION CONTROLLED-EXPANSION
MACHINE FOR CHEMICAL IGNITION STUDIES

John Neuman, B.S.M.E.

Marquette University, 2015

The ability to accurately model fuel combustion processes is essential to the development of transportation, power generation, and manufacturing technology. Models describing the kinetics of chemical oxidation are readily available and highly refined for a wide range of test fuels. However, these models still suffer from high levels of uncertainty under engine-relevant conditions, largely due to a lack of consistency between published validation data.

An experimental testing apparatus, known as the Rapid Compression Controlled-Expansion Machine (RCCEM) has been designed and fabricated to conduct chemical kinetic studies. The RCCEM features a pneumatically-driven, custom-designed cam, which governs the volumetric compression and expansion of the combustion chamber. This machine has been designed to test various compression ratios, compressed pressures, and compressed temperatures. Central to the operation of the RCCEM, the cam assembly is modular with the ability to incorporate different cams with unique compression and expansion profiles. This capability is intended to control heat loss rates in experiments via volumetric expansion, and as a result, increase understanding of its influence on the interpretation of validation data. Performance characterization of the RCCEM, using *iso*-octane and hexane, has shown that the machine is capable of testing a wide range of conditions with exceptional repeatability. Ignition delay times for *iso*-octane are reported for compressed temperatures of 630-700 K.

Additionally, two computational fluid dynamics (CFD) studies have been conducted to investigate the role of non-uniform boundary temperatures as a potential cause of discrepancies among data in the literature. The effect of these boundary conditions on ignition delay time predictions and compressed-gas temperature field development has been investigated for heated RCM experiments that use either creviced or flat pistons. Three unique boundary temperature cases for non-reactive simulations showed that a large temperature gradient forms over the crown of the piston due to heterogeneities present in the initial temperature fields. Subsequently, five boundary temperature cases were investigated for reactive simulations and demonstrated the effect of these non-uniformities on ignition delay time predictions. Through this work, it was determined that the flat piston is susceptible to these non-uniform conditions causing discrepancies in ignition delay times, whereas the creviced piston data was only minimally influenced.

ACKNOWLEDGEMENTS

John Neuman, B.S.M.E.

I would like to express my sincerest gratitude to my thesis advisor, Dr. Casey Allen, who has provided me with all of the necessary tools to successfully complete this work. Without your patience, guidance, and trust, I am sure that I could not have succeeded. I thoroughly enjoyed our constant communication and greatly appreciated the support you gave me through the occasional mishap in the lab. When I first arrived, the lab was empty—it's amazing to see how far it has come. Thank you for the opportunity to help you establish your research at Marquette. I wish you and your research group the very best—I think you have a bright future ahead of you. Although we did not get the chance to do all that we originally set out to do, I hope that, at the very least, our work can be used as a basis to put Marquette on the map in fundamental combustion research.

I would also like to express my gratitude to my thesis committee members, Dr. John Borg and Dr. Margaret Mathison. Thank you for all that you have taught me in the classroom; these were some of the most enjoyable classes I have ever taken.

Thank you to my wonderful girlfriend, Lacey. You have supported me relentlessly and pushed me to always give 100 percent. Thank you to my family, particularly for instilling a work ethic and attention to detail in me that has helped immensely over the past two years and will continue to benefit me for the rest of my life. Thank you to the Bowens for all of your support; it has been such a pleasure to get to know you all over the past few years. Thank you to my dear friend, Benyamin Davaji, for teaching me how to be a graduate student and making the office such an enjoyable place to be.

Thank you to all of the members of our research group: David Wilson, Caroline Villa, and Jack Rehn, for allowing me to pass some of my knowledge on, as well as your help in different aspects of the RCCEM design. I wish you all the best.

Thank you to the machinists at Southeast Tool and Die, Senk Tooling, and in the DLC machine shop for all of your help in fabricating the parts for the RCCEM. Thank you to Annette Wolak for all of your help in ordering and receiving my parts; your assistance has been invaluable.

TABLE OF CONTENTS

ACKNOWLEDGEMENTS	i
LIST OF TABLES	vi
LIST OF FIGURES	vii
Chapter 1 Introduction.....	1
1.1 Background and Motivation.....	1
1.1.1 Chemical Kinetic Studies.....	1
1.1.2 Overview of a Rapid Compression Machine	3
1.2 Specific Objectives and Scope of Study	7
1.3 Structure of the Thesis.....	8
Chapter 2 Experimental Facility.....	10
2.1 Traditional RCM Design.....	10
2.2 Rapid Compression Controlled-Expansion Machine	11
2.2.1 Overview.....	11
2.2.2 RCCEM Design	13
2.2.2.1 Table	13
2.2.2.2 Cam Profile.....	14
2.2.2.3 Pneumatic Actuator	16
2.2.2.4 Hydraulic Brake Mechanism.....	17
2.2.2.5 Combustion Chamber	19
2.2.2.6 Safety Shield.....	23
2.2.2.7 Design Summary	24
2.2.3 RCCEM Operation and Experimental Procedure	25

2.2.3.1	Test Initialization	25
2.2.3.2	Test Execution and Data Acquisition	28
2.2.4	Numerical Model	30
2.3	Summary	34
Chapter 3	RCCEM Characterization	36
3.1	Non-Reactive Experiments	36
3.1.1	Overview	36
3.1.2	Test Setup & Procedure	36
3.1.3	Results	37
3.1.3.1	Pressure Data	37
3.1.3.2	Repeatability	38
3.1.3.3	Heat Loss Characterization	39
3.1.3.4	Driving Pressure	41
3.1.3.5	Comparison to Modeled Results	43
3.2	Reactive Experiments	45
3.2.1	Overview	45
3.2.2	Test Setup & Procedure	46
3.2.2.1	Combustion Chamber Volume	46
3.2.3	Results	47
3.2.3.1	Pressure Data	47
3.2.3.2	Repeatability	49
3.2.3.3	Effect of Equivalence Ratio	50
3.2.3.4	Ignition Delay Times for iso-Octane	51

3.3	Summary	52
Chapter 4	Numerical Study of Non-Uniform Boundary Temperatures in RCMs.....	53
4.1	Background	54
4.2	The Effect of Non-Uniform Boundary Conditions on Temperature Field Development within Heated Rapid Compression Machine Experiments.....	55
4.2.1	CFD Setup/Numerical Specifications	55
4.2.2	Results.....	59
4.2.2.1	Steady State Simulations	59
4.2.2.2	Transient Simulations	59
4.2.3	Conclusions.....	70
4.3	The Effect of Non-Uniform Boundary Conditions on Ignition Delay Time Measurements from Heated Rapid Compression Machine Experiments.....	70
4.3.1	Overview.....	70
4.3.2	CFD Set-Up/Numerical Specifications.....	72
4.3.3	Results.....	75
4.3.4	Conclusions.....	82
4.4	Summary	83
Chapter 5	Summary & Future Work	85
5.1	Summary	85
5.2	Future Work	86
	BIBLIOGRAPHY.....	88
	Appendix A: RCCEM Numerical Model	90
	Appendix B: CFD Simulation Ignition Delay Time Script	99

Appendix C: Script to Determine Ignition Delay Time from RCCEM Data 102

LIST OF TABLES

Table 2-1: RCCEM Operating Characteristics	24
Table 2-2: Kistler 5010b Dual Mode Charge Amplifier settings.	29
Table 2-3: Model parameters, boundary, and initial conditions used in the model described in this section.	33
Table 3-1: Summary of test conditions for comparison to RCCEM model.	44
Table 3-2: List of compression ratios and initial volumes for certain distances between the cam follower clevis and the cylinder sleeve.	47

LIST OF FIGURES

Figure 1-1: Sample pressure trace for a reactive and non-reactive RCM experiment. Solid line represents the pressure for a reactive experiments and dashed line represents inert non-reactive experiment.	4
Figure 2-1: RCCEM Schematics: (a) Top-down view of the RCCEM solid model. (b) RCCEM solid model shown with safety shield.	12
Figure 2-2: Photo of the developed RCCEM setup located in the Engines Observatory Lab at Marquette University.	14
Figure 2-3: Schematic illustrating the key features of the cam. The compression and expansion portion of the profile is shown in blue.	15
Figure 2-4: Schematic of the hydraulic braking mechanism.	18
Figure 2-5: Exploded view of the hydraulic interference piston assembly.	19
Figure 2-6: Cross-section view of the cylinder head showing the ports for instrumentation and test initialization.	20
Figure 2-7: Cross section of the entire combustion chamber and cylinder sleeve assembly. The cylinder sleeve supports are fastened to the dual-carriage slide which attaches to the combustion chamber table.	21
Figure 2-8: Exploded, cross section schematic of the three piece creviced piston assembly.	23
Figure 2-9: The RCCEM Charge Preparation VI front panel. The static pressure is monitored along with temperature to initialize the combustion chamber prior to a test.	26

Figure 2-10: Fuel injector calibration setup (left) and calibration curve for hexane (right). Three measurements are taken for each pulse width.	29
Figure 2-11: The RCCEM VI front panel, which is used to start a test and record pressure data for the duration of the experiment.	30
Figure 2-12: Temperature and pressure traces for a reactive and non-reactive simulation using the numerical model. Pressure and temperature drop throughout post-compression is directly influenced by the trajectory of the cam profile.	34
Figure 3-1: The pressure trace for a non-reactive experiment for air with an initial pressure, $P_1 = 1.1$ bar.	38
Figure 3-2: Four non-reactive pressure traces for initial pressures of 1.0 and 2.0 bar. Repeatability is demonstrated as the data overlay exactly for each respective test.	39
Figure 3-3: Pressure drop rate during the expansion period for a range of compression ratios of 6 - 16. The shaded region resides between initial pressures of 1.0 bar and 2.0 bar. Compressed pressures range from 9.5 bar to 55 bar.	40
Figure 3-4: Non-reactive pressure plot for an experiment with excessive driving force. The cam follower leaves the cam surface and rebounds causing a spike in pressure.	42
Figure 3-5: Contour plot of the driving pressure as a function of the compressed pressure and initial pressure. The line indicates the cutoff for driving pressures that cause the follower to skip off of the cam surface.	43
Figure 3-6: Comparison of non-reactive experiment to numerical model of the RCCEM. The dashed line represents fully adiabatic compression and expansion.	

Throughout post-compression, the dashed line pressure decreases only due to volumetric expansion.	45
Figure 3-7: Pressure trace for a reactive experiment with Hexane. Three pressure rises are seen here: the first is due to compression, the second is first-stage ignition, and the third is second-stage ignition.	48
Figure 3-8: Plot illustrating the difference in the pressure trace for a reactive for iso-octane and a non-reactive experiment under similar test conditions for air.	49
Figure 3-9: Pressure traces for five reactive tests with iso-octane at an equivalence ratio of 0.5. First and second stage ignition are shown to be repeatable.	50
Figure 3-10: The effect of varying equivalence ratio on the pressure for iso-octane. Compressed temperatures vary due to change in gas composition, T_c ranges from 637 K to 678 K. $P_c = 24$ bar.	51
Figure 3-11: Ignition delay times for iso-octane at a compressed pressure, $P_c = 30$ bar, and equivalence ratio, $\Phi = 0.7$, for a compressed temperature range, $T_c = 634 - 694$ K.	52
Figure 4-1: CFD mesh at $t = 15$ ms after the start of compression.	55
Figure 4-2: Description of initial temperature fields (K) for simulation cases: (a) uniform boundary temperatures, (b) piston 25 K cooler, (c) piston 50 K cooler.	57
Figure 4-3: Temperature field calculations (K) in post-compression interval for initial condition case (a) with $T_c = 808$ K and $p_c = 11.23$ bar.	64
Figure 4-4: Temperature field calculations (K) in post-compression interval for initial condition case (b) with $T_c = 808$ K and $p_c = 11.23$ bar.	65

Figure 4-5: Temperature field calculations (K) in post-compression interval for initial condition case (c) with $T_c = 808$ K and $p_c = 11.23$ bar.....	66
Figure 4-6: Temperature field calculations (K) in post-compression interval for initial condition case (a) with $T_c = 808$ K and $p_c = 23.34$ bar.....	67
Figure 4-7: Temperature field calculations (K) in post-compression interval for initial condition case (b) with $T_c = 808$ K and $p_c = 23.34$ bar.	68
Figure 4-8: Temperature field calculations (K) in post-compression interval for initial condition case (c) with $T_c = 808$ K and $p_c = 23.34$ bar.....	69
Figure 4-9: Sector geometries for: (a) flat piston, (b) creviced piston, and (c) the computational domain for creviced piston showing the orthogonal grid.	71
Figure 4-10: Initial temperature fields for the simulation cases: (a) uniform boundary temperatures, (b) “cool” piston temperatures, (c) “cool” piston with wall boundary temperature gradient.	73
Figure 4-11: Ignition delay times determined for each initial temperature field with $P_c = 7$ bar for the flat piston.....	76
Figure 4-12: Compressed temperature field and selected species mass fractions at $t = 0$ (TDC) and 40 ms ATDC for uniform and 50 K/wall gradient boundary temperature case with $T_c = 753$ K with the flat piston.	78
Figure 4-13: Ignition delay times determined for each initial temperature field with $P_c = 7$ bar for the crevice piston geometry.	79
Figure 4-14: Compressed temperature field and selected species mass fractions at $t = 0$ (TDC) and 40 ms ATDC for the uniform and 50 K/wall gradient boundary temperature cases with $T_c = 753$ K with the creviced piston.	80

Chapter 1 Introduction

1.1 Background and Motivation

1.1.1 Chemical Kinetic Studies

Detailed Kinetic Models (DKMs) describe the dynamic evolution of a chemically reactive system. These models contain pertinent chemical species and elementary reaction pathways for describing and modeling fuel oxidation. Ignition delay time measurements, speciation data, and optical diagnostics are directly used to improve the capabilities of chemical kinetic modeling by providing reliable experimental data that characterize combustion processes. On a global level, ignition delay times are used to validate these chemical kinetic models. Poor agreement between experimentally determined ignition delay time measurements and numerical model results require further refinement of the mechanism and an evaluation of specific elementary reactions. Highly refined DKMs are useful when incorporated into simulations of low complexity, *i.e.*, zero-dimensional models, or even highly complex three-dimensional computational fluid dynamic (CFD) simulations to provide reliable, predictive modeling used for the advancement of transportation, power generation, and manufacturing technologies.

Experimental facilities used to collect data to validate DKMs often encounter issues due to uncertainty in measurements, poor characterization of experimental conditions, and realities that are challenging to directly measure or understand. A Rapid Compression Machine (RCM) is one such device. RCMs are fundamental reactors which are used to recreate internal combustion engine conditions in a clean, controlled environment. For RCM data to be useful, it is essential to create a thermodynamically

well-defined environment to accurately characterize an experiment. Under ideal conditions, ignition delay measurements could be performed in a quiescent, homogeneous gas phase mixture that is instantaneously compressed to a repeatable, specified reaction condition, whereupon the environment would remain isothermal and isobaric until ignition occurs. This ideality cannot be reproduced in practice, especially where low-temperature (600 – 900 K) kinetics are being investigated.

In literature, there are discrepancies among data obtained from different RCM facilities for the same fuels under similar test conditions [Mehl, Curran, Pitz, & Westbrook, 2009; Minetti, Carlier, Ribaucour, Therssen, & Sochet, 1996; Würmel & Simmie, 2005]. These discrepancies are primarily attributed to “facility-dependent” effects such as heat loss to surrounding boundaries, seal leakages, chemical phenomena, or the presence of complex aerodynamics [Mittal & Gupta, 2012; Mittal & Sung, 2006; Sung & Curran, 2014; Würmel & Simmie, 2005]. Inconsistencies in experimental test setup and operation offer a trivial explanation as well. For kineticists, discrepancies in experimental data introduce challenges in selecting proper validation data, as well as in reducing model uncertainties.

Further, a lack of understanding of heat loss effects can greatly influence the interpretation of data obtained from RCMs. Numerical modeling of an assumed “zero-dimensional” system is a valid approach to estimate the temperature trace for an experiment and much work has been done to illustrate this [Mittal & Chomier, 2014; Mittal, Raju, & Sung, 2010; Mittal & Sung, 2007]. Heat loss is included in the zero-D model in one of two ways. One method is by adding a heat loss term into the energy equation, and the other is through adding an effective volumetric expansion. Both of

these methods are tuned to match experimental data (*i.e.*, agreement among pressure drop). However, it is believed that simplifying assumptions used in these analyses limit the ability to accurately represent the physical conditions present in experimentation [Chaos & Dryer, 2010; Goldsborough, Banyon, & Mittal, 2012; Mittal, Raju, & Sung, 2008; Mittal et al., 2010]. In general, a lack of characterization of heat loss present in RCM experiments and inconsistencies in defining experimental conditions lead to an increase in uncertainty in experimental measurements, thus increasing the uncertainty associated with the model validation.

1.1.2 Overview of a Rapid Compression Machine

As described above, an RCM is an excellent tool used for studying autoignition under highly repeatable, well-characterized, and controlled conditions. RCMs are used to directly measure ignition delay times, as well as perform optical diagnostic tests, collect speciation data, and study methods for controlling other autoignition phenomena. An RCM simulates a single compression stroke of an internal combustion engine by rapidly compressing a piston into a cylinder containing a reactive fuel/air mixture. RCMs are typically designed to operate with compression times of 20 to 50 ms, creating an environment with compressed pressures of up to 100 bar and temperatures between 600 - 900 K. The remainder of this section presents a brief description of the data obtained from RCMs and how it is used in fundamental combustion research.

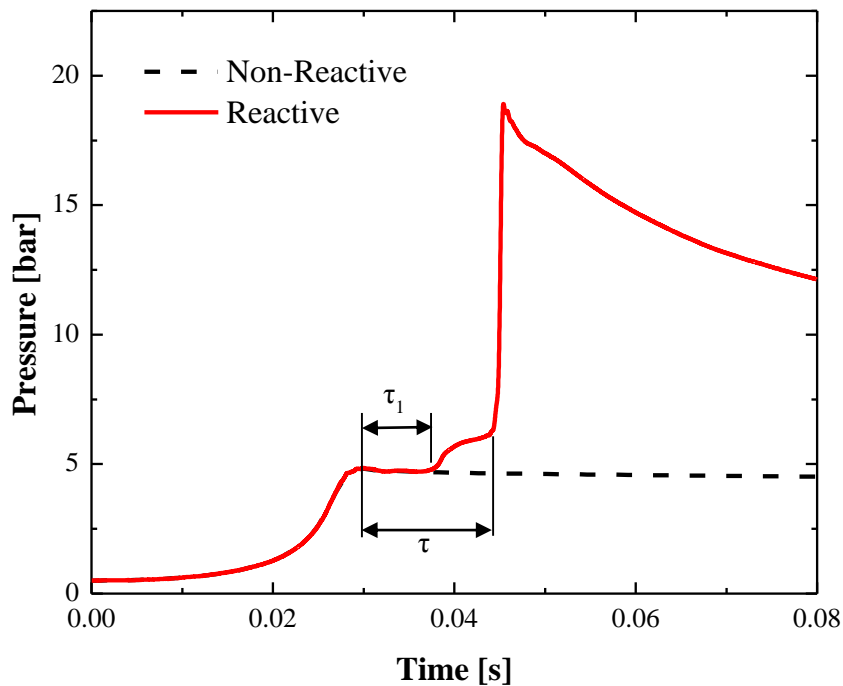


Figure 1-1: Sample pressure trace for a reactive and non-reactive RCM experiment. Solid line represents the pressure for a reactive experiments and dashed line represents inert non-reactive experiment.

Data from an RCM consists of the pressure in the combustion chamber measured over the course of an experiment. A typical pressure trace for a non-reactive and reactive experiment is given in Figure 1-1. The dashed line is the data for a non-reactive experiment, which shows an increase in pressure due to compression and a gradual pressure drop over the post-compression period. This pressure drop is primarily attributed to heat loss to the surrounding boundaries, although seal leakages can contribute as well. The solid line is the pressure trace for a reactive experiment. The compressed pressure, P_c , (*i.e.*, the pressure at the end of compression) is the same for both experiments. Heat release due to ignition causes a second spike in pressure in the reactive experiment. Ignition delay times are calculated as the time from the pressure inflection point,

indicating where the piston has reached top dead center (TDC), to the time at which ignition occurs (see Figure 1-1). First-stage ignition is represented by τ_1 and the total ignition delay time by τ .

Temperature is challenging to measure directly in RCMs because the response times of temperature reading instruments (*i.e.*, resistance temperature devices (RTD) or thermocouples) does not allow the change in temperature to be recorded in real time. Therefore, the compressed temperature is estimated using isentropic relations. Non-reactive pressure traces are used under the adiabatic core assumption to approximate heat loss by using an “effective volume” approach, e.g. [Sung & Curran, 2014; Tanaka, Ayala, & Keck, 2003] and can allow for the temperature over the course of the experiment to be approximated. Accurately determining the temperature within the combustion chamber at TDC is of utmost importance in properly characterizing a fuel. Ignition delay times are reported as a function of the compressed temperature (T_c) *i.e.*, the temperature at the end of compression.

In summary, an ideal RCM facility must have the capability to test with fast compression times over a range of compression ratios while collecting pressure data and providing optical access and gas sampling as well. A more detailed overview of the use of RCMs for chemical ignition studies is given by Sung and Curran [Sung & Curran, 2014].

In order to alleviate some of the issues described in section 1.1.1, some RCMs have been redesigned to offer more control over experimental conditions. The idea behind these machines is to better understand different phenomena associated with the operation of internal combustion engines. While these are also fundamental reactors, the

data obtained from them incorporate more of the transport processes that are present in engines.

One such machine is the University of British Columbia, Rapid Intake and Compression Machine (RICM), which can account for the flow field introduced by induction in an internal combustion engine prior to the compression stroke [Dohring, 1986].

Another machine is the Rapid Intake, Compression and Expansion Machine (RICEM) at the Korea Advanced Institute of Science and Technology, which has adapted a traditional RCM with a gas supply system and expansion that can be used to account for the fluid mechanics associated with the induction and power stroke in an internal combustion engine [Cho, Jeong, Moon, & Bae, 2010].

The Rapid Compression Expansion Machine (RCEM) at the Tokyo Institute of Technology can simulate intake, compression, expansion and exhaust strokes of a single cylinder engine using hydraulic actuation [Kobori & Kamimoto, 1995]. This machine uses a spool valve operating mechanism which allows for either intake and compression or compression and exhaust to be tested.

Another unique RCEM design exists at Pohang University of Science and Technology [Park, Huh, & Park, 2000]; this machine operates like a single-cylinder internal combustion engine with a crankshaft that rotates at a constant speed. This machine is capable of simulating a four-cycle internal combustion engine while also suppressing most of the turbulence present in the combustion chamber.

Overall, the evolution of RCMs and the development of new machines capable of increased control over experimental conditions are essential to the refinement of

combustion modeling processes. The field of chemical kinetics relies heavily on data collected from these machines for validation purposes.

1.2 Specific Objectives and Scope of Study

The objectives of this work are motivated by the desire to increase the understanding of causes for discrepancies between data obtained from different RCMs. The work presented here aims to influence this goal by addressing the following objectives.

Specifically, the main portion of this work is to design, fabricate and characterize a device capable of performing chemical ignition studies over a large range of highly-controlled experimental test conditions. This machine will be referred to as the Rapid Compression Controlled-Expansion Machine (RCCEM). The RCCEM will have the capability to control experimental conditions throughout post-compression, measure ignition delay times, provide optical access, enable rapid gas sampling, and operate with quick compression times.

Characterization of the RCCEM will outline the performance characteristics, as well as establish a range of operating conditions that can be used to conduct ignition studies of various test fuels. For the characterization, non-reactive experiments will be conducted for the entire range of operating conditions. The characterization will also provide a baseline for the differences in experimental conditions as compared to the traditional RCM facility. Reactive experiments using hexane and *iso*-octane are conducted to establish the capability of the RCCEM to observe autoignition phenomena.

Additionally, the effect of non-uniform boundary temperatures on compressed-gas temperature field development and ignition delay times will be explored for heated

RCM experiments using computational fluid dynamic (CFD) simulations. The objective of this study is to explore non-uniform boundary temperatures as a potential cause of the discrepancies in RCM data found in literature. Non-reactive simulations will be conducted with heterogeneous initial temperature fields to explore the effect on the compressed-gas temperature field development within heated RCM experiments. Reactive simulations under similar initial conditions will be conducted using primary reference fuel (PRF) with an octane number of 65 to explore the effect on ignition delay time measurements.

1.3 Structure of the Thesis

This thesis contains a total of five chapters. A short summary of each of the following chapters is given here.

Chapter 2 provides a detailed description of the RCCEM. The chapter begins with a brief overview of the machine and then works through a description of the design behind each of the components. It provides the details associated with operating and conducting experiments with the RCCEM. The chapter ends by outlining a numerical model created in Matlab, which simulates the machine operation and intended output.

Chapter 3 contains the details of the characterization of the RCCEM. This chapter includes a summary of the operating characteristics of the RCCEM as well as an operating map covering the experimental conditions possible. It ends with a study on the autoignition of iso-octane performed with the RCCEM.

Chapter 4 presents two computational fluid dynamic (CFD) studies conducted for RCMs where the effect of non-uniform boundary temperatures on temperature field development and ignition delay time measurements are explored as possible causes of

discrepancies present in literature. An overview of the studies and background of each is given at the beginning of the chapter, followed by the specific setup for each set of simulations and their respective results and conclusions.

Finally, Chapter 5 summarizes this work and provides suggestions for future developmental work with the RCCEM.

Chapter 2 Experimental Facility

This chapter presents the design and development of the Rapid Compression Controlled-Expansion Machine (RCCEM) which is to be used to conduct experimental chemical kinetic studies. A review of existing machines and numerical modeling work was conducted in order to develop a rapid compression machine facility with all of the capabilities of traditional RCMs as described in Chapter 1, as well as offer the additional capabilities for actively controlling compression and post-compression conditions.

This chapter is organized in the following manner. First, a brief description of existing RCM designs is given. Second, the design of each component in the RCCEM is described. The operating protocol is then discussed. The remainder of the chapter is then dedicated to explaining the numerical model developed to predict the performance of the RCCEM.

2.1 Traditional RCM Design

Traditional RCMs consist of three main components: an actuator, braking mechanism, and combustion chamber. They are often designed with these components oriented in a straight line, concentrically aligned. For actuation, RCMs commonly use compressed air as it is a versatile way to exert large amounts of force and the driving pressure can be easily controlled, allowing various compression times to be tested. A hydraulic brake system is often used to decelerate and stop the combustion piston through controlled venting of hydraulic oil [Affleck & Thomas, 2006; Allen, 2012; Mittal, 2006]. Once the compression stroke ends, the force from the pneumatic actuator holds the combustion chamber at constant volume for the duration of the experiment. The

combustion chamber is usually cylindrical to replicate the geometry of an internal combustion engine and is usually fitted with the following instrumentation for data acquisition: piezoelectric pressure transducer, thermocouple, gas inlet/outlet, and windows.

Two other RCM designs are important to note in light of the RCCEM designed in this work. These are located at the University of Poitiers [Strozzi, Sotton, Mura, & Bellenoue, 2009] and at the University of Science and Technology at Lille [Ribaucour, Minetti, Carlier, & Sochet, 1992]. These RCMs have the actuator and combustion chamber oriented in a right-angle configuration and motion is transmitted through a linear cam mechanism, which ultimately governs the trajectory of the combustion piston. The former is designed with interchangeable cams to operate as an RCM or RCEM.

2.2 Rapid Compression Controlled-Expansion Machine

2.2.1 Overview

A schematic of the RCCEM and a photograph of the experimental setup are presented in Figures 2-1 and 2-2, respectively. The RCCEM incorporates several features from traditional RCMs, but couples them in a unique way to allow for greater control over the post-compression conditions. It is pneumatically-actuated, hydraulically-stopped, and oriented in a right angle, cam-actuated combustion piston configuration similar to the RCMs at Lille [Ribaucour et al., 1992] and Poitiers [Strozzi et al., 2009]. This orientation allows for the stroke and combustion chamber volume trajectory to be changed by using different cams with unique profiles. The cam allows for control over the conditions during compression and throughout post-compression. Only one cam was

fabricated for this work, but the intention is to have different cams made to evaluate different conditions. This cam is designed so that throughout post-compression, the combustion chamber is allowed to undergo a slow, controlled expansion. By slowly expanding the combustion chamber, and through the use of several different cam profiles, it is desired to explore the effects of varying heat loss rates over a large range of test conditions. Another feature unique to the RCCEM is the custom-slide that the combustion chamber assembly is mounted to. This slide is operated by turning a hand wheel and allows the RCCEM to test over a continuous range of compression ratios between 4 and 17.

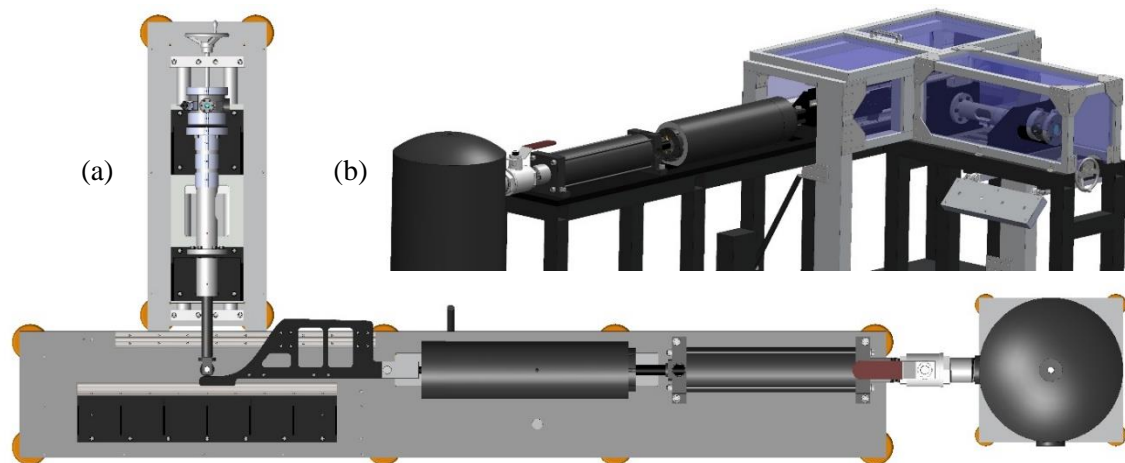


Figure 2-1: RCCEM Schematics: (a) Top-down view of the RCCEM solid model. (b) RCCEM solid model shown with safety shield.

2.2.2 RCCEM Design

2.2.2.1 Table

The table that the RCCEM and all of its components are attached to is made out of 3-inch square tubing with a wall thickness of 0.25 inches. The tubing is 1018 steel and has a black, powder-coated finish. The right angle design of the RCCEM encompasses the integration of two tables, one which holds the driving mechanism and the other which holds the combustion chamber assembly. The overall dimensions of the driving mechanism table are 10 feet long by 15 inches wide. A table top that covers the entire frame is a one inch thick Blanchard ground steel plate. The smaller combustion chamber table is 45 inches in length and 20 inches wide. The two tables are attached by four 9/16-18 bolts. The table assembly is supported twelve 6-inch diameter Mighty-Mount isolating feet which are adjustable to ensure the table is level. A lower level of plates, approximately 9-inches off the ground, are mounted to the frame to hold the hydraulic pump, vacuum pump, and the data acquisition equipment. This table is extremely robust due to its heavy design, which ensures that mechanical vibrations are kept to a minimum.



Figure 2-2: Photo of the developed RCCEM setup located in the Engines Observatory Lab at Marquette University.

2.2.2.2 Cam Profile

The cam profile designed for use in this work consists of a compression and expansion period, which is illustrated in Figure 2-3. The compression period is an 8-inch double-harmonic rise over a period of 10.905 inches, which is coupled to a linear expansion period that drops 0.3 inches over a period of 10.905 inches. This profile was determined through a parametric study using the numerical model explained in section 2.1.4, with the compression ratio and expansion height as the input parameters. The expansion height, 0.3 inches, was chosen to constrain the temperature change drop to approximately 100 K over the entire range of operating conditions. The temperature drop is defined as the difference between the peak compressed temperature at the end of compression and the temperature at the end of the expansion.

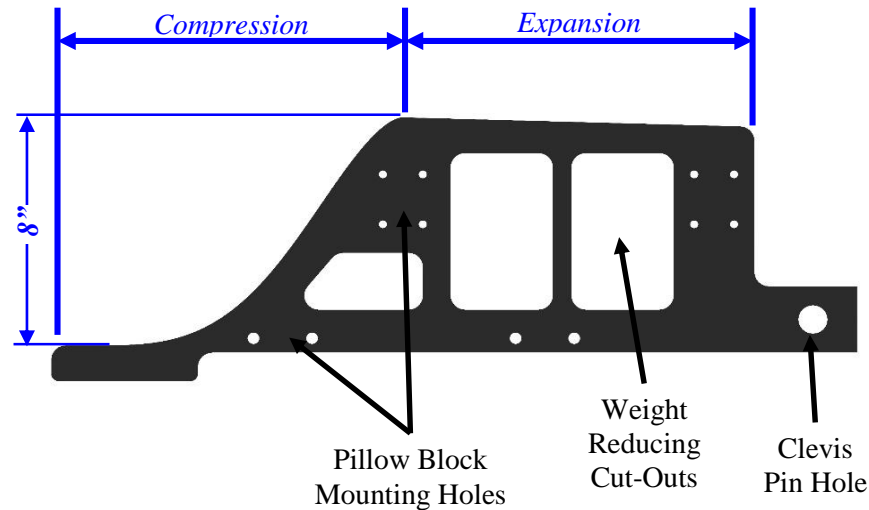


Figure 2-3: Schematic illustrating the key features of the cam. The compression and expansion portion of the profile is shown in blue.

The cam was manufactured by Fox Valley Tool and Die, Inc. and is made of 4140 steel which is ion-nitrided to a Rockwell C hardness of 48-52 and has a black oxide finish. Its overall dimensions are approximately 23 inches long by 9 inches tall and 1.25 inches thick. It weighs approximately 50 pounds. In order to reduce the weight of the cam, several large cut-outs were incorporated into the design. The cam assembly consists of the cam along with four pillow blocks fitted with open-ceramic coated thrust bearings which slide over two $\frac{3}{4}$ -inch diameter 304 stainless steel rods. One rod is mounted to the table perpendicular to the cam's top surface, and the other rod is mounted to a rear support structure oriented perpendicular to the front support. The front support fastens directly into the table top, while the rear support structure, which is made of a 36-inch long, $\frac{1}{2}$ -inch thick steel plate supported by seven $\frac{1}{2}$ -inch thick, 45-degree angle plates. The design of the cam assembly is ideal to prevent any deflection or vibration throughout a large range of operating conditions, as well as to ensure a high degree of reliability. The

cam features an open track, over which a McGill CR-2S cam follower rolls. The follower is held in place by a 0.625-inch diameter pin made of 4340 steel, which is press-fit into a custom clevis that threads directly into the combustion piston rod. The combustion piston rod is 1.375 inches in diameter and is made out of 4340 steel, with a chrome-plated surface. This rod runs through two self-aligning thrust bearings placed in the cylinder sleeve (see Figure 2-6). These ceramic-coated bearings allow for a maximum of 2.5 degrees of deflection during use and were implemented to ensure smooth operation under high dynamic loading. The creviced-piston assembly described later in this section threads directly onto the opposite end of this rod.

2.2.2.3 *Pneumatic Actuator*

Driving the cam assembly is a large-bore, custom pneumatic actuator built by Peninsular Cylinders. This actuator features a 6-inch diameter piston which is capable of producing nearly 8,500 pounds of force at a maximum driving pressure of 300 psi. The driving side of the pneumatic actuator is fitted with a 3-inch NPT port, which connects to a 60-gallon receiver tank by way of a full-port ball valve. The tank was sized in order to maintain more than 95 percent of the driving pressure throughout the entire 22-inch stroke. Driving pressure is set by regulating the building air supply to a value within the operating ranges specified in chapter 4. In order to prevent pressure from building up in the front side of the actuator, three 1-1/2 inch NPT ports were added as vents. These ports are fitted with individual ball valves, which are used to pressurize the front side of the piston in order to retract the RCCEM. The pneumatic actuator drives a rod that is 1.375 inches in diameter and has 3/4-16 internal threads machined into the end.

2.2.2.4 *Hydraulic Brake Mechanism*

In order to decelerate the cam during the expansion period and then stop it at the end of the stroke, an annular flow hydraulic brake mechanism is used. The hydraulic brake mechanism is illustrated in Figure 2-4. The four main components are the hydraulic cylinder, hydraulic interference piston, stroke adjuster, and stopping ring. The cylinder is made of 1018 steel with an outside diameter of 8 inches and an inside diameter which steps from 4 inches down to 3.6 inches. The stepped profile reduces the annular area for oil to flow around the cupped piston, thus substantially decelerating the cam at the end of compression. Figure 2-4 illustrates the location of the stepped profile in regard to the overall stroke. A more detailed illustration of the design of the hydraulic interference piston is also shown in Figure 2-5. The two components of the piston are made out of 1018 steel and follow the design used by Allen at Michigan State University [Allen, 2012]. This piston threads onto a 4-inch long, grade-8 rod with $\frac{3}{4}$ -16 threads and connects both the pneumatic piston rod to the 1-inch diameter 4340 steel rod that attaches to the cam clevis. The two pieces of the piston hold a size -334 O-ring between them which allows the piston to seal against the stroke adjuster when the RCCEM is fully retracted. When the piston is sealed, heavy weight mineral oil is pumped into the cylinder via a manual pump made by Star Hydraulics. This pump is located directly under the cylinder on the lower portion of the table. Hydraulic pressure is then used to balance the force across the hydraulic interference piston prior to a test. Each end of the hydraulic cylinder is sealed via rod wipers and polypaks placed in the stopping ring and stroke adjuster bushings. These bushings are brass and are held in place by six-equally spaced 10-32 screws. Within the stroke adjuster, two $\frac{1}{4}$ -inch NPT ports are placed to clean out

the oil that accumulates when retracting the RCCEM. When retracted, air is forced through the top port and the bottom port drains oil back into the pump reservoir. This introduces a pocket of air to the system once the piston seal is released. To fire the RCCEM, the oil pressure is relieved by a Parker solenoid valve. This allows the driving pressure to break the seal on the hydraulic piston and quickly move the entire assembly. Inside the cylinder, annular flow continues until the cupped piston enters into the stopping ring groove. Once the piston enters the stopping ring groove, the area in contact with hydraulic oil decreases and causes an increase in pressure, which abruptly stops the cam assembly.

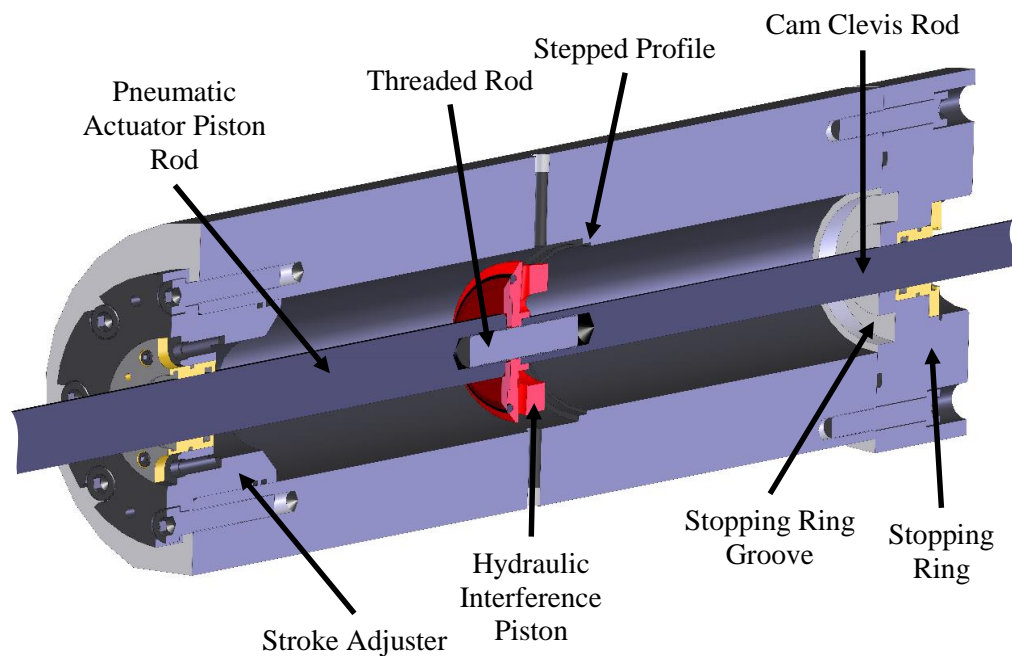


Figure 2-4: Schematic of the hydraulic braking mechanism.

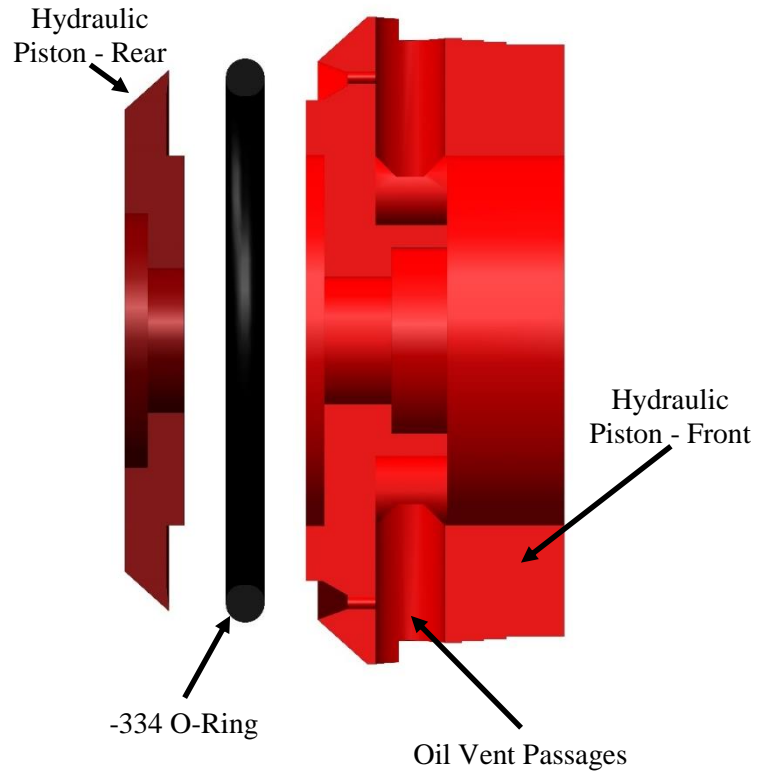


Figure 2-5: Exploded view of the hydraulic interference piston assembly.

2.2.2.5 Combustion Chamber

The combustion chamber is 2 inches in diameter and has a standard clearance height of 0.5 inches. The volume trajectory of the combustion chamber is governed by the cam profile previously described. The cylinder, cylinder sleeve, and head are made of 304 stainless steel, while the creviced-piston assembly is made out of 6061 aluminum.

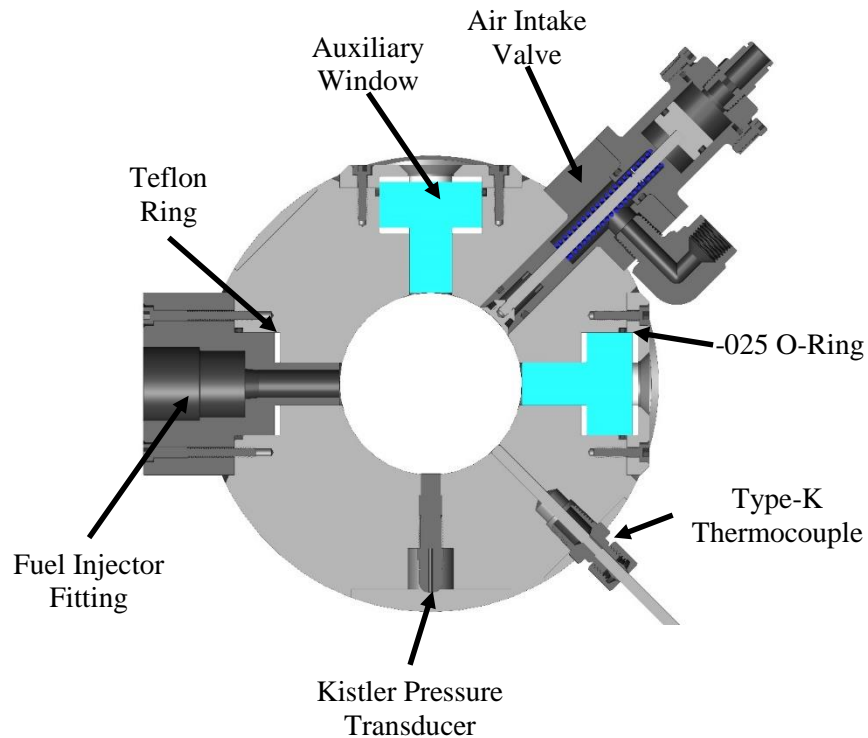


Figure 2-6: Cross-section view of the cylinder head showing the ports for instrumentation and test initialization.

The piston used is a numerically optimized design developed by Mittal and Sung [Mittal & Sung, 2007]. The creviced piston is used to limit adverse fluid dynamics caused by using a flat piston. With a flat piston, cool boundary layer gases shear off the cylinder wall during compression, thus creating a roll-up vortex which flows over the crown of the piston and introduces heterogeneities into the compressed temperature field [Mittal & Sung, 2006; Würmel & Simmie, 2005]. The presence of the roll-up vortex introduces error in characterizing experiments because the compressed-gas temperature field becomes non-homogeneous, thus invalidating the adiabatic core hypothesis [Mittal & Chomier, 2014]. An exploded view of this piston design is shown in Figure 2-8. It

consists of three pieces which are designed to hold two polypak ring seals, one facing the cylinder head to seal during compression and the other facing the opposite way to allow for a vacuum seal. The front and rear sections of the creviced piston are sealed using -028 O-rings. This assembly then threads directly onto the combustion piston rod, which allows for the possibility of other piston head designs to be used. To record pressure data, the cylinder head is fitted with a Kistler 603B1 piezoelectric pressure transducer. A thermocouple is used to record the temperature within the combustion chamber prior to a test. A schematic of the cylinder head is shown in Figure 2-7.

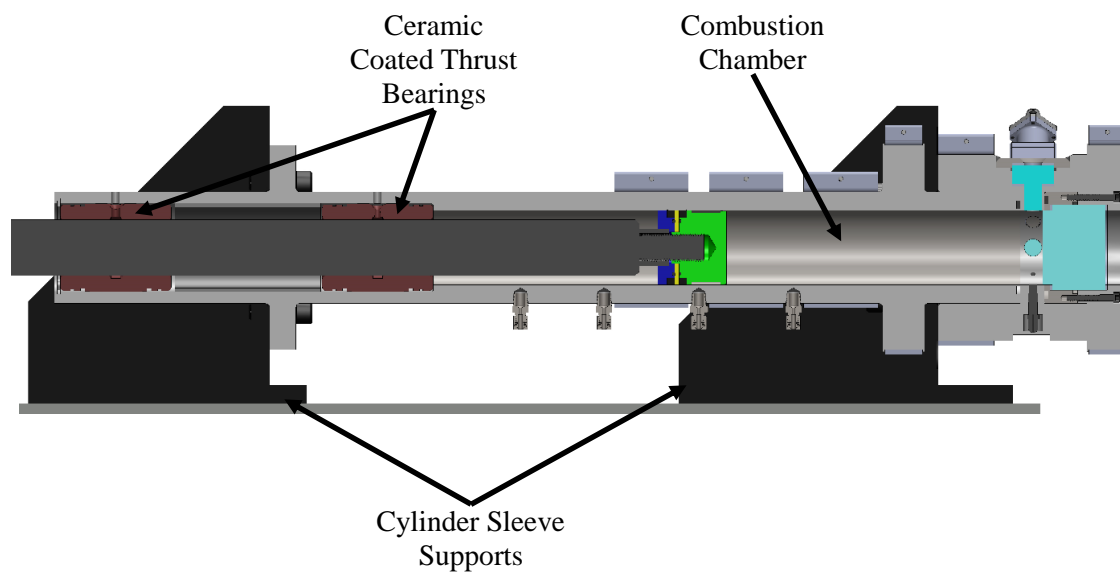


Figure 2-7: Cross section of the entire combustion chamber and cylinder sleeve assembly. The cylinder sleeve supports are fastened to the dual-carriage slide which attaches to the combustion chamber table.

In order to initialize the contents of the combustion chamber when preparing a test, a custom pneumatically-actuated poppet valve has been designed to connect the combustion chamber to a manifold, which holds an Omegadyne PX409 static pressure

transducer and has ports connected to N_2 , O_2 , a vacuum pump, and compressed air. Additionally, four window ports have been designed to allow for optical access to the combustion chamber. These windows are currently replaced with stainless steel plugs, which will be used when optical diagnostics are not being tested. A two-inch wide and four-inch long slot in the side of the combustion chamber is designed to provide further optical access with the use of an optical piston. One of the three auxiliary windows is replaced with a fuel injector to insert precise amounts of fuel into the combustion chamber. The charge preparation approach is known as the Direct Test Chamber (DTC) method, developed by Allen at Michigan State University [Allen, 2012].

Certain fuels with low vapor pressures require heating to volatilize the reactants in the combustion chamber; therefore, the RCCEM was designed to include a feedback-controlled heating system of six resistive band heaters that wrap around the outside of the combustion chamber. Each band heater has its own reference thermocouple embedded into the cylinder sleeve wall. This design is similar to the heating system employed by Allen at Michigan State University [Allen, 2012]; however, it was not used for experiments described in this work.

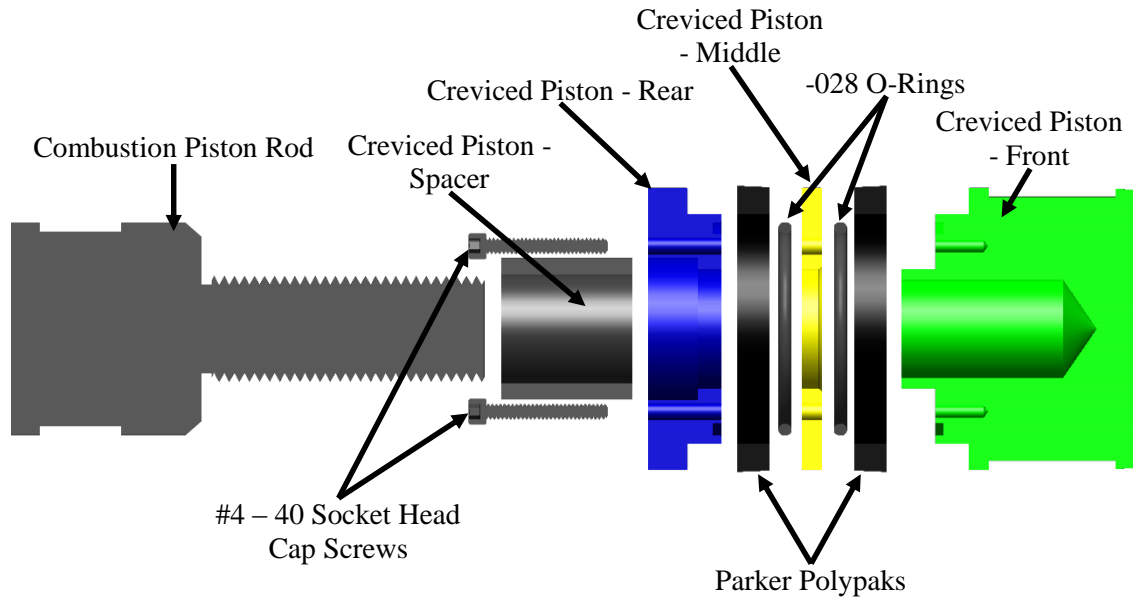


Figure 2-8: Exploded, cross section schematic of the three piece creviced piston assembly.

The RCCEM can operate over a range of compression ratios from 4 to 17. In order to change the compression ratio, the cylinder sleeve assembly is attached to a custom dual-carriage slide built by Generic Slides, Inc., which is actuated by turning a hand wheel. Each full revolution of the hand wheel correlates to 0.25 inches of translation and is fully operational under the safety shield. This allows for the clearance height of the combustion chamber to be changed in between tests, thus controlling the compressed pressure and temperature. This slide enables a continuous set of clearance heights to be tested between 0.5 inches and 1.5 inches.

2.2.2.6 Safety Shield

One extremely important feature of the RCCEM is the safety shield. The frame is built out of 15-series 80/20 aluminum extrusions which fully encase the cam mechanism and combustion chamber. Over the cam mechanism, two doors open up to allow access to

switch out the cam, service the cam follower, and determine the clearance height. On the opposite end of the cam, an Enidine OEMXT 2.0M x 4 shock absorber, capable of absorbing over 15,000 pounds of force, is attached to a ½-inch thick steel plate that is fastened to the aluminum extrusion frame with 32, 5/16-18 screws. The rest of the panels are made of ¼-inch thick Lexan to provide a safe, transparent window to observe the cam mechanism during operation. The combustion chamber table safety shield also has Lexan windows and is equipped with a slot on the control side to allow for the fuel injector to be hooked up to a high-pressure accumulator. The front panel over the combustion chamber has an arc milled in it in order to operate the hand wheel while the combustion chamber safety shield is in place.

2.2.2.7 *Design Summary*

The operating characteristics of the RCCEM are listed in Table 2-1. The RCCEM is designed to enable testing over a large range of experimental conditions. Over the next section, RCCEM testing protocol is outlined for conducting chemical ignition studies.

Table 2-1: RCCEM Operating Characteristics

<i>Cylinder Bore Diameter</i>	2 in
<i>Stroke Length</i>	8 in
<i>Compression Ratio</i>	4 - 17
<i>Clearance Height</i>	0.5 – 1.5 in
<i>Expansion Height</i>	0.3 in
<i>Compression Time</i>	~30-50 ms
<i>Piston Head Configuration</i>	Creved

2.2.3 RCCEM Operation and Experimental Procedure

While the previous section outlined the design of the major components of the RCCEM, this section is focused on describing the testing protocol. The RCCEM is controlled remotely via a computer which is connected to instrumentation and solenoid valves through the use of a National Instruments USB-6353 DAQ. The testing procedure outlined over the remainder of this section is of primary importance to prevent any damage to the RCCEM and its components.

2.2.3.1 Test Initialization

To retract the RCCEM before or after an experiment, each of the three 1-1/2-inch ball valves on the front of the pneumatic cylinder must be closed, as well as the three-inch ball valve on the driving side. The 3/4-inch ball valve on the side of pneumatic cylinder must be opened to remove any pressure on the driving side of the cylinder. Then the front end of the pneumatic cylinder is pressurized by turning the three-way ball valve to the left. Once the cam assembly is retracted over halfway, the combustion chamber must be pressurized to approximately 35 psi. This is accomplished by actuating the air intake valve via the RCCEM Charge Preparation VI and opening the air pressure valve on the control panel. This ensures that the cam follower stays connected to the cam surface over the entire reverse stroke. This will retract the RCCEM until the hydraulic interference piston contacts the stroke adjuster. It is important never to open the air intake valve prior to retracting the cam assembly halfway. Certain test conditions will enable the piston to contact the air intake valve, which will damage the valve stem.

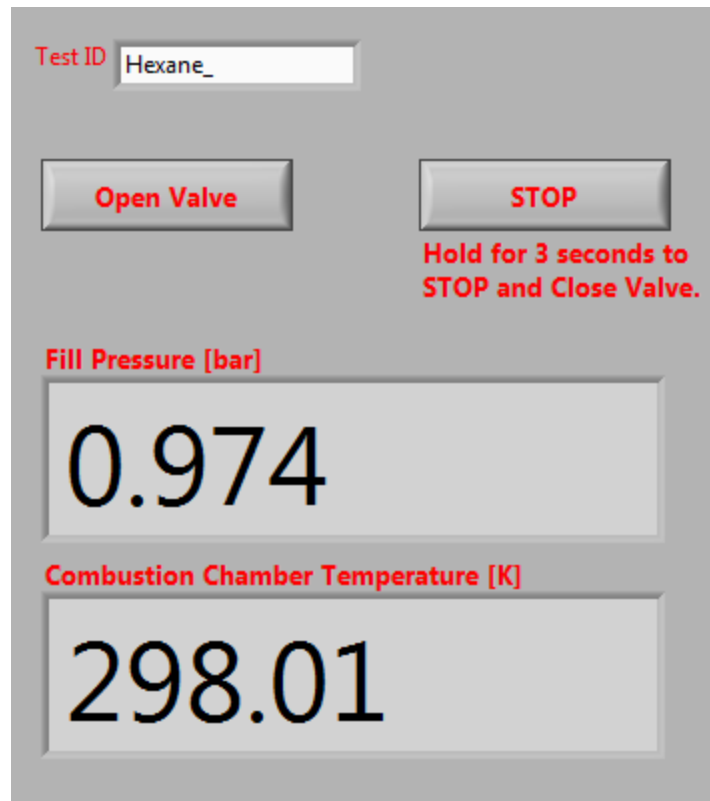


Figure 2-9: The RCCEM Charge Preparation VI front panel. The static pressure is monitored along with temperature to initialize the combustion chamber prior to a test.

Also, the Omegadyne pressure transducer is only rated for 35 psig; therefore, the pressure in the combustion chamber after a test could be high enough to damage the transducer if the air intake valve is opened prior to retracting the cam past halfway.

Next the hydraulic brake is set by operating the manual pump located on the platform below the hydraulic cylinder until the pressure gauge reads approximately 700 psi. Several pumps (~20-25) should be done with the valve on top of the hydraulic cylinder open to remove air from the system. Once the air is removed, the brake can be pressurized. Now the back side of the hydraulic piston must be drained; this is

accomplished by turning the three-way ball valve attached to the front of the air cylinder to the right and listening until air comes out of the vent hole in the oil pump reservoir.

The RCCEM Charge Preparation VI will be used to open the air intake valve. A screen capture of the control panel is shown in Figure 2-9. This VI also monitors the static pressure in the combustion chamber so that specific pressures can be set, and initial conditions are written to a text file located in the RCCEM/Data/Initial Conditions directory. To set the contents of the combustion chamber, the air pressure from retracting the RCCEM can be released by closing the air pressure needle valve on the control panel. The Agilent vacuum pump can be turned on and the vacuum pump needle valve can be opened by turning the handle to the left. Once a vacuum is drawn on the combustion chamber, the vacuum needle valve on the control panel can be closed. Each respective needle valve for the gases located on the control panel are then opened, one at a time, until the specific pressure of each gas is achieved. Once these pressures are set in the combustion chamber, the air intake valve can be closed by holding the stop button for three seconds on the RCCEM VI. The air intake valve must always be closed prior to opening the three-inch driving-pressure ball valve.

Fuel is then added to the combustion chamber through an injection or a series of injections from the fuel injector mounted in the cylinder head. A BMW automotive fuel injector is used. In order to verify the mass of the injection, the fuel injector must be calibrated for each specific test fuel. The calibration correlates the fuel mass injected with a pulse width, which actuates the injector for a set period of time. For each fuel, a calibration curve is created by making a series of injections into a beaker for a range of pulse widths while measuring the mass before and after each injection. The calibration

measurement setup and a calibration curve for hexane is shown in Figure 2-10. Here it can be seen that the fuel mass per pulse is linearly related to the pulse width. As a result, a pulse width and number of injections needed for a specific mass of fuel can be determined. Once the pulse width and number of injections for a specific experiment is determined, National Instruments CalView is used to actuate the fuel injector and inject the mass of fuel into the combustion chamber.

Once the combustion chamber is initialized, the $\frac{3}{4}$ -inch ball valve on the rear of the pneumatic cylinder must be closed and the three-inch ball valve connecting the driving pressure to the pneumatic cylinder is opened. The three 1-1/2-inch ball valves on the front of the cylinder can now be opened to completely arm the RCCEM.

2.2.3.2 Test Execution and Data Acquisition

Once the RCCEM is completely set up for a test, the RCCEM VI (see Figure 2-11) is used to fire and collect pressure data for the duration of the test. The Kistler 603B 1 pressure transducer communicates to the VI through a Kistler 5010B dual mode charge amplifier, which is setup as an analog differential voltage input to the NI-USB 6353 DAQ. The settings on the charge amplifier must be set to the values shown in Table 2-2. After each test, the mode must be set to “Reset” in order to remove the charge build up on the piezoelectric crystals in the transducer.

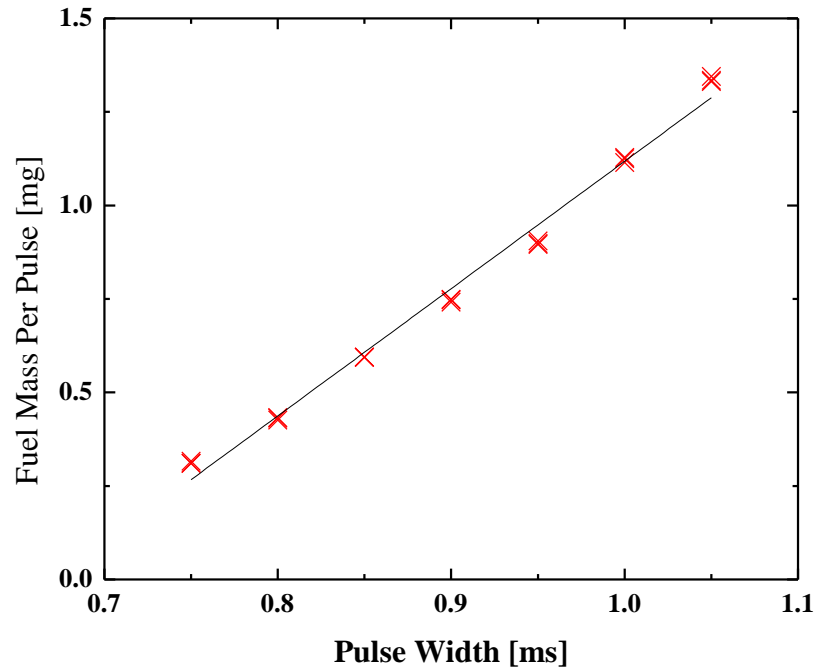


Figure 2-10: Fuel injector calibration setup (left) and calibration curve for hexane (right). Three measurements are taken for each pulse width.

Table 2-2: Kistler 5010b Dual Mode Charge Amplifier settings.

Setting	Value
<i>Mode</i>	Operate (Reset after each test)
<i>Scale</i>	10 bar/volt
<i>Sensitivity</i>	5.37 pC/bar
<i>Time Constant</i>	Long
<i>Input</i>	Charge

Once the RCCEM fire button is pressed, the RCCEM VI energizes the hydraulic solenoid valve and bleeds the pressure from the hydraulic cylinder. The combustion chamber pressure acquisition is triggered off of its own signal, and once a threshold is reached, data is recorded for approximately 0.75 seconds at a rate of 100,000 samples per

second. The pressure data is then written to the specific test text file located in the RCCEM/Data directory.

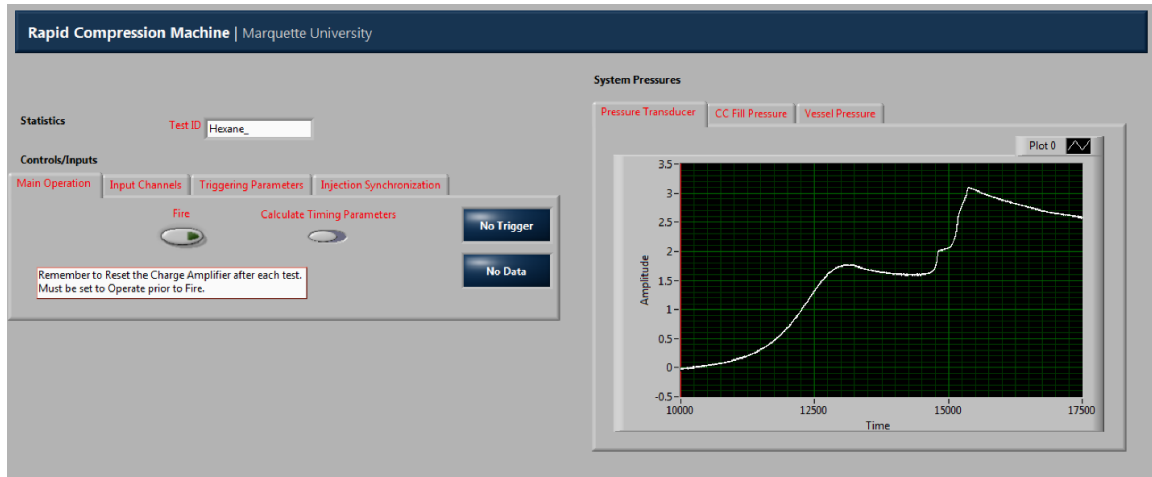


Figure 2-11: The RCCEM VI front panel, which is used to start a test and record pressure data for the duration of the experiment.

2.2.4 Numerical Model

In this section, a numerical model of the RCCEM is described. This model is able to provide an estimate of the performance characteristics of the RCCEM, as well as the intended pressure and temperature trace (see Figure 2-12) for an experiment. Matlab was used to make these calculations over a variety of relevant conditions for the intended operating range, and the script is given in Appendix A.

The model is a force balance on the driving piston assembly, including forces generated by the pneumatic actuator, the pressure change in the hydraulic chamber due to annular flow and incompressibility, and the pressure rise in the combustion chamber transmitted through the cam. The force balance is given in equation 2-1, where F_{air} is the

force generated by the pneumatic piston, F_g is the force due to pressure in the combustion chamber, ϕ is the pressure angle of the cam, and F_{oil} is the force of hydraulic brake mechanism. The mass and acceleration are for the entire piston assembly, including the cam assembly, hydraulic piston assembly, and pneumatic piston rod.

$$\sum F_x = ma = F_{air} - F_g \tan(\phi) - F_{oil} \quad (2-1)$$

Each term in the force balance is determined by an integration of the pressures present in each component over the duration of the experiment. For the hydraulic cylinder, the rate of pressure change in the oil can be determined through the integration of equation 2-2, where V_{oil} is the volume of oil in front of the piston, A_{face} is the area on the leading edge of the hydraulic piston in contact with the oil, v is the velocity of the piston assembly, and P is the pressure of the oil in front of the hydraulic piston. The variables P_o and A_o represent the ambient pressure and the circular area of the hydraulic piston, respectively. The remainder of the terms represent material properties of the oil and are listed in Table 2-3.

$$\frac{dP}{dt} = \frac{-\beta_{oil} C_d A_o}{V_{oil}} \sqrt{\frac{2(P-P_o)}{\rho_{oil}}} + \frac{\beta_{oil} A_{face} v}{V_{oil}} \quad (2-2)$$

For the combustion chamber, the compression and expansion is assumed to be adiabatic and frictionless; therefore, no heat loss is modeled. The pressure change is represented by the differential equation given in equation 2-3, where γ is the ratio of specific heats, V_g is the volume of the combustion chamber, and dQ/dt is the heat release rate.

$$\frac{dP_g}{dt} = -\gamma \frac{P_g}{V_g} \frac{dV_g}{dt} + \frac{\gamma-1}{V_g} \frac{dQ}{dt} \quad (2-3)$$

For simulating combustion, a finite heat release model known as the Wiebe function (equations 2-4 and 2-5) is used [Ferguson & Kirkpatrick, 2001]. To model a non-reactive test, the heating value of the fuel, Q_{in} , is set to zero. Example model output for the combustion chamber temperature and pressure for non-reactive and reactive simulations is shown in Figure 2-12. The dashed line represents a non-reactive simulation while the solid line incorporates heat release.

$$\frac{dQ}{dt} = n_w a_w \frac{Q_{in}}{t_d} (1 - X_b) \left(\frac{t-t_s}{t_d} \right)^{n_w-1} \quad (2-4)$$

$$X_b = 1 - \exp \left(-a_w \left(\frac{t-t_s}{t_d} \right)^{n_w} \right) \quad (2-5)$$

where

X_b = the burned mass fraction

Q_{in} = the heating value input

t = simulation time

t_s = start of combustion

t_d = combustion duration

n_w = Wiebe form factor

a_w = Wiebe efficiency factor

The force due to the pressure in the combustion chamber can be related to the motion of the cam assembly using the cam follower pressure angle, ϕ . The pressure angle is tangent to the face of the cam and represents the direction of the reaction force through the cam follower. The pressure angle can be calculated using equation 2-6 [Norton, 2009] where V_{rfd} is the cam follower velocity, and R_p is the prime radius of the cam profile.

$$\phi = \tan^{-1} \left(\frac{v_{rfd}}{R_p} \right) \quad (2-6)$$

The position of the cam follower with respect to its starting position can be determined using equation 2-7a and 2-7b. Equation 2-7a is the position during the compression stroke of the RCCEM. This portion is a double harmonic rise profile where

Θ and β represent the distance the assembly has traveled and the period of the rise, respectively [Norton, 2009]. Equation 2-7b defines the expansion stroke of the cam profile. The cam follower velocity can then be determined by differentiating the cam follower position with respect to time.

$$s_{rfd} = \frac{h}{2} \left\{ \left[1 - \cos \left(\pi \frac{\theta}{\beta} \right) \right] - \frac{1}{4} \left[1 - \cos \left(2\pi \frac{\theta}{\beta} \right) \right] \right\} \quad (2-7a)$$

$$s_{rfd} = h - 0.0275\theta \quad (2-7b)$$

Table 2-3: Model parameters, boundary, and initial conditions used in the model described in this section.

Parameter	Symbol	Value
<i>Weight of Piston Assembly</i>	-	78 pounds
<i>Ratio of Specific Heats</i>	γ	1.374
<i>Bulk Modulus of Oil</i>	β	232,060 psi
<i>Density of Oil</i>	ρ	0.0345 lb./in ³
<i>Ambient Temperature</i>	T_{amb}	532 °R
<i>Initial Combustion Chamber Pressure</i>	$P_g(1)$	14.7 psi
<i>Initial Combustion Chamber</i>	$T_g(1)$	532 °R
<i>Initial Acceleration</i>	$a(1)$	0 in/s ²
<i>Initial Velocity</i>	$v(1)$	0 in/s
<i>Cam follower Initial Position</i>	$S_{rfd}(1)$	0 in
<i>Cam Follower Initial Velocity</i>	$V_{rfd}(1)$	0 in/s
<i>Initial Pressure Angle</i>	$\emptyset(1)$	0 °
<i>Initial Oil Pressure</i>	$P(1)$	580 psi
<i>Initial Volume of Air Cylinder</i>	$V_{air}(1)$	13,860 in ³

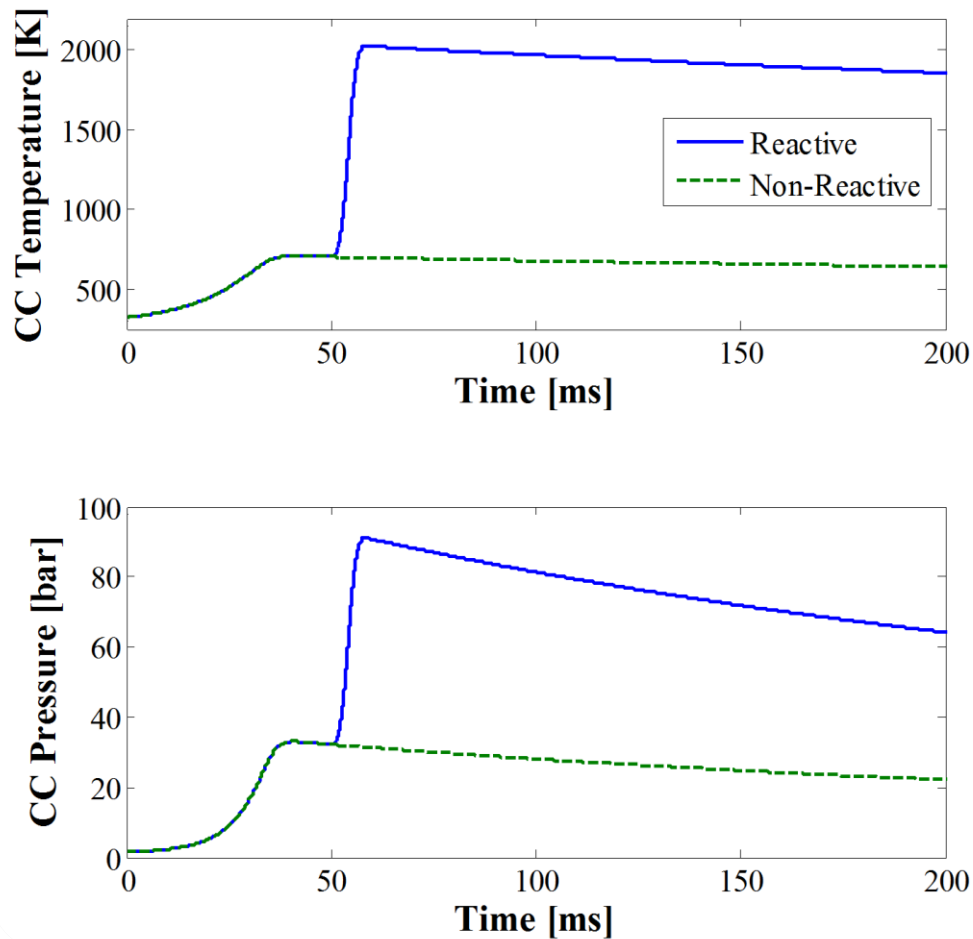


Figure 2-12: Temperature and pressure traces for a reactive and non-reactive simulation using the numerical model. Pressure and temperature drop throughout post-compression is directly influenced by the trajectory of the cam profile.

2.3 Summary

An experimental testing apparatus known as the RCCEM was designed and fabricated to measure ignition delay times for a wide range of test conditions. RCCEM capabilities are summarized by the following characteristics: compression ratios of 4-17, compression times of ~30–50 ms, compressed temperatures between ~600-800 K, and compressed pressure up to 100 bar. This device is intended to be used to experimentally

vary heat loss rates in RCM experiments through the addition of volume expansion during post-compression. The cam used in this work has an expansion height of 0.3 inches, which was designed to constrain the temperature or pressure drop to a specific amount throughout post-compression. The overall cam assembly design is adaptable, which allows for different cams to be used. Cam profiles can range from the traditional RCM volumetric trajectory to any combination of compression and expansion heights to actively control the post-compression conditions.

Testing protocol was established to ensure repeatability, safety, and to prevent damage to any of the RCCEM components. The RCCEM is controlled using the following Labview VIs: RCCEM Charge Preparation VI and RCCEM VI. The RCCEM Charge Preparation VI was created to monitor the pressure inside the combustion chamber while initializing the concentrations of the oxidizer gases in the reaction chamber and to actuate the air intake valve. Subsequently, the RCCEM VI was created to trigger an experiment and collect pressure data for the duration of the test. Using these two VIs, repeatable operation of the RCCEM is possible.

A numerical model of the RCCEM was created to estimate the performance of the RCCEM. The model was used to predict the combustion chamber pressure and temperature over the intended range of operating conditions. Additionally, the model enabled the loading of certain components to be projected, which was useful in performing design calculations and determining a factor of safety for various components. This model will also be used to develop additional cam profiles, allowing for the performance to be estimated prior to physical testing.

Chapter 3 RCCEM Characterization

This chapter presents an overview of the performance and operating characteristics of the RCCEM. Data was obtained from the RCCEM over a wide range of operating conditions for both non-reactive and reactive experiments. Non-reactive experiments are used to understand the test conditions possible with the RCCEM. Additionally, reactive experiments are conducted using hexane and *iso*-octane to show the ability of the RCCEM to perform reactive experiments. Preliminary ignition delay time measurements of *iso*-octane are presented to demonstrate the ability to adequately measure ignition delays with the RCCEM.

3.1 Non-Reactive Experiments

3.1.1 Overview

Prior to performing any reactive experiments in the RCCEM, a number of non-reactive experiments were used to determine the attainable experimental conditions. This section presents a summary of the variety of test conditions attainable in the RCCEM, as well as a description of these conditions and their influence on the experimental data collected from the RCCEM.

3.1.2 Test Setup & Procedure

To initialize the non-reactive experiments reported in this chapter, compressed air was expanded into the combustion chamber with the RCCEM fully retracted. The initial pressure was set by allowing the air pressure to equilibrate to a specific initial pressure with the air-intake valve open. No fuel was injected. The initial temperature and static

pressure were recorded prior to each test, and the dynamic pressure was measured throughout the duration of the experiment.

3.1.3 Results

3.1.3.1 Pressure Data

Data collected from the RCCEM during an experiment is the combustion chamber pressure versus time. Raw data for a non-reactive experiment can be seen in Figure 3-1. Here, time $t = 0$ represents the end of the compression stroke when the piston has reached TDC. Throughout post-compression ($t = 0-150$ ms), the pressure signal is free of any oscillations or disturbances which would cause uncertainty in the pressure measurement. Compression time for the experiment in Figure 3-1 is approximately 34 ms, with the final 50 percent of the pressure rise occurring in approximately 5 ms. Quick compression times are necessary to model the RCCEM compression stroke as a nearly adiabatic process. Compression times range from ~30-50 ms based on the compression ratio and the initial pressure in the combustion chamber.

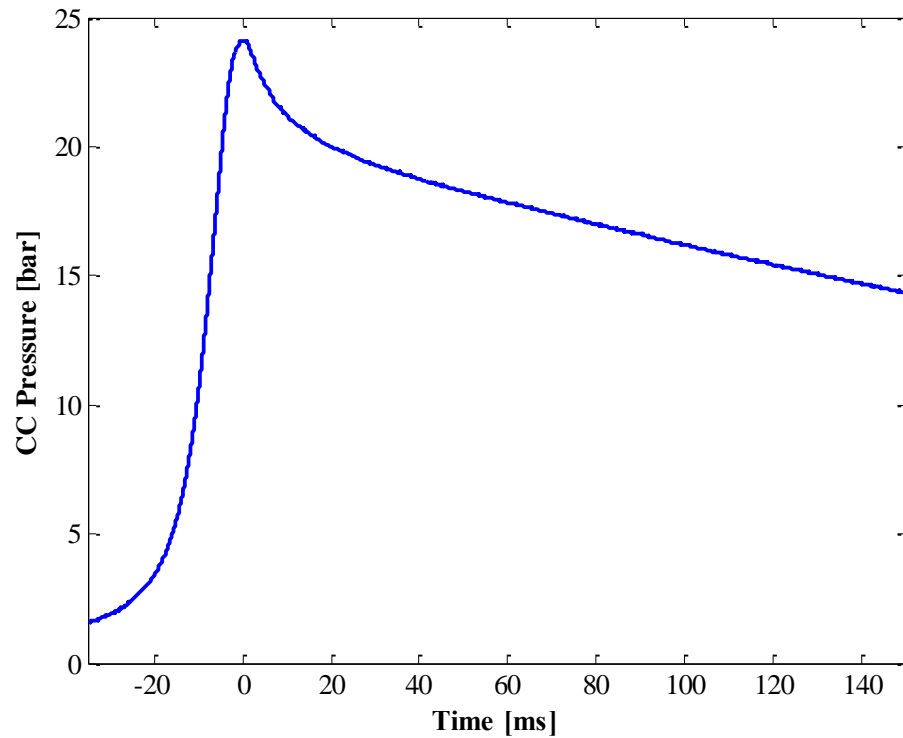


Figure 3-1: The pressure trace for a non-reactive experiment for air with an initial pressure, $P_i = 1.1$ bar.

3.1.3.2 Repeatability

Repeatability at high and low compressed pressures is demonstrated in Figure 3-2. The pressure traces for four experiments at an initial pressure of one bar and four pressure traces for an initial pressure of two bar are shown. These traces directly overlap one another for the entire compression and expansion period. As a result, it is shown that

the RCCEM is capable of creating repeatable experimental conditions over a wide range of pressures.

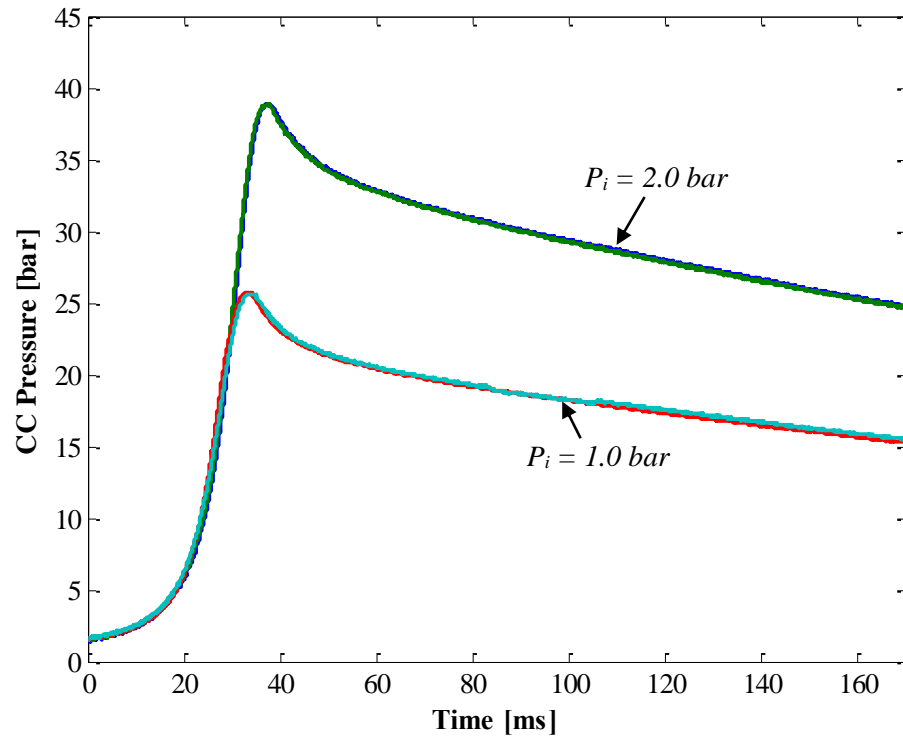


Figure 3-2: Four non-reactive pressure traces for initial pressures of 1.0 and 2.0 bar. Repeatability is demonstrated as the data overlay exactly for each respective test.

3.1.3.3 Heat Loss Characterization

As a proxy to estimate the rate of heat loss throughout post-compression, the average pressure drop rate throughout the expansion period was calculated. A comparison of the pressure drop rates for a range of compression ratios from 6-16 is shown for initial pressures of one and two bar in Figure 3-3. The average pressure drop rate includes both the pressure decrease due to heat loss and the pressure decrease due to volumetric expansion. Two important characteristics of the RCCEM can be identified through the

determination of the average pressure drop rate: (1) the higher the compressed pressure, the higher the pressure drop rate; and (2) the higher the compression ratio, the more influence the volumetric expansion has on the pressure drop. This indicates that any change in initial conditions or compression ratio will influence the pressure drop rate. Because the pressure drop rate lumps the pressure drop due to heat loss and volumetric expansion together, a comparison of the pressure drop rate from the RCCEM for each cam profile to the traditional RCM combustion chamber volume trajectory can be obtained. This comparison can in turn be used to better understand the differences between various RCM facilities.

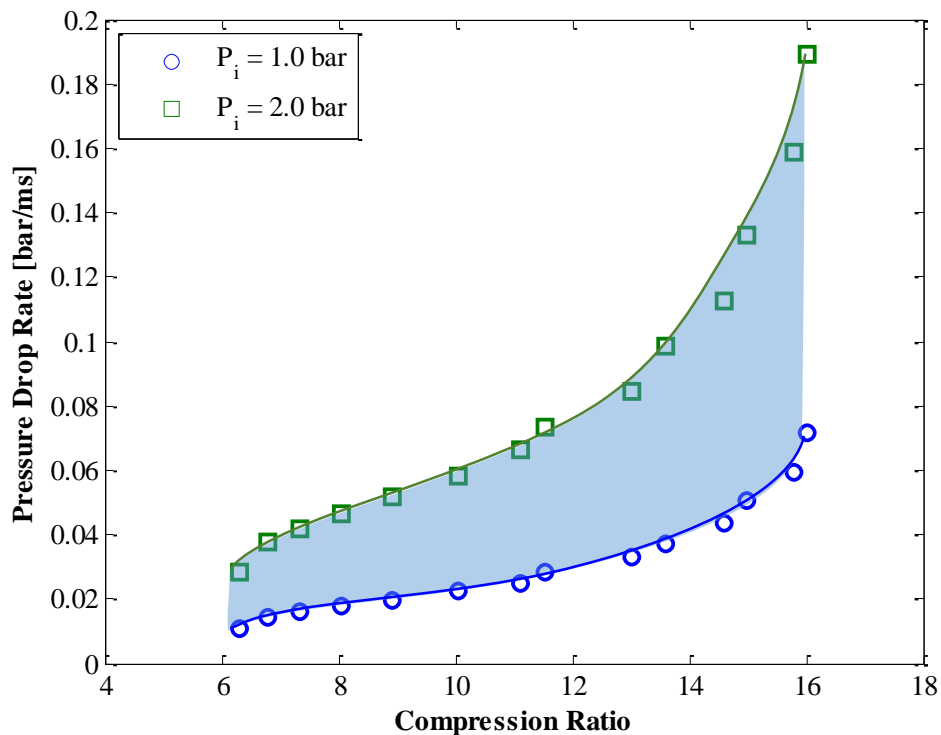


Figure 3-3: Pressure drop rate during the expansion period for a range of compression ratios of 6 - 16. The shaded region resides between initial pressures of 1.0 bar and 2.0 bar. Compressed pressures range from 9.5 bar to 55 bar.

3.1.3.4 Driving Pressure

Because the cam is designed with an open profile, the driving pressure must be regulated to ensure that the follower remains in contact with the cam surface during the transition from compression to expansion. Under certain conditions, the momentum of the combustion piston rod assembly can overcome the force of the compressed gas in the combustion chamber and cause the cam follower to jump off the cam track. Figure 3-4 shows a pressure trace for a test with a driving pressure and combustion chamber pressure mismatch. This pressure trace shows a spike due to the combustion piston rod assembly ramping off the cam surface and compressing farther than intended. The

pressure in the combustion chamber then reaches a point where the force slams the follower back into the cam surface.

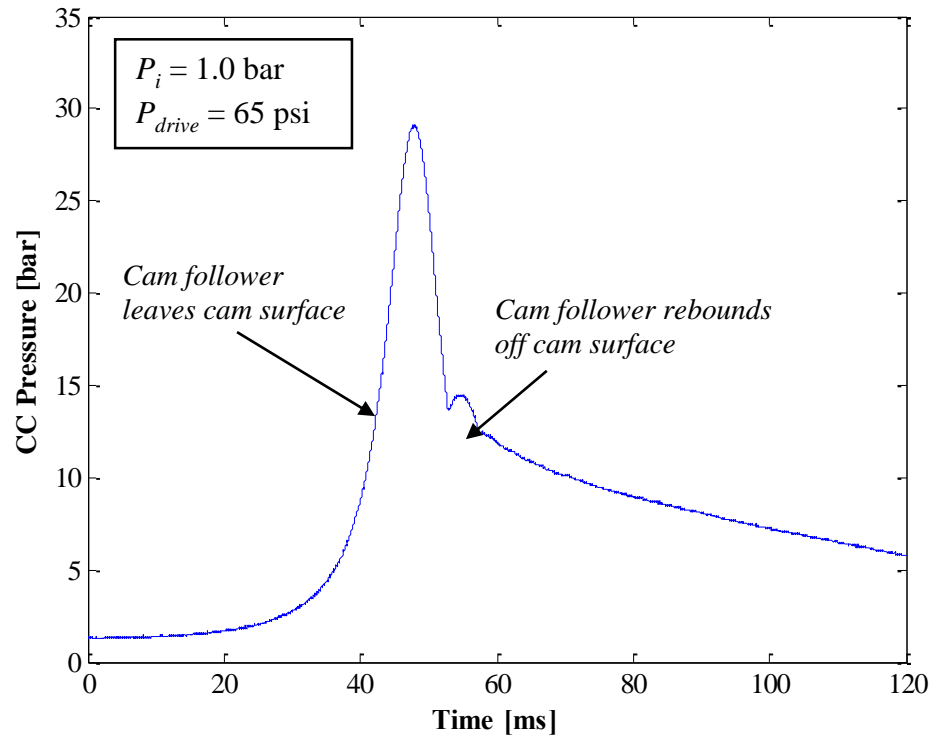


Figure 3-4: Non-reactive pressure plot for an experiment with excessive driving force. The cam follower leaves the cam surface and rebounds causing a spike in pressure.

A smaller pressure increase indicates that the follower contacts the cam surface and rebounds. Experiments where this occur subject the cam surface, cam follower, clevis, and clevis pin to extreme forces which are not intended for regular use. Therefore, to ensure a long life for both the cam follower assembly and cam, the driving pressure must be carefully selected for each respective test. The contour plot shown in Figure 3-5 illustrates the driving pressures that can safely be used for a range of initial and compressed pressures. These driving pressure values should be used conservatively,

approaching the limits incrementally. Additionally, once fuel is injected into the combustion chamber, the initial pressure can vary. This should be taken into consideration when initializing an experiment.

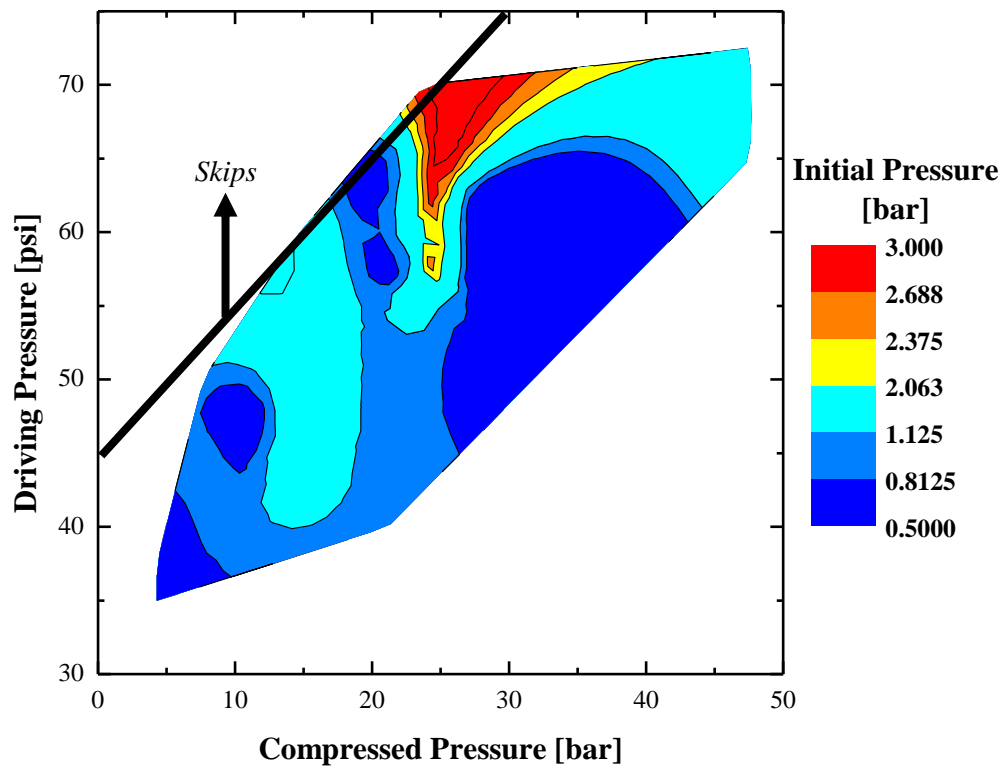


Figure 3-5: Contour plot of the driving pressure as a function of the compressed pressure and initial pressure. The line indicates the cutoff for driving pressures that cause the follower to skip off of the cam surface.

3.1.3.5 Comparison to Modeled Results

A comparison of a non-reactive experiment to the numerical model under similar test conditions is shown in Figure 3-7. The test conditions are summarized in Table 3-1. The dashed line in Figure 3-7 is the pressure trace for the numerical model. As previously

stated, the model neglects heat loss and friction, so the resulting pressure trace represents adiabatic compression and expansion. The shape of the trajectory of the pressure trace for the compression stroke matches well between model and experiment. However, the peak pressure in the experiment is only approximately 63 percent of the peak pressure in the model. During the expansion stroke, the model undergoes a pressure decrease only due to volumetric expansion, whereas in the experiment, the pressure decreases due to heat loss and volumetric expansion. The slope of each pressure trace throughout post-compression is similar; however, as shown above, the rate of pressure decrease is dependent on the compressed pressure. Therefore, the model predicts a slightly quicker pressure decrease rate due to volumetric expansion at that compressed pressure. It is hypothesized that quicker compression times in the experiments would increase agreement for the compression stroke.

Table 3-1: Summary of test conditions for comparison to RCCEM model.

<i>Compression Ratio</i>		10.8
<i>Initial Pressure</i>	P_i	1.0 bar
<i>Initial Temperature</i>	T_i	298 K
<i>Driving Pressure</i>	P_{drive}	55 psi

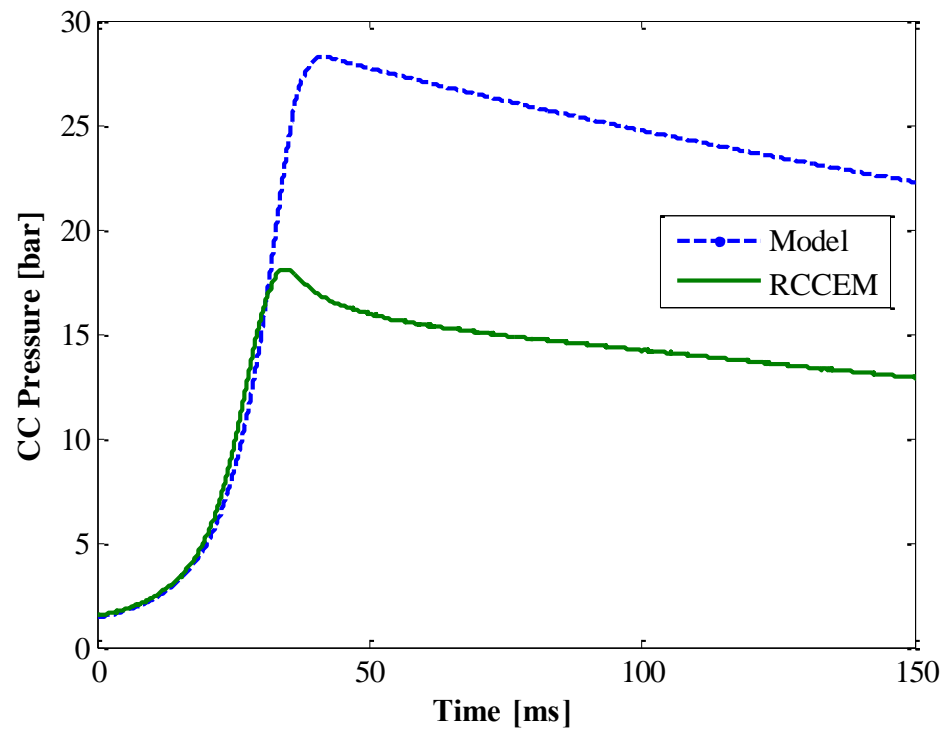


Figure 3-6: Comparison of non-reactive experiment to numerical model of the RCCEM. The dashed line represents fully adiabatic compression and expansion. Throughout post-compression, the dashed line pressure decreases only due to volumetric expansion.

3.2 Reactive Experiments

3.2.1 Overview

Reactive experiments are performed to demonstrate repeatability, as well as the capability of the RCCEM to measure ignition delay times. This section presents the results of reactive experiments for hexane and *iso*-octane. These experiments prove that the RCCEM is capable of experimentally observing autoignition phenomena of chemically reactive gaseous mixtures.

3.2.2 Test Setup & Procedure

Reactive experiments are initialized using the Direct Test Chamber method [Allen, 2012], where a specific mass of fuel is injected directly into the combustion chamber using an automotive fuel injector. Prior to injecting the fuel, the same procedure as in the non-reactive experiments is followed. The air/fuel mixture is established based on the volume and mole fractions of the reactants. A summary of the procedure used to determine the combustion chamber volume is described next.

3.2.2.1 Combustion Chamber Volume

In order to inject the correct amount of fuel into the combustion chamber for a reactive experiment, the volume of the combustion chamber must be determined. This is accomplished using the ideal gas equation of state (equation 3-1), where P is the pressure, V is the volume, n is the number of moles, R_u is the universal gas constant, and T is the temperature. By measuring the static pressure using the Omegadyne transducer for the reaction chamber at two different volumes, the initial volume can be calculated.

$$PV = nR_uT \quad (3-1)$$

An accurate determination of the volume is essential to perform reactive experiments at specific air/fuel ratios. Additionally, the volume can be used to calculate the specific geometric compression ratio, and as a result, the non-adiabaticity of the RCCEM can be approximated. The compression ratios are listed in Table 3-2. Here, the compression ratio and volume at BDC are listed as a function of the distance from the end of the cylinder sleeve to the cam follower clevis. The information in this table can be used to accurately initialize reactive experiments.

Table 3-2: List of compression ratios and initial volumes for certain distances between the cam follower clevis and the cylinder sleeve.

Distance (Clevis to Cylinder Sleeve) [in]	Volume at BDC [m ³]	Compression Ratio
8.375	4.38E-04	16.71
8.399	4.39E-04	16.01
8.413	4.40E-04	15.62
8.432	4.41E-04	15.12
8.452	4.42E-04	14.64
8.490	4.44E-04	13.81
8.500	4.45E-04	13.61
8.529	4.46E-04	13.06
8.567	4.48E-04	12.41
8.606	4.50E-04	11.81
8.683	4.54E-04	10.79
8.800	4.60E-04	9.56
9.000	4.70E-04	8.05
9.125	4.77E-04	7.35
9.250	4.83E-04	6.78
9.375	4.90E-04	6.30
9.500	4.96E-04	5.89
9.625	5.02E-04	5.55
9.750	5.09E-04	5.25
9.875	5.15E-04	4.98
10.000	5.22E-04	4.75

3.2.3 Results

3.2.3.1 Pressure Data

A pressure trace for a reactive experiment for hexane is shown in Figure 3-7. This data is from an experiment for hexane with reactant molar compositions of 1.0 C₇H₁₆ /15.834 O₂ /59.535 N₂, representing a slightly lean gas mixture. For this experiment, both first- and second-stage ignition are observed. It is important to note that this pressure

signal is free of any oscillations or disturbances throughout compression and ignition. Steep pressure rise during second-stage ignition is indicative of a well-mixed air/fuel mixture and nearly homogeneous ignition. Figure 3-8 illustrates the distinctive difference between the pressure trace for a non-reactive and reactive experiment. The latter shows rapid pressure increase due to autoignition during the post-compression period.

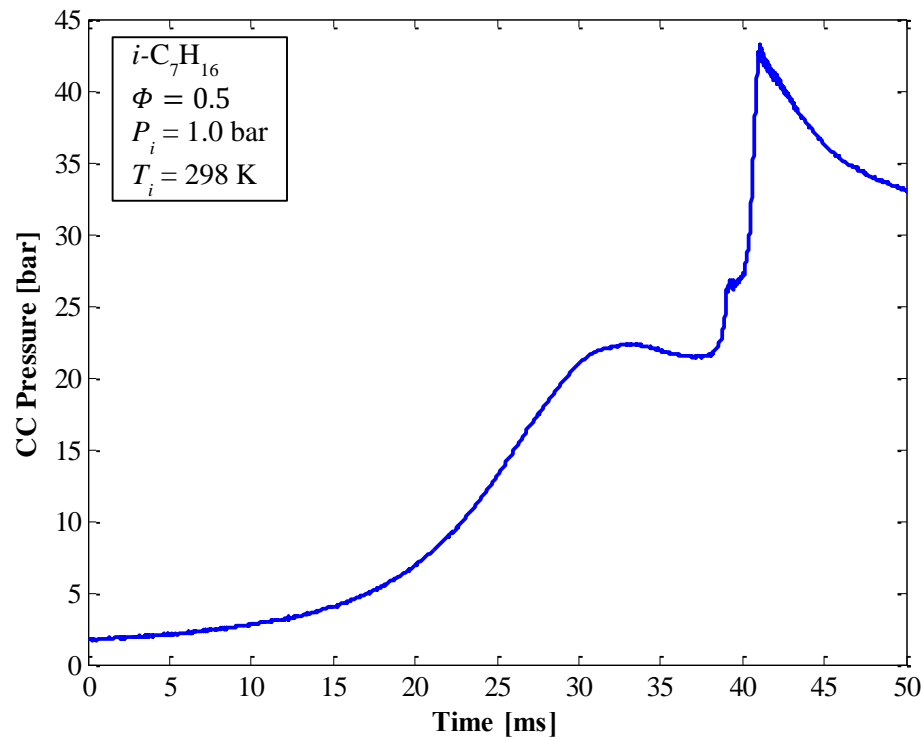


Figure 3-7: Pressure trace for a reactive experiment with Hexane. Three pressure rises are seen here: the first is due to compression, the second is first-stage ignition, and the third is second-stage ignition.

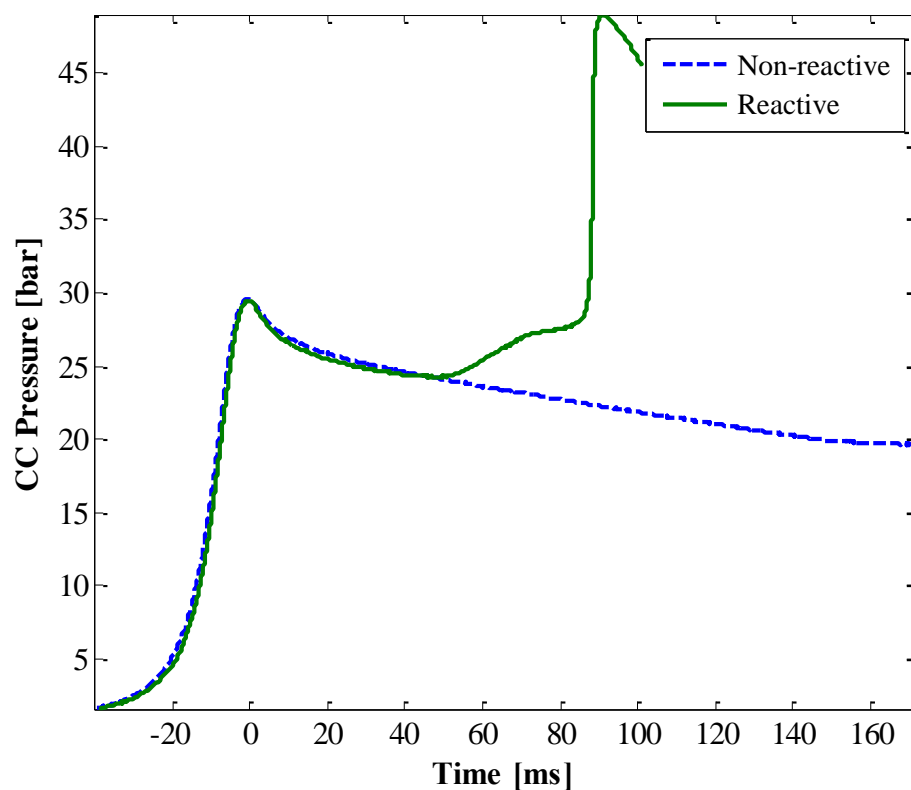


Figure 3-8: Plot illustrating the difference in the pressure trace for a reactive for *iso*-octane and a non-reactive experiment under similar test conditions for air.

3.2.3.2 Repeatability

Repeatability is demonstrated for reactive experiments in Figure 3-9. Five reactive experiments for *iso*-octane were conducted with an equivalence ratio of 0.5, an initial pressure of 1.15 bar, and an initial temperature of 298 K. For each of these cases, the reactant molar concentrations were 1.0 C₈H₁₈ / 25.0 O₂ / 94.0 N₂. Both first- and second-stage ignition for each experiment are shown to match closely among the five

cases. This behavior has been observed for numerous reactive experiments and showcases the ability of the RCCEM to conduct highly repeatable experiments.

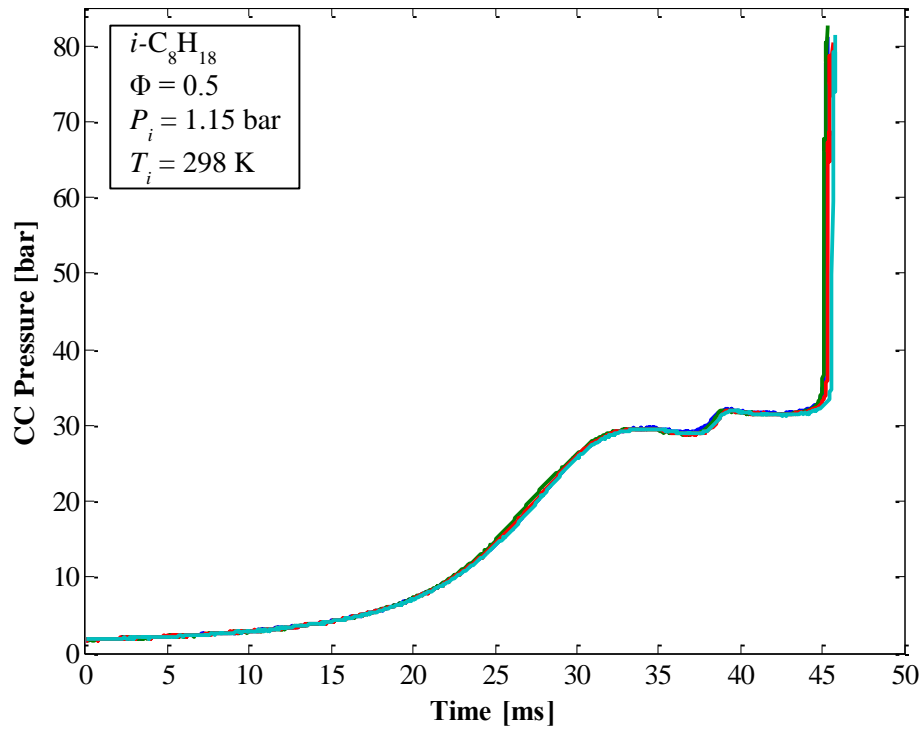


Figure 3-9: Pressure traces for five reactive tests with iso-octane at an equivalence ratio of 0.5. First and second stage ignition are shown to be repeatable.

3.2.3.3 Effect of Equivalence Ratio

Figure 3-10 illustrates the effect of varying the equivalence ratio on the ignition delay time for one compression ratio. As the equivalence ratio is increased from 0.55 to 1.0, the ignition delay increases. This is primarily a result of a decrease in the compressed temperatures due to the existence of more fuel. Further, at equivalence ratios near 1.0, a

linear pressure increase is seen in place of first-stage ignition. This is most likely due to the lower temperatures in the combustion chamber late in the post-compression period.

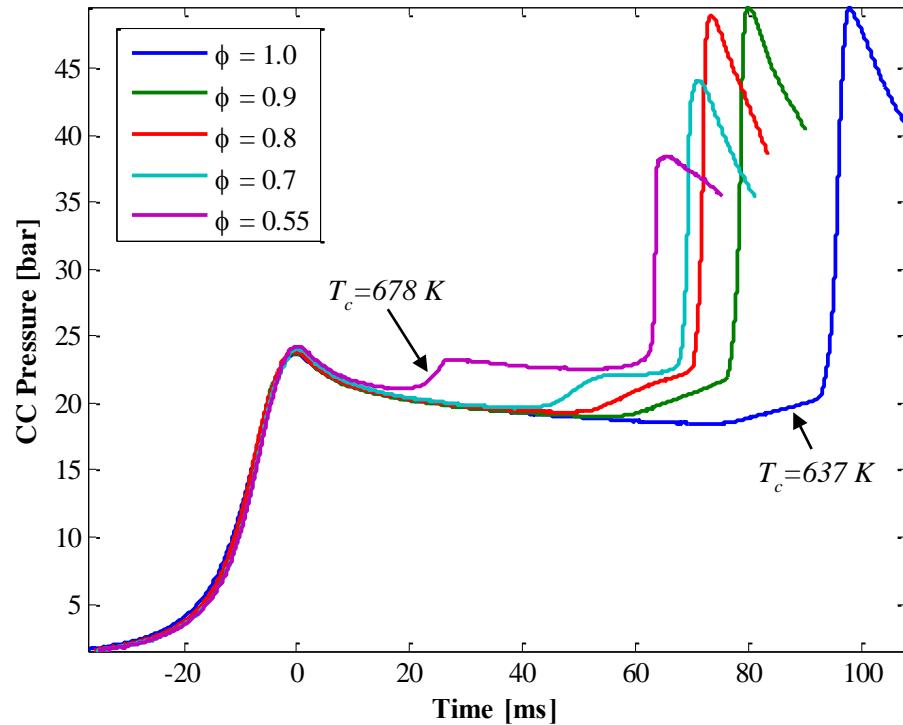


Figure 3-10: The effect of varying equivalence ratio on the pressure for iso-octane. Compressed temperatures vary due to change in gas composition, T_c ranges from 637 K to 678 K. $P_c = 24$ bar.

3.2.3.4 Ignition Delay Times for iso-Octane

Figure 3-11 is a plot of the ignition delay times for *iso*-octane as a function of the compressed temperature for the range of $T_c = 630$ to 700 K. For *iso*-octane, this temperature range is indicative of the low temperature regime where the ignition delay decreases with increasing compressed temperature. The reactant molar concentrations for this set of experiments was 1.0 C_8H_{18} / 17.857 O_2 / 67.143 N_2 and the compressed

temperature was varied by changing the clearance heights from 0.5 to 2.0 inches. The Matlab script for determining the ignition delay times can be found in Appendix C.

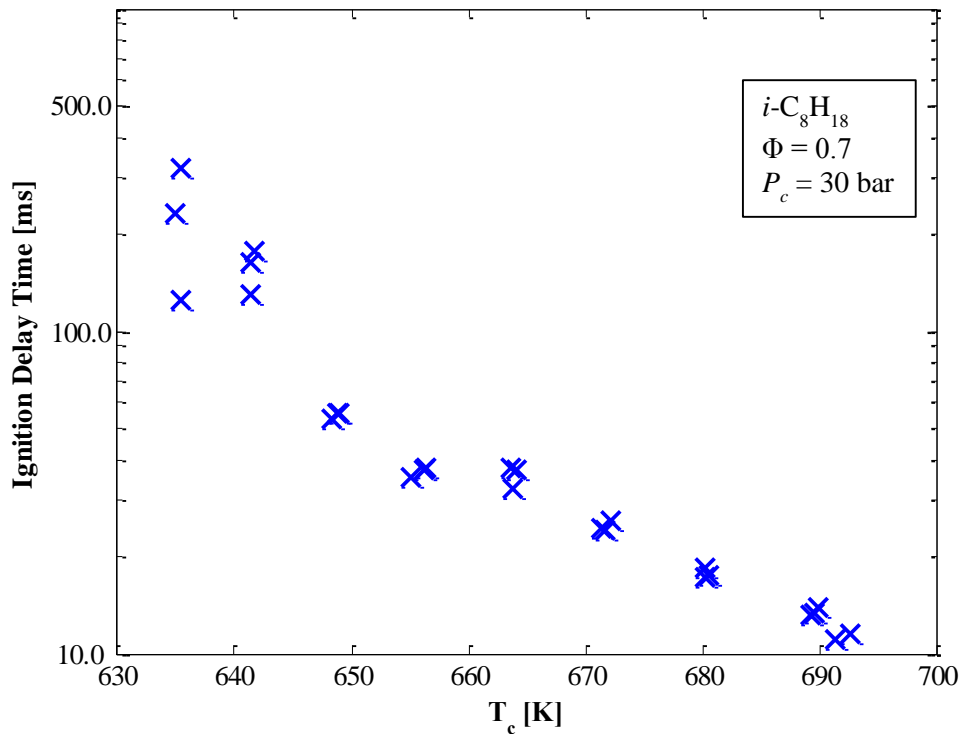


Figure 3-11: Ignition delay times for iso-octane at a compressed pressure, $P_c = 30$ bar, and equivalence ratio, $\Phi = 0.7$, for a compressed temperature range, $T_c = 634 - 694$ K.

3.3 Summary

The results presented in this chapter provide a basis for the performance characterization and operating characteristics of the RCCEM. The RCCEM is capable of obtaining highly repeatable experimental measurements. Non-reactive experiments were conducted to characterize the pressure trace for the RCCEM, and reactive experiments were conducted for hexane and *iso*-octane to illustrate that the RCCEM is capable of chemical ignition studies. Further characterization work is needed to understand the

impact the RCCEM could have on the interpretation of validation data obtained in RCM experiments.

Chapter 4 Numerical Study of Non-Uniform Boundary Temperatures in RCMs

This chapter presents two numerical studies exploring non-uniform boundary temperatures as a potential cause of discrepancies found in literature for data from heated RCM experiments. As described earlier, RCMs are most prominently used to measure ignition delay times which represent the reactivity of a fuel at a given temperature, pressure and concentration. These machines operate by rapidly compressing a reactive gas mixture and maintaining constant volume while measuring the time required for ignition (*i.e.*, ignition delay time). During the compression stroke, heat loss and fluid motion cause heterogeneities to form within the compressed gas temperature field. Heterogeneous temperature fields make it challenging to accurately assign a single reference temperature to characterize an RCM experiment.

The following studies are motivated by the hypothesis that heated RCM experiments result in non-uniform initial gas temperatures and the consequences of this are poorly understood. Previous work by [Allen, Toulson, Edwards, & Lee, 2012] indicates that even with rigorous feedback-controlled heating systems and a well-insulated combustion chamber, boundary temperatures within the RCM are not constant. The data show a difference of approximately 5-7 K between the minimum and maximum boundary temperatures, with the piston crown exhibiting a distinct temperature depression. Because of the exponential relationship between chemical reaction rates and temperature, temperature differences of this magnitude can have significant impact on ignition delay times. For heated RCMs with no feedback control, larger discrepancies are

anticipated, leading to an uncharacterized source of error when interpreting ignition delay data obtained under heated conditions.

4.1 Background

The temperature field that develops during an actual RCM experiment is expected to depend strongly on the initial gas temperature and hence, wall boundary temperatures. The results described in sections 4.2 and 4.3 are important for interpreting ignition delay data in heated RCM experiments, which is common for non-volatile jet fuels, diesel surrogates, and biodiesel surrogates.

The implications of non-uniform temperatures when using a zero-dimensional (zero-D) model to simulate RCM experiments are also poorly understood. Zero-D codes simulate the compression of a homogeneous gas phase mixture which is then held at constant volume until autoignition occurs. Heat loss from the reaction chamber that cools the core gas region is commonly modeled through a volume expansion term. Several studies have been conducted in order to evaluate the validity of zero-D modeling for calculating ignition delay times by comparing to CFD simulation results [Mittal & Chomier, 2014; Mittal et al., 2010; Mittal & Sung, 2006, 2007]. These works have been primarily focused on the validity of the zero-D model for representing the core reacting conditions. However, the influence of non-uniform boundary temperatures is rarely considered.

4.2 The Effect of Non-Uniform Boundary Conditions on Temperature Field Development within Heated Rapid Compression Machine Experiments

4.2.1 CFD Setup/Numerical Specifications

CFD simulations were performed using Ansys Fluent for an RCM with a flat piston, using a 2D configuration. The modeled RCM has a two-inch diameter reaction chamber, and all simulations used a compression ratio of 6, clearance height of 1.417 inches, and stroke length of 7.084 inches, respectively. The combination of clearance height and compression ratio is chosen to represent a likely RCM configuration for testing jet fuels. High initial temperatures (~ 400 K) are needed to vaporize the fuel; thus, a modest compression ratio can generate the low-temperature autoignition conditions of interest (600 – 900 K). Peak compressed temperatures (T_c) for the reported simulations were near 800 K, which resides within the negative temperature coefficient (NTC) region for many gasoline and jet fuel hydrocarbon surrogate components.

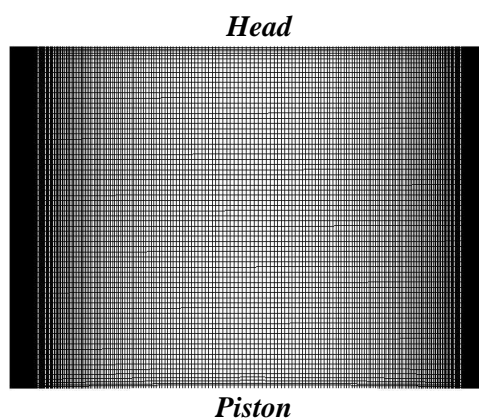


Figure 4-1: CFD mesh at $t = 15$ ms after the start of compression.

An illustration of the 2D CFD grid appears in Figure 4-1, where the geometry of the main combustion chamber is seen. The mesh is shown at a time $t = 15$ ms after commencement of the compression stroke signifying TDC. A quadrilateral mesh of 300 radial by 400 axial divisions is used. A time step of $20.833 \mu\text{s}$ was used with Fluent's In-Cylinder feature corresponding to an engine speed of 2000 RPM with a 0.25 degree step size. In-Cylinder geometry consists of a crank radius of 3.542 inches and connecting rod length of 8 inches. As a result of the geometry and engine speed, the simulations had a total compression time of 15 ms. The simulations use the Pressure-Implicit-Split-Operator (PISO) algorithm along with the Pressure Staggering Option (PRESTO!) for pressure and second order upwind discretization for density, momentum, and energy. All simulations treated air as an ideal-gas; hence, these preliminary simulations only explore the development of the RCM temperature field and not its direct effect on ignition delay times. This worthwhile topic is investigated in section 4.3. The same mesh is used for both the steady-state simulations and the transient RCM compression simulations. Non-uniform boundary temperatures primarily influence the RCM compressed gas

temperature field by introducing heterogeneities in the initial gas temperature prior to initiation of the RCM experiment.

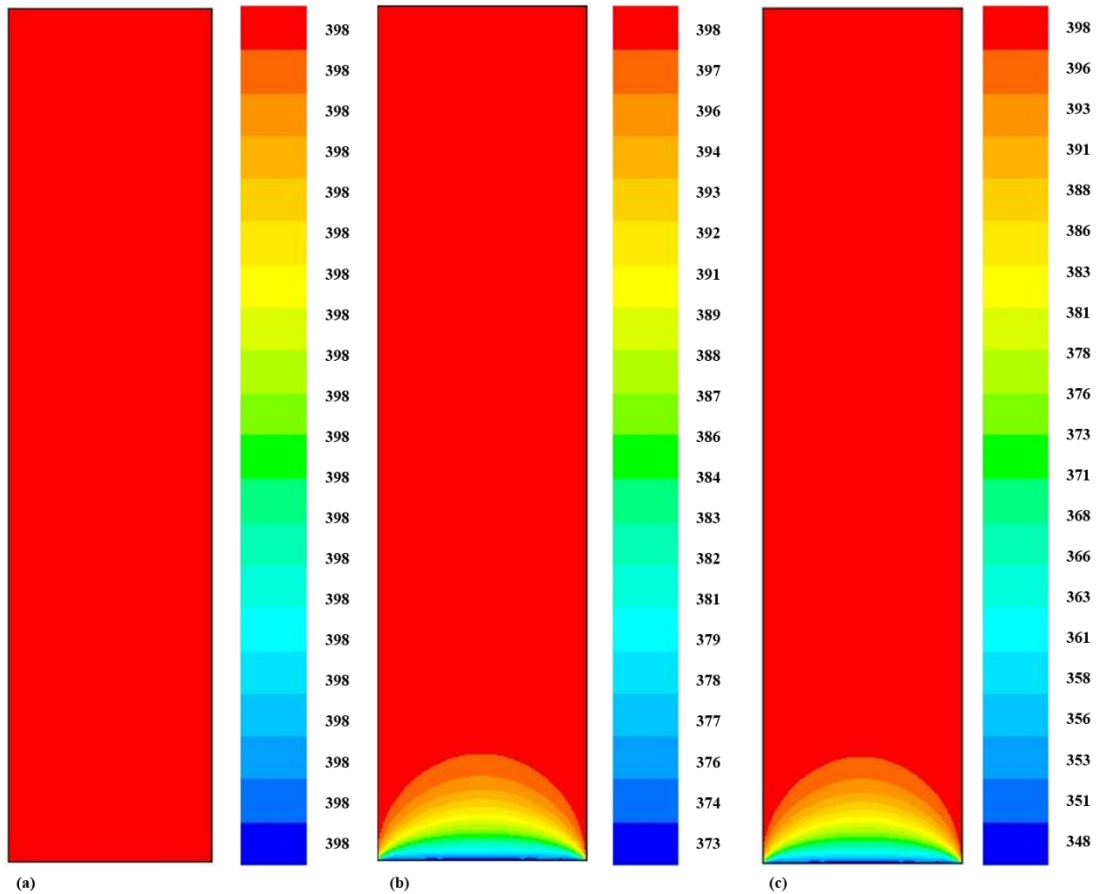


Figure 4-2: Description of initial temperature fields (K) for simulation cases: (a) uniform boundary temperatures, (b) piston 25 K cooler, (c) piston 50 K cooler.

The initial gas temperatures fields used in this work are obtained by performing a steady-state CFD simulation in which the gas temperature is calculated for a given set of boundary temperatures. The steady simulations converged to a 0 K difference between two consecutive iterations. Three unique boundary temperature cases are investigated: (a) uniform boundary temperatures, where all of the walls are set to an initial temperature of

398 K, and two cool-piston cases where the piston is (b) 25 K cooler (373 K) and (c) 50 K cooler (348 K) than the rest of the boundaries. The uniform boundary temperature case serves primarily as a baseline for comparing the influence of the non-uniform boundary temperatures. These test cases are illustrated in Figure 4-2, where the calculated gas temperature field appears for each case. The displayed temperature fields were obtained from the steady-state simulations and used as the initial temperature fields during simulation of the RCM compression stroke.

The temporal development of the gas temperature field in the RCM was calculated by simulating the full RCM compression stroke and 100 ms of the post-compression period. The velocity of the compressing piston is obtained through Fluent's In-Cylinder feature, which calculates piston motion based on engine speed, connecting rod length, and crank radius. This approach is consistent with the approach used by Mittal and Sung [Mittal & Sung, 2006, 2007] in their RCM CFD analyses. The simulations utilized a layering dynamic quadrilateral mesh. The time step, along with a maximum number of iterations per time step of 100, guaranteed convergence based on scaled residuals below 10^{-3} and 10^{-6} , for continuity and momentum and the energy equation, respectively. A time step larger than this did not allow the layering function to operate fully on the dynamic mesh and a negative cell volume error would occur. The flow field within the RCM is treated as laminar based on the published approach of Mittal and Sung, who note laminar flow calculations more strongly supported experimental temperature measurements than turbulent flow models.

CFD simulations were performed for cases (a), (b), and (c) shown in Figure 4-2, while investigating two different initial gas pressures of 1 bar and 2 bar. Steady state

temperature field data previously described was interpolated into the same mesh to initialize using the different temperature cases described for use in the transient in-cylinder calculations. Pressure data was not interpolated along with the temperature data, as it was desired to set the pressure at a specific level prior to compression.

4.2.2 Results

4.2.2.1 Steady State Simulations

This section describes the results of the steady state temperature fields based on differing boundary temperatures. The gas temperature, cylinder walls, and head in all three cases are set at 398 K while the piston temperature is set at 398 K, 373 K, and 348 K for cases (a), (b), and (c), respectively.

Figure 4-2 shows the three initial gas temperature fields at their respective steady state solutions based on boundary temperatures. Cases (b) and (c) show a dome which protrudes into the reaction chamber stemming from the cooler temperature of the piston at a 25 K and 50 K temperature depression, respectively. The distance over which the gradient occurs appears to be constant between (b) and (c), but the gradient is approximately twice as steep in the 50 K cooler piston case. The temperature field steady state conditions are used as the initial conditions for the results obtained in section 4.2.2.2.

4.2.2.2 Transient Simulations

This section describes the results of the RCM compression simulations by displaying the gas temperature fields at top dead center (TDC) ($t = 0$ ms), and the following times after TDC: 5 ms, 10 ms, 20 ms, 40 ms, 60 ms, 80 ms, and 100 ms. For

improved clarity in comparison, the temperature scale in the images is restricted to 100 K (712 – 812 K).

The RCM CFD simulation results using an initial pressure of $p_0 = 1$ bar appear in Figures 4-3 to 4-5. These figures correspond to the uniform boundary temperature case (Figure 4-3), the 25 K cool-piston case (Figure 4-4), and the 50 K cool-piston case (Figure 4-5). The compressed pressure obtained for these simulations was approximately $p_c = 11.23$ bar. The same general behavior is seen for all these test cases, where a cool toroidal vortex is clearly formed at TDC. The vortex continues to contract toward the centerline of the RCM while penetrating axially into the core gas region. Each of the test cases is distinguished by the size and temperatures within the vortices.

Despite the dramatic variation in the initial gas temperature fields which affect the initial mass-averaged temperatures, the peak compressed temperatures were identical for all cases. This is evident in part (a) of Figures 4-3 to 4-7, and it means that the temperature of the end-gas region farthest from the cool-piston crown is unaffected by mixing with the cool vortex in the post-compression period. For the $p_0 = 1$ bar simulations, the vortex penetrates approximately half the clearance distance by the end of the simulation ($t = 100$ ms), leaving a substantial portion of the compressed gas unaffected by the vortex. Zero-dimensional models based on an adiabatic expansion can be expected to accurately predict the temperatures outside of the vortex, where conditions would control the onset of first-stage ignition activity.

Mixing of the cool vortex with the high temperature gas proceeds on the same timescale for all of the simulated cases; however, the temperatures associated with the vortex and surrounding gases are dramatically different. For the uniform temperature case

(Figure 4-3), only a thin thermal boundary layer separates the high-temperature gas from the cool walls. This is evident in Figure 4-3a, where a solid red color appears between the converging vortices. For the cool-piston cases, a significant thermal boundary layer separates the cool wall from the high-temperature gas region at TDC (Figure 4-4a and 4-5a). For the 25 K cool-piston case, the thermal boundary layer extends approximately 0.21 inches from the piston crown, covering a ~ 10 K temperature span. For the 50 K cool-piston case, the gradient is more severe, with a ~ 30 K change in temperature occurring over a distance of approximately 0.26 inches. These results indicate that the temperature difference between the circumferential wall and piston face weakly influence the thermal boundary layer thickness, but strongly influence the temperature gradient across the boundary layer.

The presence of a thick thermal boundary layer can have important consequences when measuring ignition delay times. For example, in the NTC region, the rate of energy release during the first stage of ignition will depend on the extent of the high-temperature gas region. Depletion of this region due to the thermal boundary layer will lead to a slower heat release event relative to predictions made with a zero-dimensional model, thus altering the overall course of the reaction. Furthermore, because the cool vortex region provides the main contribution to hot ignition under some NTC conditions, temperature gradients across the boundary layer can strongly influence the reaction in a manner that is difficult to predict without CFD modeling.

Without reactive simulation work where fuel chemistry is included, it is difficult to assess the impact of temperature non-uniformities on ignition behavior. However, the results in Figures 4-3 to 4-5 imply that the significance of non-uniform boundary

temperatures will depend strongly on the temperature regime being tested. For temperatures below the NTC region, the dominating ignition chemistry will occur in the high-temperature gas region outside of the vortex. Experimental measurements in this temperature region will be minimally influenced by a cool-piston crown. Furthermore, despite the presence of the vortex, homogeneous modeling of the reaction environment that assumes an adiabatically-expanding gas after compression can accurately represent the important temperature that drives the reaction. Within the NTC region, the cool vortex becomes more important, making experimental measurements more sensitive to variation in the piston crown temperature. Although the first stage of ignition will be driven by chemistry occurring outside the vortex where initial temperature non-uniformities have no influence, the main hot ignition chemistry occurs in the vortex where temperatures are strongly sensitive to the initially-cool piston. Overall ignition delay data (*i.e.*, first stage plus second stage) obtained under these conditions are expected to be strongly sensitive to non-uniformities in the initial piston temperature relative to the circumferential wall temperature.

It is noted that these analyses are based on a limited number of CFD tests, and the conclusions may be different for varying clearance height and compression time. For shorter clearance heights, the vortex will destroy a larger fraction of the high-temperature gas region on shorter time scales. Additionally, longer compression times will enhance the role of the vortex at shorter post-compression times.

RCM CFD work in the literature indicates that the mixing of cool boundary layer gases into the gas core by vorticular motion is diminished as compressed pressure increases[Mittal & Sung, 2006]. This reduction is attributed to thinning of the thermal

boundary layer at high pressures because of lower gas thermal diffusivity[Mittal & Sung, 2006]. This suggests that the general conclusions regarding the $p_0 = 1$ bar simulations would be valid for the $p_0 = 2$ bar simulations, but that the consequences of the vortex would be less severe at higher pressures. Therefore, the presence of the vortex would moderate the first-stage heat release rate because fuel oxidation in the cooler vortex may be delayed. A smaller vortex at higher pressures would offset this effect and lead to faster heat release rates during the first stage of ignition. The timing of the main hot ignition depends strongly on the evolution of the temperature and species profiles, and a higher rate of first-stage heat release would accelerate the main ignition.

CFD simulation results for the three initial condition cases appear in Figure 4-5 ($p_0 = 2$ bar, uniform temperature), Figure 4-6 ($p_0 = 2$ bar, 25 K cool-piston case), and Figure 4-7 ($p_0 = 2$ bar, 50 K cool-piston case). The expectations regarding the influence of pressure are confirmed by the results in each of these figures. For all of the simulation results, the vortex is more spatially confined than the corresponding initial condition case simulated at $p_0 = 1$ bar. At the final simulation time of 100 ms, the vortex has penetrated approximately 70% of the vortex penetration distance in the $p_0 = 1$ bar. This is valid for the cases reported in Figure 4-5h, 4-6h, and 4-7h. Furthermore, by comparing parts (e) through (h) for Figures 4-5 to 4-7, it seems that very limited convective penetration occurs beyond 40 ms after TDC. During this period, changes in the gas temperature field appear to occur only by thermal diffusion.

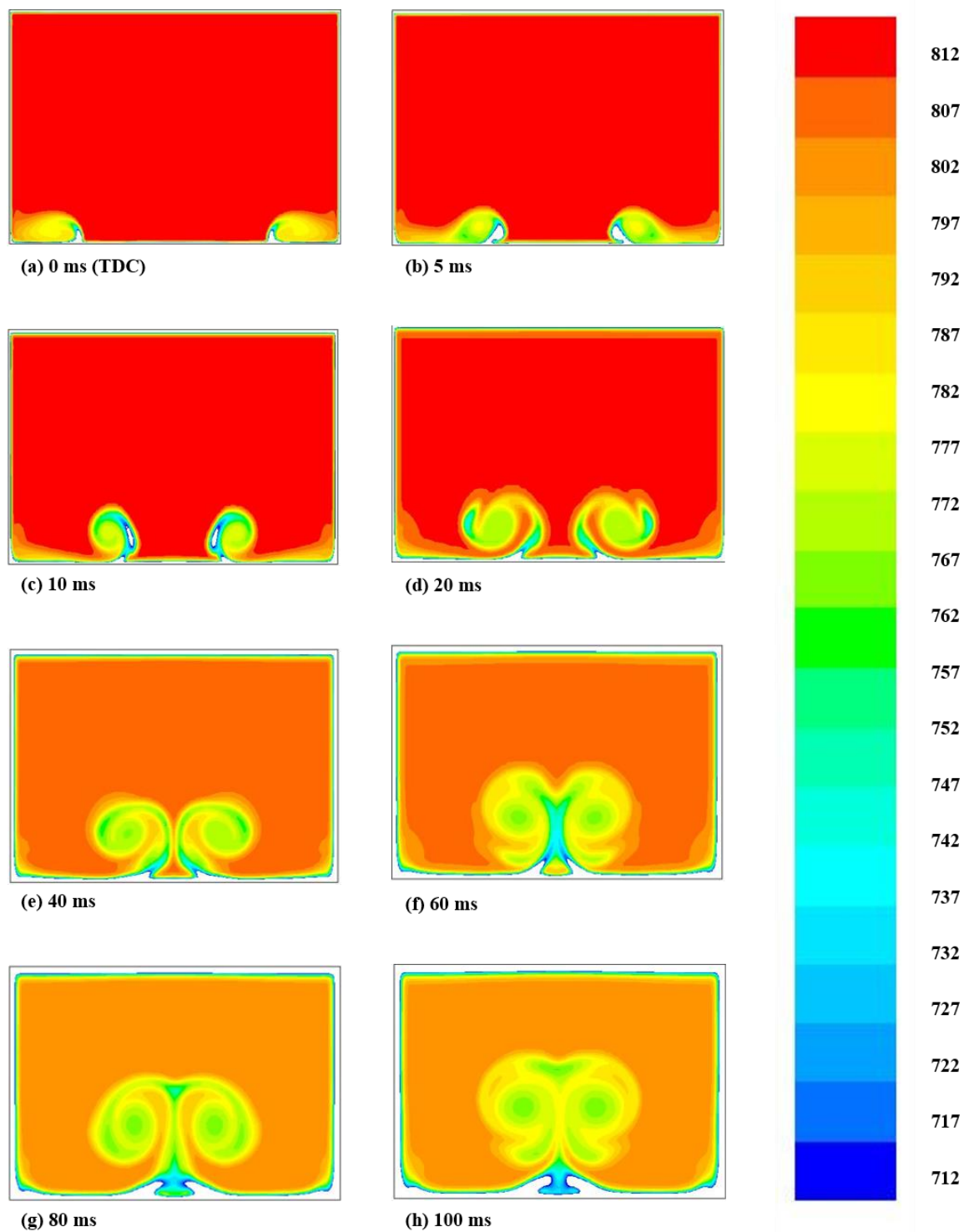


Figure 4-3: Temperature field calculations (K) in post-compression interval for initial condition case (a) with $T_c = 808$ K and $p_c = 11.23$ bar.

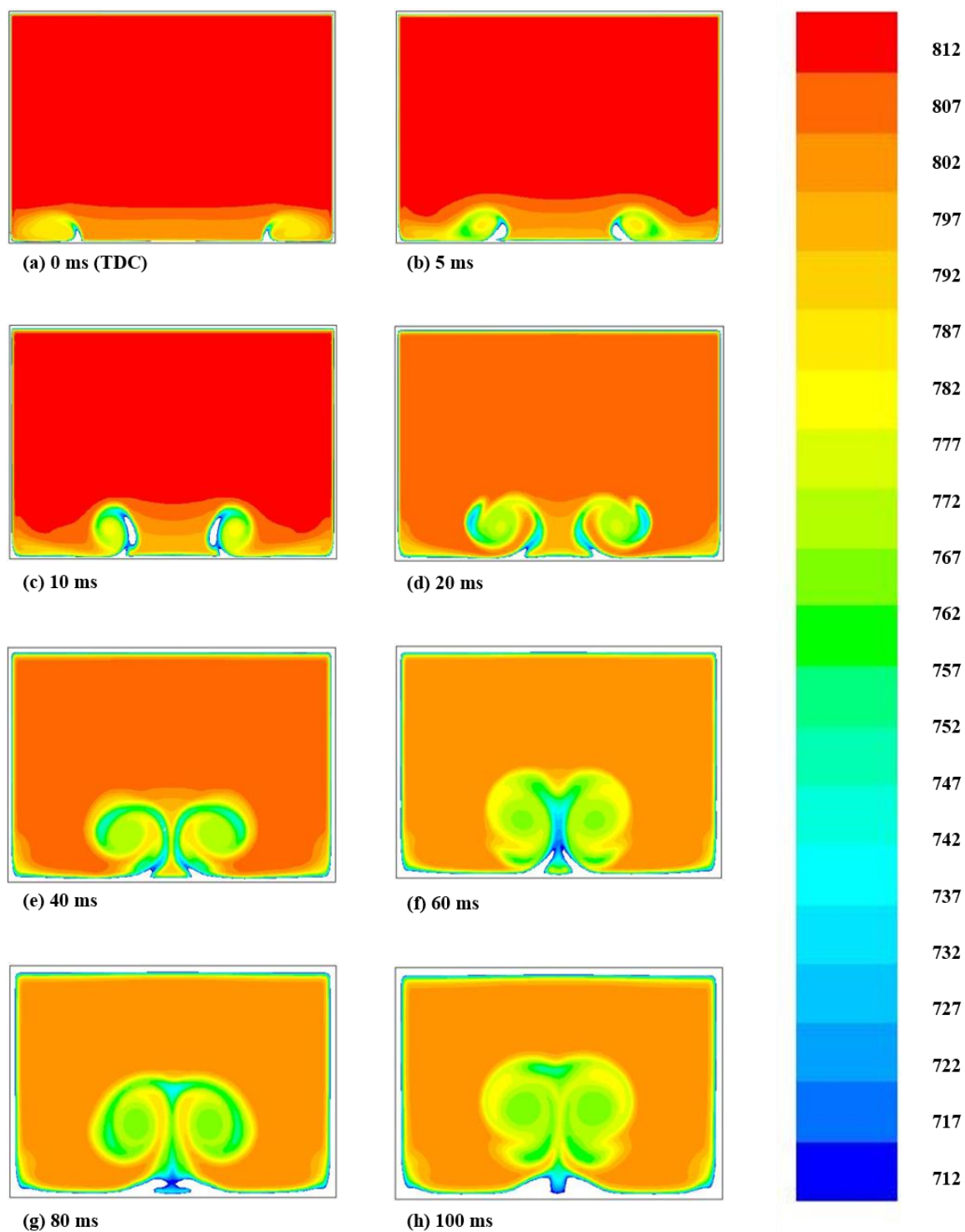


Figure 4-4: Temperature field calculations (K) in post-compression interval for initial condition case (b) with $T_c = 808$ K and $p_c = 11.23$ bar.

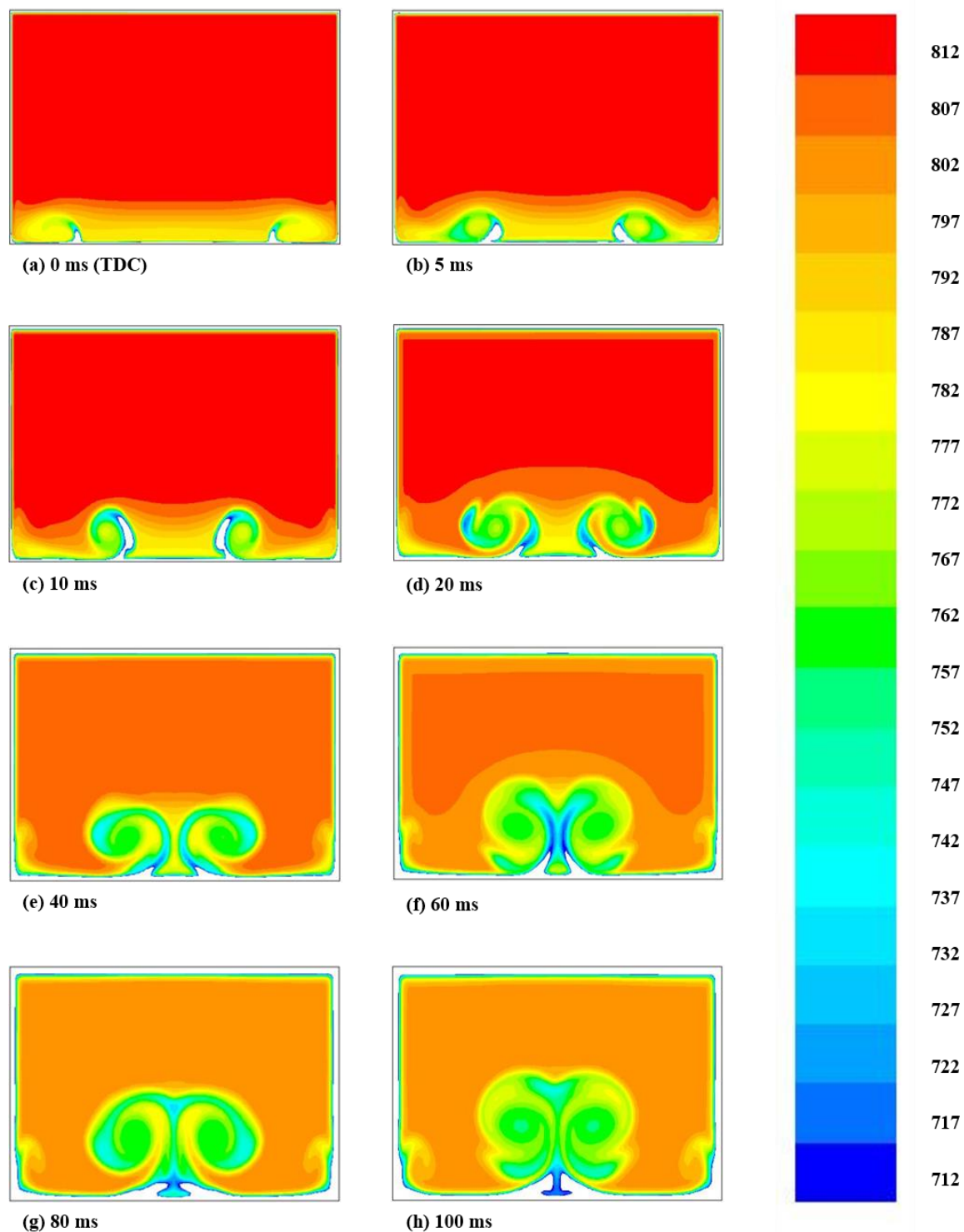


Figure 4-5: Temperature field calculations (K) in post-compression interval for initial condition case (c) with $T_c = 808$ K and $p_c = 11.23$ bar.

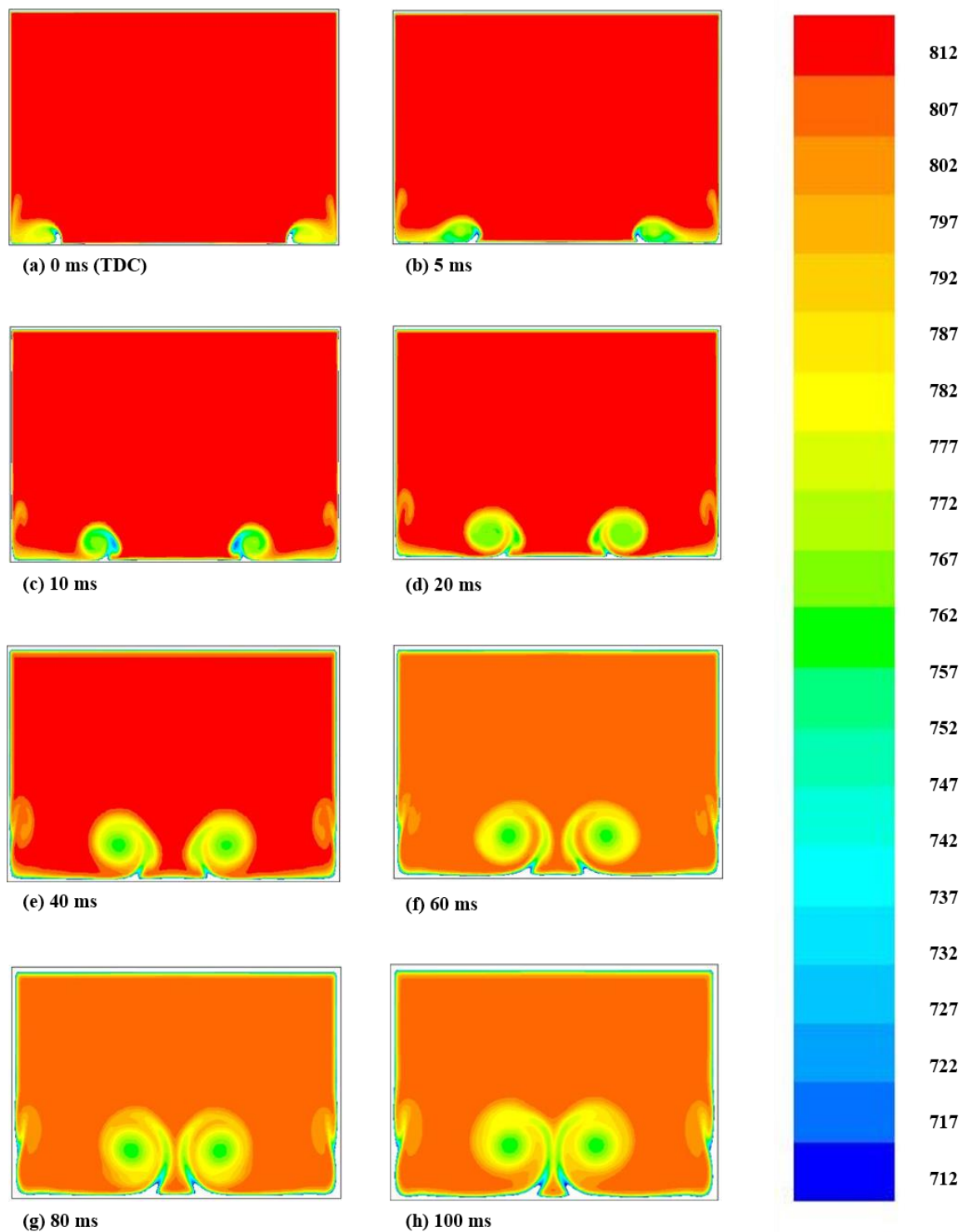


Figure 4-6: Temperature field calculations (K) in post-compression interval for initial condition case (a) with $T_c = 808$ K and $p_c = 23.34$ bar.

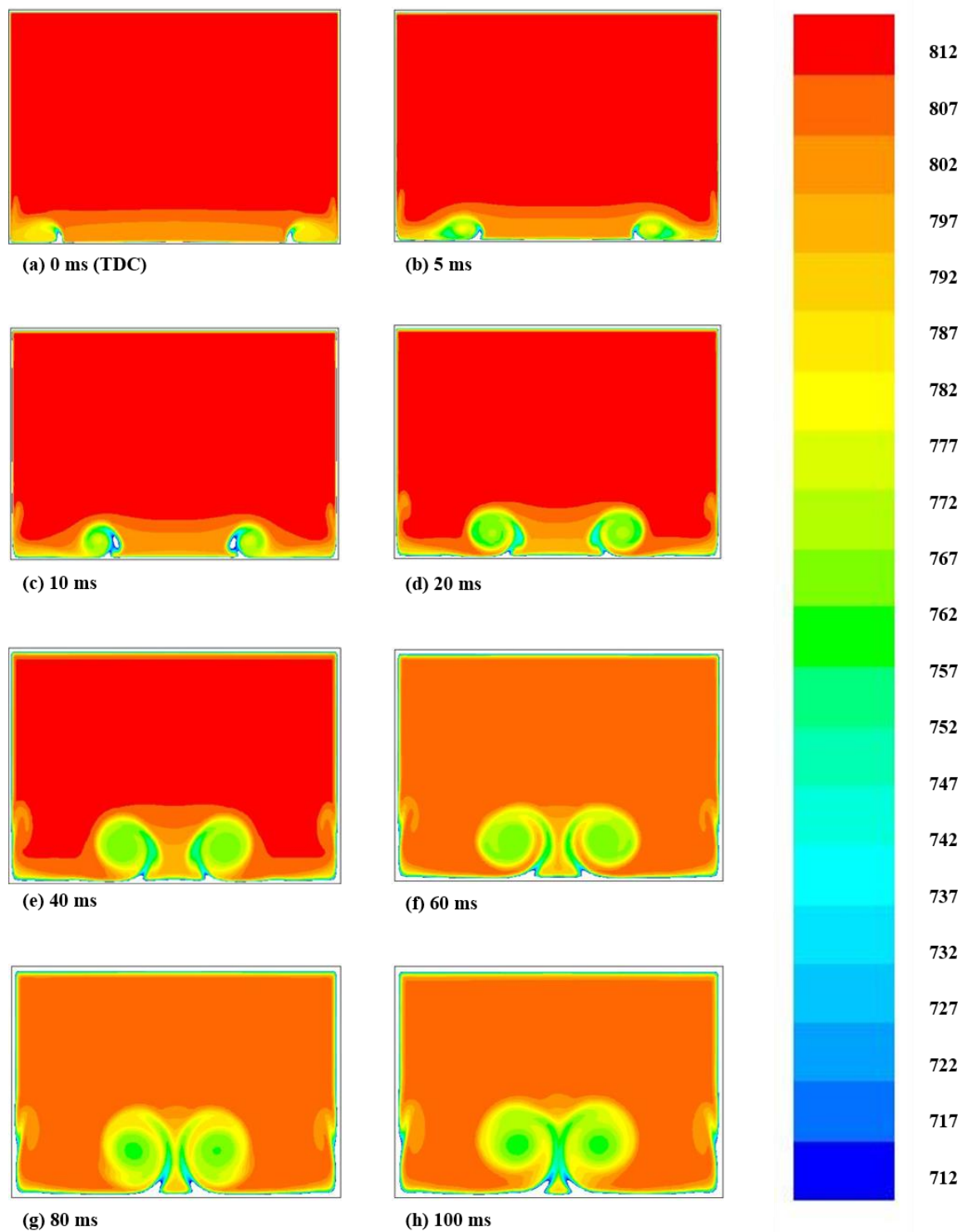


Figure 4-7: Temperature field calculations (K) in post-compression interval for initial condition case (b) with $T_c = 808$ K and $p_c = 23.34$ bar.

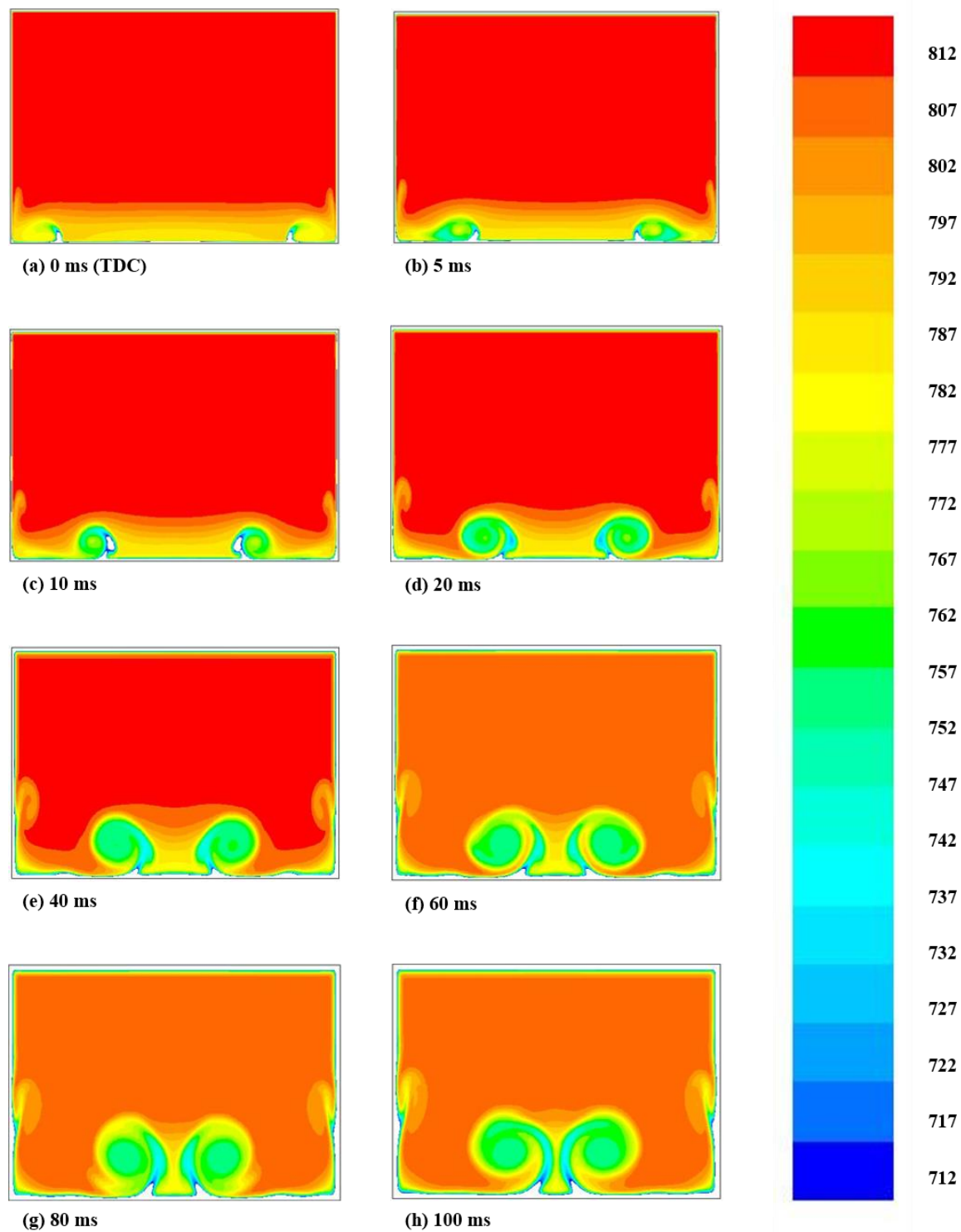


Figure 4-8: Temperature field calculations (K) in post-compression interval for initial condition case (c) with $T_c = 808$ K and $p_c = 23.34$ bar.

4.2.3 Conclusions

This work reports a numerical investigation of the role of non-uniform boundary temperatures in the development of the compressed gas temperature field in an RCM. The results are important for interpreting ignition delay data for non-volatile fuels where heating is applied to an RCM, resulting in non-uniform boundary temperatures. Simulations with three unique temperature fields at initial pressures of 1 bar and 2 bar revealed that non-homogeneous bulk gas temperatures can play an important role in the development of the gas temperature field during and after compression in the RCM.

These simulations indicate that non-uniformities in the initial boundary temperatures lead to a non-uniform initial gas temperature field that is characterized by a cool dome extending from the piston crown. During the RCM compression stroke, the dome is compressed to a spatial region near the piston crown, and a significant temperature gradient can develop across this thermal boundary layer. Temperatures in the cool roll-up vortex are determined by these boundary layer temperatures and have the potential to strongly influence the timing of hot ignition during RCM experiments performed in the NTC region. The impact of a cool piston crown is reduced going to higher compressed pressures due to a change in gas thermal diffusivity that limits the impact of the vortex.

4.3 The Effect of Non-Uniform Boundary Conditions on Ignition Delay Time Measurements from Heated Rapid Compression Machine Experiments

4.3.1 Overview

The results outlined in the previous section demonstrate that non-uniformities in the initial conditions play an important role in the determination of compressed gas

temperature fields. Therefore, the following work was conducted to address some of the shortcomings of that study and specifically address these three open questions: (1) can a creviced piston design suppress temperature heterogeneities that are present prior to compression? (2) how do axially-varying wall temperatures influence development of the gas temperature? and (3) how do the simulated conditions directly impact ignition delay time predictions? This section aims to provide a better understanding of the influence heterogeneities, caused by non-uniform boundary temperatures, have on ignition delay time predictions. A set of reactive CFD simulations for both a flat and creviced piston is presented.

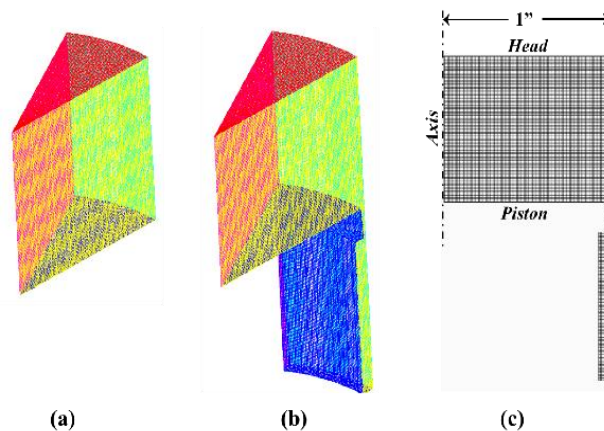


Figure 4-9: Sector geometries for: (a) flat piston, (b) creviced piston, and (c) the computational domain for creviced piston showing the orthogonal grid.

Two main differences between the two studies must be noted. The first is that the compression time used in this study is taken from the RCCEM numerical model rather than using the In-Cylinder feature described in section 4.2.1. Therefore, instead of a compression time of 15 ms, the compression time used was 32 ms. As described above,

lower compression times will suppress some of the effects of the vortex throughout the post-compression period. The second difference is that the software package used in this study is Converge CFD rather than ANSYS Fluent.

4.3.2 CFD Set-Up/Numerical Specifications

Converge CFD is used to perform these simulations in a 3D sector geometry. The modeled RCM has a two-inch bore and a stroke length of eight inches. The sector is comprised of a 30-degree slice of the in-cylinder region as shown in Figure 4-9. Compression ratios of 6, 8, 10, 12, and 14 were explored by varying the clearance height. This range of compression ratios was chosen to represent an RCM configuration typical for testing jet fuels in the low-temperature regime. Peak compressed temperatures (T_c) for the reported simulations ranged from 690 K to 885 K, which covers much of the negative temperature coefficient (NTC) region for the fuel used (PRF 65).

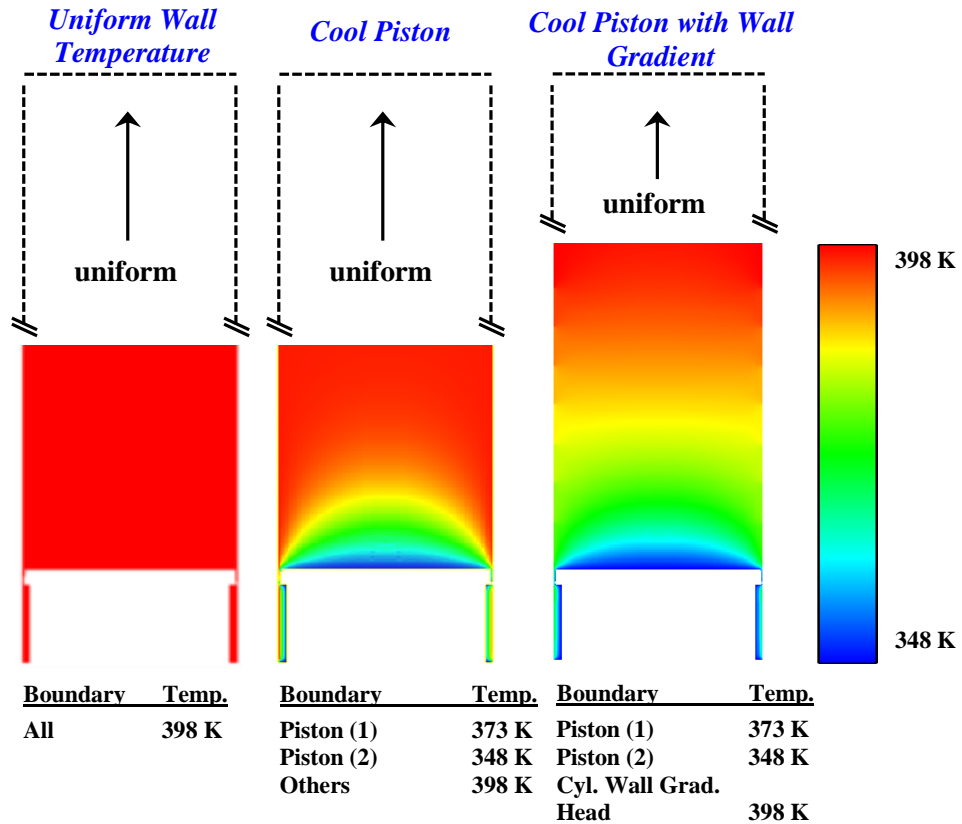


Figure 4-10: Initial temperature fields for the simulation cases: (a) uniform boundary temperatures, (b) “cool” piston temperatures, (c) “cool” piston with wall boundary temperature gradient.

Both the flat and creviced piston reaction chamber configurations are illustrated in Figure 4-9, as well as a planar slice of the creviced geometry. The creviced piston is based off of the optimized design developed by Mittal and Sung, which is also used in the RCCEM [Mittal & Sung, 2006]. These geometries are shown at compression time $t = 32$ ms after the commencement of the compression stroke, which corresponds to top dead center (TDC). Converge CFD uses a modified cut-cell Cartesian method to automatically generate an orthogonal grid within the geometry at each time step based on a base grid size. The base grid sizing for these simulations was $dx = dy = dz = 0.035$ inches. Further

grid refinement was achieved by applying a permanent fixed embedding with a scale of two over the entire geometry. Converge CFD has a built-in variable time step algorithm governed by the convective-, sound speed-, and the diffusive-Courant-Friedrichs-Lewy (CFL) numbers, which are evaluated at each time step and adjusted based on optimizing model run-time performance. The simulations use the skeletal kinetic model for Primary Reference Fuel (PRF) from Tsurushima [Tsurushima, 2009] containing 33 species and 38 reactions. All of the simulations tested primary reference fuel with an octane number of 65 (PRF65), using the ideal gas equation of state with species mass fractions for *n*-heptane/ *iso*-octane / O₂ / N₂ = 0.02156 / 0.04077 / 0.21849 / 0.71918 at a compressed pressure $P_c = 7$ bar. Momentum, energy, and species equations were solved. Combustion modeling was carried out by the SAGE detailed chemistry solver, coupled with a two-dimensional multi-zone model which solves the chemistry in temperature bins of 2 K and equivalence ratio bins of 0.05. Pressure and velocity were solved through the use of the Pressure-Implicit-Split-Operator (PISO) algorithm. Identical simulation and modeling parameters were used for both the steady state and transient simulations.

These simulations, similar to those described in section 4.2, explored the influence of initial temperature field heterogeneities by using steady state temperature fields as the initial temperature fields for transient simulations with five unique boundary temperature cases. The initial temperature fields were determined by setting the boundary conditions to their respective temperatures and stepping through the simulation time at constant volume (the piston at bottom dead center (BDC)) until the average temperature in the cylinder reached a steady state value at which the temperature variation was 0 K over consecutive time steps. Figure 4-10 illustrates the different initial temperature fields

for each of the following cases: (a) the uniform boundary temperature case, (b) the two “cool” piston cases (25 and 50 K), and (c) the two “cool” piston with wall gradient cases. The uniform case provides a baseline for comparison to the non-uniform boundary temperature cases. The “cool” piston with wall gradient simulations simulated a spatial variation in the cylinder wall temperature starting at the piston and increasing in temperature towards the head. This would be characteristic of the gap between band heaters on experimental setups. Only the energy equation was solved for the steady simulations. Temperature fields covering the entire sector geometry were obtained for each case and were initialized as the temperature fields in the RCM prior to the compression stroke. These steady simulations were considered to be pressure independent because the initial pressure can be varied in experiments.

The temporal development of the gas temperature field in the RCM was determined by simulating the full RCCEM compression stroke with no expansion until ignition occurred. The simulations each had a compression time of 32 ms. The velocity profile was set by the time and position of the cam follower taken from the numerical model described in section 2.1.4. All of the simulations were run under laminar conditions coinciding with the work in section 4.2 and work conducted by others [Mittal & Chomier, 2014; Mittal & Sung, 2006].

4.3.3 Results

The simulated ignition delay times for the flat piston cases appear in Figure 4-11. It can be seen that the disparity between the boundary temperature cases depends strongly on the particular condition being investigated. At the lowest compressed temperature (~680 K), a difference of 18 ms separates the shortest and longest total ignition delay

times. The 50 K/wall gradient case is an outlier at this condition, with all other cases predicting a roughly identical ignition delay time. At the transition into the NTC region (~ 750 K), only 3 ms separates the shortest and longest total ignition delay times. Moving farther into the NTC region ($T_c \sim 850$ K), only the cool piston cases with wall gradients ignited. All of the other simulations at this condition failed to ignite. For the two cases in which ignition occurred, the total ignition delay times were separated by 66 ms. Two more compression ratios were simulated for which no ignition delay times could be determined. The first was targeted at a compressed temperature near $T_c = 815$ K, but heat release during the compression stroke prohibited the accurate assignment of a reference temperature. The second case, which was for the highest compression ratio investigated, did not ignite during the allotted simulation time (200 ms).

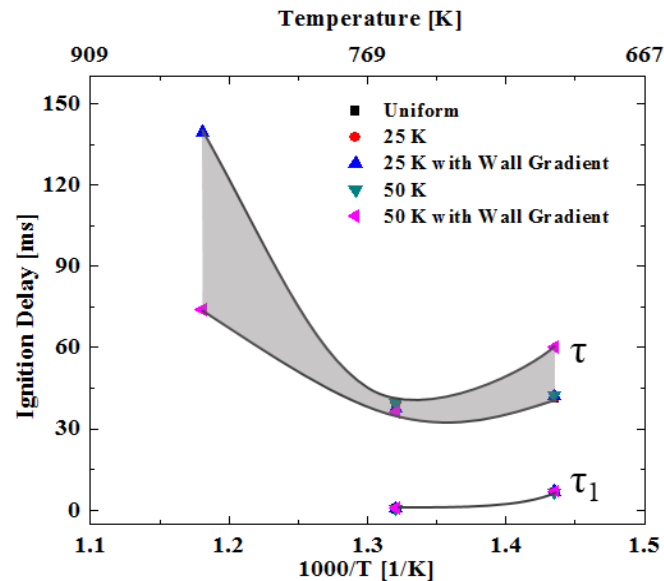


Figure 4-11: Ignition delay times determined for each initial temperature field with $P_c = 7$ bar for the flat piston.

The wide variation in responses motivates a review of the temperature and species mass fraction fields that develop during the chemical induction period. Simulations results for the case of $T_c = 750$ K are used here as an example, for which the temperature and mass fraction fields for n-C₇H₁₆, CH₂O, H₂O₂, and OH are reported at times of $t = 0$ and $t = 10$ ms after TDC (ATDC). These results appear in Figure 4-12 for the uniform and 50 K/wall gradient cases for which the total ignition delay times are 40 ms and 36 ms, respectively. The temperature fields at TDC clearly depict the presence of a cool vortex penetrating the core gas region, which is consistent with prior RCM CFD studies. The effect of the non-uniform boundary temperature is plainly visible in the temperature fields at TDC in Figure 4-12. The non-uniformities have led to a gas temperature reduction both within and around the vortex. Despite this difference, the peak gas temperature outside of the vortex is the same at TDC for both of the boundary cases. At this point in time, the consumption rate of n-C₇H₁₆ is very modest, but it is evident that the thermal stratification for the 50K/wall gradient cases leads to a spatially-unique heat release pattern. Combined with the convective mixing induced by the flat piston, a complicated process unfolds where the overall reaction rate is modulated by the mixing of regions with enhanced and moderated reactivity (*i.e.*, based on local temperature and species concentrations). The ignition delay predictions, combined with the temperature and mass fraction fields, clearly show that heated flat piston RCM experiments are susceptible to non-uniform boundary temperatures.

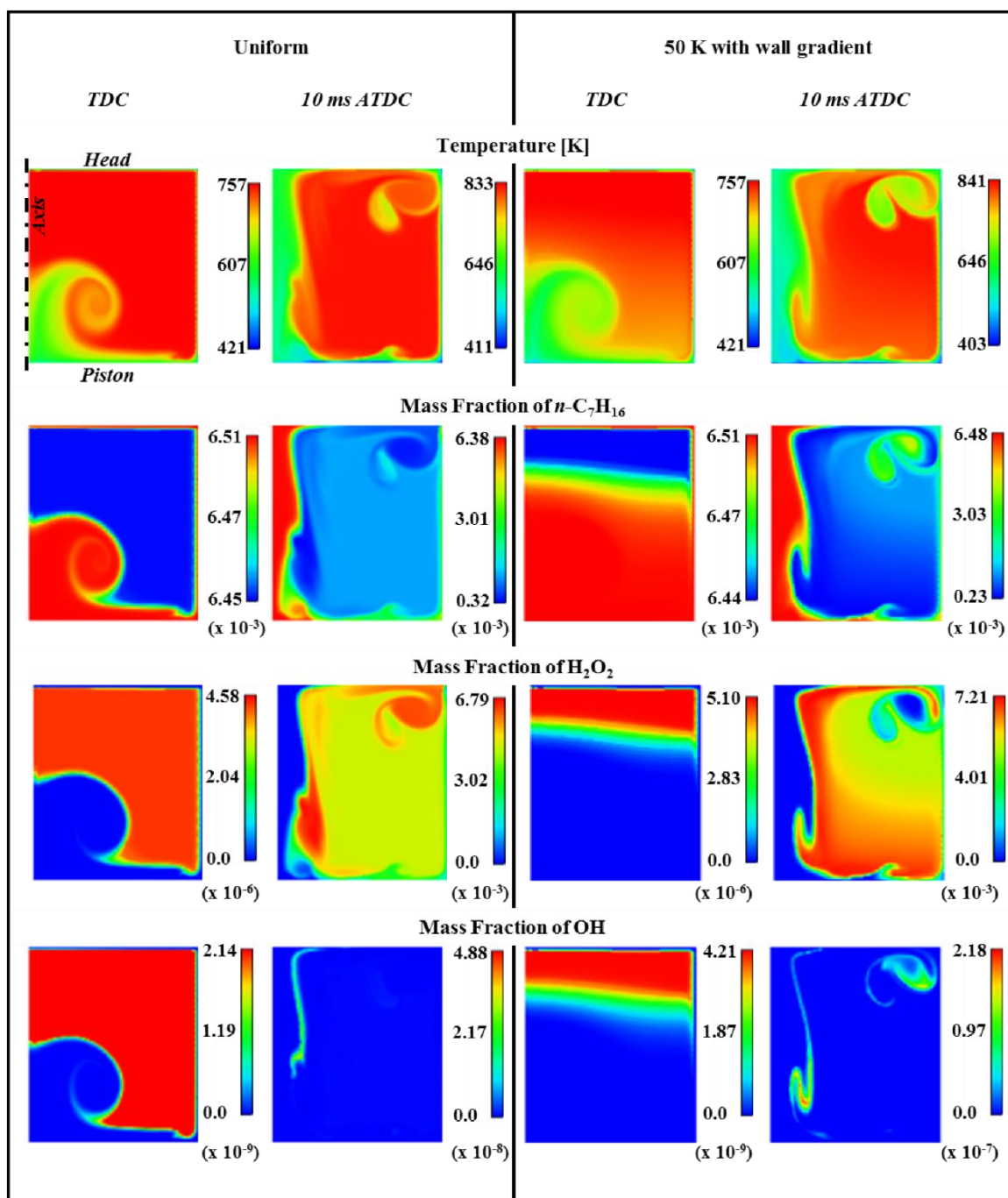


Figure 4-12: Compressed temperature field and selected species mass fractions at $t=0$ (TDC) and 40 ms ATDC for uniform and 50 K/wall gradient boundary temperature case with $T_c = 753$ K with the flat piston.

The simulated ignition delay times for the creviced piston cases appear in Figure 4-13. It is especially important to view these results relative to the flat piston simulations to determine whether the creviced piston can effectively suppress the influence of the non-uniform boundary conditions. A review of the total ignition delay predictions in Figure 4-13 suggests that the creviced piston is largely effective for this purpose. The variation among the total ignition delay times changes across the set of compressed temperatures, with maximum discrepancy (9 ms) between boundary cases occurring at the highest compressed temperature (870 K). As with the flat piston simulations, an additional compression ratio was tested that led to heat release during the compression stroke. These data points have been omitted from the analysis.

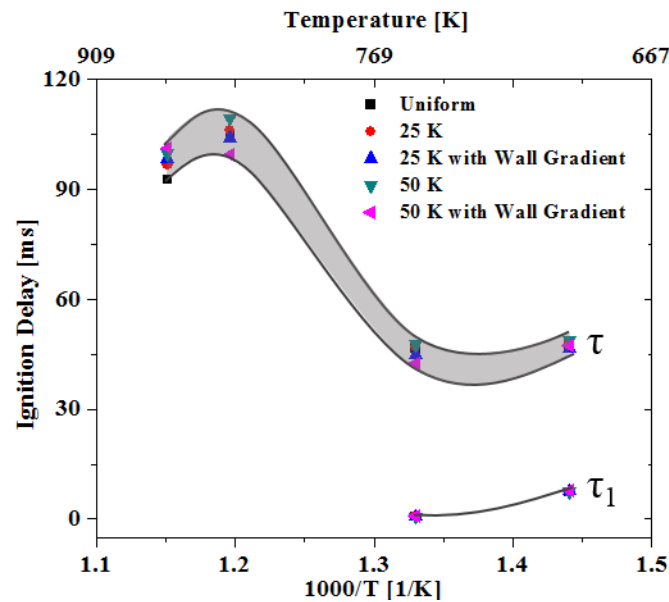


Figure 4-13: Ignition delay times determined for each initial temperature field with $P_c = 7\text{bar}$ for the crevice piston geometry.

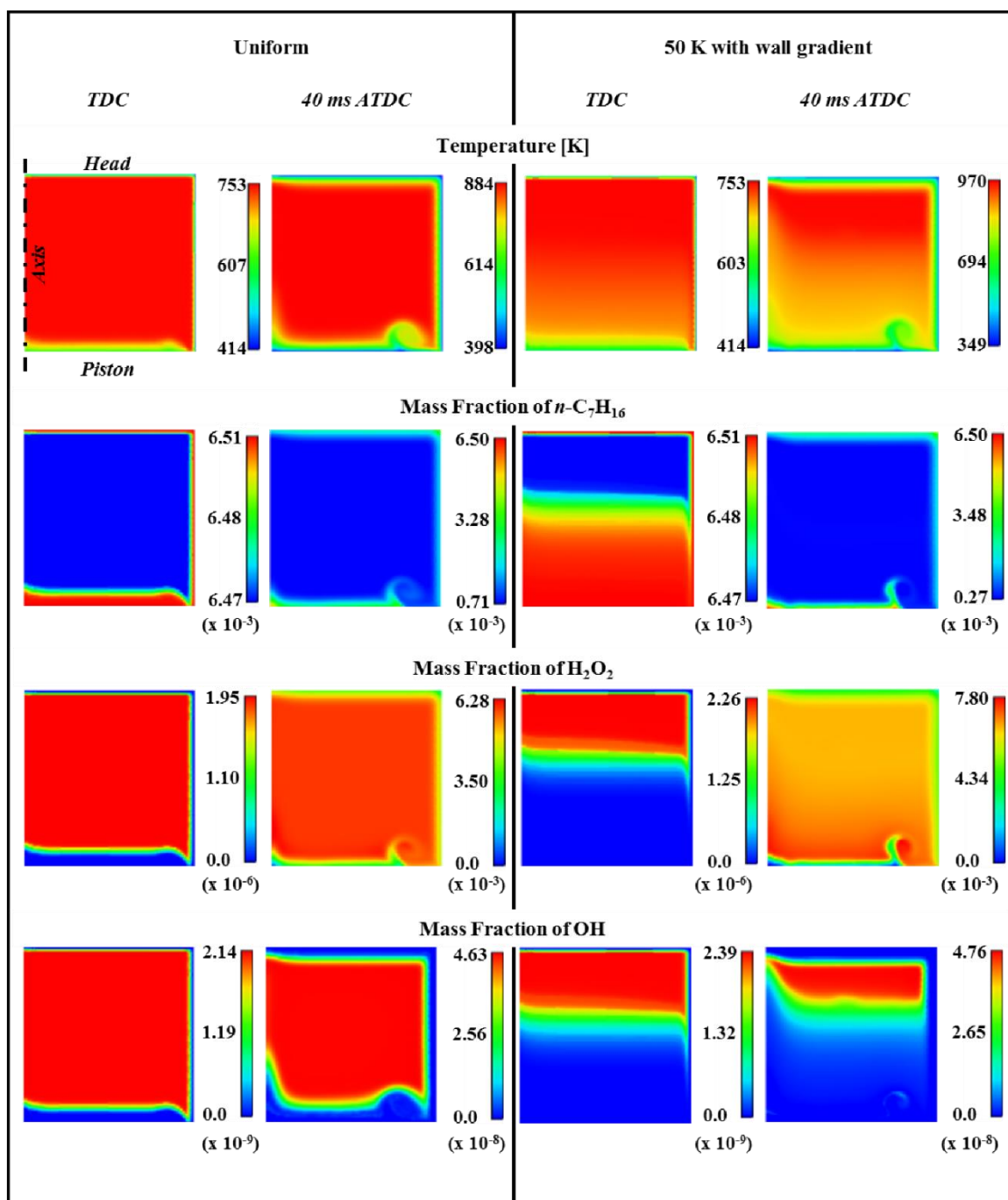


Figure 4-14: Compressed temperature field and selected species mass fractions at $t=0$ (TDC) and 40 ms ATDC for the uniform and 50 K/wall gradient boundary temperature cases with $T_c = 753$ K with the creviced piston.

The ignition delay time predictions suggest that variations in the piston and wall temperatures do not significantly influence the experiments if a creviced piston is used. Further investigation into the underlying phenomena is done by comparing the temperature and mass fraction fields for the case near $T_c \sim 750$ K. The uniform and 50 K/wall gradient cases are compared in Figure 4-14, where temperature and mass fraction fields (n -C₇H₁₆, CH₂O, H₂O₂, OH) are displayed at TDC and 40 ms ATDC. The general ability of the creviced piston to suppress the influence of the roll-up vortex is obvious when comparing Figures 4-12 and 4-14. In spite of this characteristic, it can clearly be seen that temperature stratification does exist in core gas at TDC for the 50K/wall gradient case. As with the flat piston simulations, this leads to a spatially-unique heat release pattern as the fuel (*e.g.*, n -C₇H₁₆) is broken down more rapidly in the hotter region. This is evident in the n -C₇H₁₆ mass fraction fields at TDC, but the scale of the colorbar should be considered when interpreting the data. At 40 ms ATDC, two significant things have occurred in the 50 K/wall gradient case: (1) the enhanced reactivity in the hotter region has exacerbated the thermal stratification relative to TDC, and (2) the peak temperature in the hot region (970 K) is greater than the peak temperature in the uniform case (884 K). The latter occurs because the fuel mass in the simulation was calculated in Converge using the ideal gas equation of state with a specified fuel mass fraction, pressure, average temperature.

The results shown in Figures 4-12 and 4-14 support the following interpretation of the non-uniform boundary cases: (1) The non-uniform initial temperature field results in a stratified compressed gas temperature field at TDC; (2) The temperature stratification at TDC forms a hot zone of enhanced reactivity and a cool zone of mild reactivity which are

connected by a stratified region; (3) The reaction proceeds independently within these regions, and the most reactive region determines the observed ignition delay time. For the case depicted in Figure 4-14, the reaction trajectory to hot ignition is controlled by the peak temperature reached in the hot region after first-stage ignition. This implies that if the same fuel mass reacts in this region, regardless of the boundary case tested, the total ignition delay time will be minimally affected by the non-uniform temperature field. However, these non-uniformities would be significant if the hot region temperature is in the NTC region, meaning the cool region may be more reactive. Under these conditions, a compressed temperature calculated using the adiabatic core hypothesis would be reflective of the hot region temperature, but the controlling chemistry would be characteristic of the cool region.

The ignition delay times were calculated as the difference from the time at TDC until the maximum value of pressure change with respect to time (dp/dt). For these simulations, the script present in Appendix B was used. This script takes the pressure data for a group of simulations and calculates the ignition delay time for each simulation and populates a new text file with the simulation name, compressed temperature and pressure, and first- and second-stage ignition delay times.

4.3.4 Conclusions

CFD simulations have been used to investigate the influence of non-uniform RCM boundary temperatures on compressed temperature fields and ignition delay times. These results are important for interpreting heated RCM data for non-volatile fuels and for understanding the level of rigor required to properly characterize these experiments.

The simulation results indicate that ignition delay data from flat piston RCMs are susceptible to non-uniform gas temperatures present at the start of an experiment. The compression stroke initiates a complicated process that involves charge cooling and convective mixing of gas regions with different temperatures and species concentrations. It was found that a creviced piston can suppress some of these effects by virtually eliminating convective mixing of the gas regions in the RCM. The lack of convective mixing in the presence of thermal heterogeneities allows two regions to form, each with unique temperatures and reactivities. Chemical reaction can proceed independently in these regions, and provided that the hot region controls the global response, the ignition delay time should closely match an experiment where the boundary temperatures are uniform. However, in the NTC region, the global response will be susceptible to the temperature non-uniformities because the cooler gases surrounding the piston will exert the controlling chemistry.

4.4 Summary

The influence of non-uniform boundary temperatures on heated RCM experiments have been explored as a potential cause for discrepancies in ignition delay times found in the literature. CFD simulations were used with heterogeneities present in the initial gas temperature field to predict the temporal development of compressed-gas temperature fields and ignition delay times. Non-uniform boundary temperatures influence the initial temperature field by introducing heterogeneities prior to compression. For cool-piston cases, steady state simulations revealed the presence of a dome-shaped temperature gradient over the crown of the piston. For cool-piston with wall gradient cases, the temperature gradient was much larger and penetrated further into

the initial volume of the combustion chamber. It is shown that the temperature field development can be strongly influenced by non-uniform boundary temperatures. Non-reactive simulations with the flat piston revealed that a temperature gradient develops across the roll-up vortex that is directly related to initial temperature fields. The effect of this on ignition delay times was then studied for both flat and creviced pistons. Ignition delay time predictions for each of the unique boundary temperature cases illustrated the potential susceptibility of flat piston experiments to non-uniform boundary temperatures. The creviced piston was determined to mildly suppress these effects; however, additional points in the NTC region should be explored to fully understand the reaction trajectory predicted. Compressed-gas temperature fields and select species concentrations for both the flat and creviced piston simulations showed that non-uniform boundary temperatures led to thermal and unique species stratification. On a global level, the ignition delay time predictions were not shown to be sensitive to this.

Chapter 5 Summary & Future Work

5.1 Summary

The main goal of this thesis was to increase the understanding of potential causes for discrepancies in published validation data obtained from RCMs. The work described throughout this thesis addresses this in two ways: (1) development of a new type of experimental apparatus to increase understanding of the role of heat loss during post-compression, and (2) investigating the role of non-uniform boundary temperatures in heated RCM experiments. Conclusions of the latter are presented at the end of Chapter 4.

In regard to the first, a summary of the Rapid Compression Controlled-Expansion Machine in its current state will be discussed. The RCCEM is an extremely high quality test fixture capable of testing the reactivity of premixed gaseous mixtures throughout the low-temperature regime and over a wide range of experimental conditions. In its current state, the RCCEM is capable of repeatable conditions of compressed temperatures up to 700 K, compressed pressures up to 55 bar, and compression times on the order of 30-50 ms. Over 350 experiments have been conducted with the RCCEM, allowing for preliminary characterization work to be completed as described in Chapter 3. It is important to note that the characterization of the RCCEM must be continued to really understand the effects of experimentally varying heat loss rates on RCM experiments.

The RCCEM was ultimately designed to offer a new experimental method for potentially characterizing the effects of heat loss in RCM experiments. Currently, the machine is not able to test with all of the functionality it was originally designed for.

However, the RCCEM provides a solid foundation for future work. Some specific items are discussed in the following section for future work.

5.2 Future Work

For the RCCEM, the following items should be considered for future development. First of all, a clever solution to prevent the cam follower from jumping off of the cam surface during operation should be explored. A solution to this problem can improve overall compression times, as well as ensure that the combustion piston does not come into contact with the gas sampling valve.

Second, incorporating heat loss into the numerical model for the RCCEM can be used to develop cam profiles and more accurately predict the experimental conditions that the RCCEM is capable of reaching. Using the first cam designed for use in this work as a baseline, the model can be correlated to mimic actual RCCEM performance.

Third, more cam profiles should be acquired to explore a wider range of operating conditions. It is of particular interest to acquire a traditional RCM cam to separate out the heat loss rates seen when constant volume is held throughout post-compression. This will allow for generalized heat loss in the RCCEM to be measured and compared to cams with specific expansion heights.

Additionally, the RCCEM was designed to incorporate a feedback-controlled heating system. This heating system will allow the RCCEM to test non-volatile fuels by heating the combustion chamber prior to a test. The heating system will also allow the RCCEM to test at higher compressed temperatures than in its current state.

Lastly, set up the gas sampling valve to quench chemical reactions during RCCEM experiments and analyze species concentrations using the Gas-

Chromatograph/Mass-Spectrometer located in the lab. This can provide essential validation data to kineticists and combustion modelers.

The ability to incorporate some or all of these changes will continue to develop the RCCEM into a truly world-class experimental setup. Further experimental work should also be used to continue the performance characterization of the RCCEM.

BIBLIOGRAPHY

- [Affleck, W. S., & Thomas, A. , 2006]. An Opposed Piston Rapid Compression Machine for Pre-flame Reaction Studies. *ARCHIVE: Proceedings of the Institution of Mechanical Engineers 1847-1982 (vols 1-196)*, 183, 365–387.
- [Allen, C. , 2012]. *Advanced Rapid Compression Machine Test Methods and Surrogate Fuel Modeling for Bio-Derived and Diesel Fuel Autoignition*. Michigan State University.
- [Allen, C., Toulson, E., Edwards, T., & Lee, T. , 2012]. Application of a Novel Charge Preparation Approach to Testing the Autoignition Characteristics of JP-8 and Camelina Hydroprocessed Renewable Jet Fuel in a Rapid Compression Machine. *Combustion and Flame*, 159(9), 2780–2788.
- [Chaos, M., & Dryer, F. L. , 2010]. Chemical-Kinetic Modeling of Ignition Delay: Considerations in Interpreting Shock Tube Data. *International Journal of Chemical Kinetics*, 42, 143–150.
- [Cho, G., Jeong, D., Moon, G., & Bae, C. , 2010]. Controlled Auto-Ignition Characteristics of Methane–Air Mixture in a Rapid Intake Compression and Expansion Machine. *Energy*, 35(10), 4184–4191.
- [Dohring, K. , 1986]. *The Relative Effects of Intake and Compression Generated Turbulence on I.C. Engine Combustion Duration*. The University of British Columbia.
- [Ferguson, C. R., & Kirkpatrick, A. T. , 2001]. *Internal Combustion Engines: Applied Thermosciences*. (J. Hayton, Ed.) (2nd ed.). New York, NY: John Wiley and Sons, Inc.
- [Goldsborough, S. S., Banyon, C., & Mittal, G. , 2012]. A Computationally Efficient, Physics-Based Model for Simulating Heat Loss During Compression and the Delay Period in RCM Experiments. *Combustion and Flame*, 159(12), 3476–3492.
- [Kobori, S., & Kamimoto, T. , 1995]. Development of a Rapid Compression-Expansion Machine Simulating Diesel Combustion. *SAE Technical Papers*, 952514, 14.
- [Mehl, M., Curran, H. J., Pitz, W. J., & Westbrook, C. K. , 2009]. Chemical kinetic modeling of component mixtures relevant to gasoline.
- [Minetti, R., Carlier, M., Ribaucour, M., Therssen, E., & Sochet, L. R. , 1996]. Comparison of Oxidation and Autoignition of the Two Primary Reference Fuels by Rapid Compression. *Symposium (International) on Combustion*, 26, 747–753.
- [Mittal, G. , 2006]. A Rapid Compression Machine – Design, Characterization, and Autoignition Investigations, 198.
- [Mittal, G., & Chomier, M. , 2014]. Interpretation of Experimental Data from Rapid Compression Machines Without Creviced Pistons. *Combustion and Flame*, 161(1), 75–83.

- [Mittal, G., & Gupta, S. , 2012]. Computational Assessment of an Approach for Implementing Crevice Containment in Rapid Compression Machines. *Fuel*, 102, 536–544.
- [Mittal, G., Raju, M. P., & Sung, C. J. , 2008]. Computational Fluid Dynamics Modeling of Hydrogen Ignition in a Rapid Compression Machine. *Combustion and Flame*, 155(3), 417–428.
- [Mittal, G., Raju, M. P., & Sung, C. J. , 2010]. CFD Modeling of Two-Stage Ignition in a Rapid Compression Machine: Assessment of Zero-Dimensional Approach. *Combustion and Flame*, 157(7), 1316–1324.
- [Mittal, G., & Sung, C. J. , 2006]. Aerodynamics Inside a Rapid Compression Machine. *Combustion and Flame*, 145(1-2), 160–180.
- [Mittal, G., & Sung, C.-J. , 2007]. A Rapid Compression Machine for Chemical Kinetics Studies At Elevated Pressures and Temperatures. *Combustion Science and Technology*, 179(3), 497–530.
- [Norton, R. L. , 2009]. *Cam Design and Manufacturing Handbook* (2nd ed.). New York, NY: Industrial Press, Inc.
- [Park, J. W., Huh, K. Y., & Park, K. H. , 2000]. Experimental Study on the Combustion Characteristics of Emulsified Diesel in a RCEM. *Seoul 2000 FISITA World Automotive Congress*, (6), 1–6.
- [Ribaucour, M., Minetti, R., Carlier, M., & Sochet, L. R. , 1992]. Autoinflammation à haute pression. Conception, réalisation et test d'une machine à compression rapide. *Journal de Chimie Physique*.
- [Strozzi, C., Sotton, J., Mura, A., & Bellenoue, M. , 2009]. Characterization of a Two-Dimensional Temperature Field within a Rapid Compression Machine Using a Toluene Planar Laser-Induced Fluorescence Imaging Technique. *Measurement Science and Technology*, 20, 125403.
- [Sung, C.-J., & Curran, H. J. , 2014]. Using Rapid Compression Machines for Chemical Kinetics Studies. *Progress in Energy and Combustion Science*, 44, 1–18.
- [Tanaka, S., Ayala, F., & Keck, J. C. , 2003]. A Reduced Chemical Kinetic Model for HCCI Combustion of Primary Reference Fuels in a Rapid Compression Machine. *Combustion and Flame*, 133(4), 467–481.
- [Tsurushima, T. , 2009]. A New Skeletal PRF Kinetic Model for HCCI Combustion. *Proceedings of the Combustion Institute*, 32(2), 2835–2841.
- [Würmel, J., & Simmie, J. M. , 2005]. CFD Studies of a Twin-Piston Rapid Compression Machine. *Combustion and Flame*, 141(4), 417–430.

Appendix A: RCCEM Numerical Model

```

%%%%%%%%%%
%% RCCEM Operating Model
% Created on: 1/27/2014
% Updates
% 2/18/2014- Added Vent to add to braking
% 2/19/2014- Added Vent to Oil Pressure
% 2/25/2014- Changed Fall Profile to Linear Expansion
% 2/28/2015- Weibe Function working
% Author: John Neuman
format shortG
clc, clear all

%%%%%%%%%%
%% Constants
h1=8;           % Cam Height
Beta1=10.905;  % Half of the cam stroke (in)
L=21.81;       % Cam Linear length (in)
Lp=27.91;      % Cam follower path length (in)
mass=78/386;   % Mass of cam and piston assembly (lbm*in/s^2)
c_mass=47/386; % Mass of the cam.

% Fluid/Thermodynamic Properties
gamma_air=1.4; % Ratio of Specific Heats
B=232060;     % Modulus of Oil (psi)
rho=0.03145;  % Density of Oil (lb/in^3)
nu=0.0651;    % Kinematic Viscosity of Oil (in^2/s)
R=640.0512;   % psia-in^3/lbm-R
Z=0.9986;     % Air Compressibility Factor

%%%%%%%%%%
%% Inputs
% Ratio of Specific Heats
gamma=1.374;
% Expansion Height
h2=0.3;
% Air Cylinder Initial Driving Pressure (psi)
Pair(1)=60;
Driving_Pressure=Pair(1)
% Air Cylinder Temperature in Rankine
Tair(1)=532;
% Initial Pressure in the Combustion Chamber (psi)

```

```

Pc(1)=14.7;
% Combustion Chamber Initial Temperature
Tc(1)=532;
% Hydraulic Cylinder Step Diameters
dhyd2=3.75;    % First Step Diameter of Hydraulic Cylinder (in)
dhyd3=3.6;    % Second Step Diameter of Hydraulic Cylinder (in)
dhyd4=3.6;    % Third Step Diameter of Hydraulic Cylinder (in)
% Distance from Origin of the Cylinder Steps (in)
Lwd1=11.7;    % Length of open diameter in Hydraulic Cylinder (in)
Lwd2=11.4;
Lwd3=Lwd2;
Lwd4=.630;
% Coefficient of Discharge For Each Step Size (correlated)
Cdn=[.3 .4 .4 .45 .25 .25 .25 .25 .25];

%%%%%%%%%%%%%%%%%%%%%%%%%%%%%%%%%%%%%%%%%%%%%%%%%%%%%%%%%%%%%%%%%%%%%%%%%%
%%%%%%%%%%%%%%%%%%%%%%%%%%%%%%%%%%%%%%%%%%%%%%%%%%%%%%%%%%%%%%%%%%%%%%%%%%
%% Geometry
% Combustion Chamber
Lc=8.875;      % Initial Clearance Length (in)
dc=2;         % Diameter of Combustion Chamber (in)
Ag=pi*(dc^2)/4; % Area of Combustion Chamber (in^2)

% Air Cylinder
dair=6;       % Diameter of Air Cylinder (in)
din=3;
Aair=pi*(dair^2)/4; % Area of Air Cylinder (in^2)

% Air Cylinder Vent (Unused)
dvent=.75;
Across_75=pi*(dvent^2)/4; % Cross Section of Vent
C_75=50;

% Hydraulic Cylinder
dhyd=4;       % Initial Diameter of Hydraulic Cylinder(in)
dhyd_avg=(dhyd+dhyd2+dhyd3+dhyd4)/4;
dhyd5=3.57;
dhydp=3.203; % Piston Groove Outside Diameter (in)

% Area of oil acting on Hydraulic Piston steps (in^2)
Aoil=pi*(dhyd^2)/4;
Aoil2=pi*(dhyd2^2)/4;
Aoil3=pi*(dhyd3^2)/4;
Aoil4=pi*(dhyd4^2)/4;
% Aoil5=pi*(dhyd5^2)/4;

```

```

Ain=(pi*1.94^2/4);          % Area inside stopping ring groove
Aoilpg=(pi*(dhydp2)/4)-Ain; % Area of the hydraulic piston groove

% Hydraulic Piston
dhp=3.5;rhp=dhp/2;          % O.D. of Hydraulic Piston (in)
Aface=pi*(dhp^2)/4;        % Area of the Hydraulic Piston Face (in^2)
Ao=(pi*(dhyd^2)/4)-Aface;  % Area of the Oil Outlet (in^2)

% Diameters of the Piston Steps (in)
d4=3.124;r4=d4/2;
d3=3.154;r3=d3/2;
d2=3.174;r2=d2/2;
d1=3.194;r1=d1/2;

% Piston Step Areas (in^2)
A4((((d4^2)/4)*pi)-Ain;
A3((((d3^2)/4)*pi)-Ain;
A2((((d2^2)/4)*pi)-Ain;
A1((((d1^2)/4)*pi)-Ain;

% Length of the Piston Steps (in)
L1=0.893;
L2=0.551;
L3=0.433;
L4=0.314;

% Hydraulic Oil Venting (Unused)
Lwh=9.500;
Cd_oil=0.62;
dvent_oil=0.375;
B_oil=dvent/dhyd_avg;
C=(Cd_oil/sqrt(1-B_oil^4));
A_oil_orifice=pi*(dvent_oil^2)/4;
Poil_o=14.7;

%%%%%%%%%%%%%%%%%%%%%%%%%%%%%%%%%%%%%%%%%%%%%%%%%%%%%%%%%%%%%%%%%%%%%%%%%%
%%
%% Initial Conditions
%% Time Step
dt=10^-6;
tim(1)=0;

% Motion I.C.'s
a(1)=0;
v(1)=0;
Dist(1)=0;

```

```

% Cam Follower Trajectory and Velocity Initial Conditions
Rp=Lp/(2*pi);      % Prime Radius (in) for Cam Motion Calculations
srfd(1)=0;        % Cam follower initial position
vrfd(1)=0;        % Cam follower initial velocity
PHI(1)=0;         % Cam follower initial pressure angle

% Pressure I.C.'s
dp_air(1)=0;      % Initial differential pressure of the air cylinder
Pair_o=14.7;     % Initial pressure in front of air cylinder
Po=14.7;         % Back Pressure of the hydraulic cylinder (psi)

dpdt(1)=0;       % Initial differential pressure of hydraulic chamber
P(1)=580;        % Initial Oil Pressure in front of piston (psi)

% Force I.C.'s
F1(1)=Pair(1)*Aair;
F2(1)=0;
F3(1)=P(1)*Aface;

% Volume I.C.'s
Vair(1)=13860;
Vg(1)=Ag*Lc;
Voil(1)=Aoil*L;

% Air Temperature
mair(1)=(Pair(1)*Vair(1))/(R*Tair(1));
dmdt_air(1)=0;

% Fall Profile Linear
m=h2/Beta1;

% Weibe Function
nw=3;
aw=5;
tims=0.09;
timd=.005;

Qin=20000*.05; % 20,000 BTU/lbm * Fuel Mass Gasoline
xb(1)=0;
dPcdt(1)=0;
% dQcdt(1)=0;

t=2;

```



```

%%%%%%%%%%%%%%%%%%%%%%%%%%%%%%%%%%%%%%%%%%%%%%%%%%%%%%%%%%%%%%%%%%%%%%%%
%%
%% Air Cylinder
% Calculate the Volume of the air cylinder as dependent on the
% force balance as a function of time.

% Adiabatic Expansion for the air cylinder pressure
Vair(t)=Vair(t-1)+(Aair*((Dist(t))-Dist(t-1)));
Pair(t)= (Pair(t-1)*((Vair(t-1)/Vair(t))gamma_air)-(dp_air(t-1));

Tair(t)=Tair(t-1)*((Pair(t)/(Pair(t-1)))((gamma_air-1)/gamma_air));

mair(t)=mair(t-1)+dmdt_air(t-1)*dt;
rho_air(t)=mair(t)/Vair(t);
%%%%%%%%%%%%%%%%%%%%%%%%%%%%%%%%%%%%%%%%%%%%%%%%%%%%%%%%%%%%%%%%%%%%%%%%
%%
%% Air Vent Model (Unused)
% Loop to model the effect of an air vent on the driving side of the
% air cylinder
if Dist(t)<L-(Lwd1) % Vent is closed to start with and through compression
    dmdt_air(t)=0;
    dp_air1(t)=0;
    dp_air2(t)=0;
    dp_air3(t)=0;
    dp_air(t)=0;
% elseif Dist(t)>=L-(Lwd1) & Dist(t)<=L-Lwd4
% % Calculate Mass Flow rate of the air as the vent is opened
%
dmdt_air(t)=C_75*Across_75*sqrt((2*rho_air(t)*386*(gamma_air/(gamma_air-
1))*(((Pair_o/Pair(t))(2/gamma_air))-(Pair_o/Pair(t))((gamma_air+1)/gamma_air))/(1-
(Pair_o/Pair(t))))*(Pair(t)-Pair_o));
% % Calculate the Pressure drop due to Mass flowing out of the
% % vent
% dp_air1(t)=(((R*Tair(t))/Vair(t))*dmdt_air(t)*dt);
% dp_air2(t)=((Pair(t)/Vair(t))*(Vair(t)-Vair(t-1)));
% dp_air3(t)=(Pair(t)*Tair(t))*((Tair(t-1)-Tair(t))/Tair(t)2);
% dp_air(t)=dp_air1(t)-dp_air2(t)-dp_air3(t);
else % Simulates the vent is closed outside of the range above
    dmdt_air(t)=0;
    dp_air1(t)=0;
    dp_air2(t)=0;
    dp_air3(t)=0;
    dp_air(t)=0;
end

```

```

%%%%%%%%%%
%%
%% Oil Vent (Unused)
%   Loop to account for a vent of the Oil Pressure behind the hydraulic
%   piston to allow for faster expansion
%   if P(t-1)<=Poil_o
%       P(t-1)=Poil_o;
%       Poil_o=.85*P(t-1);
%   end
%   if Dist(t)==0
%       V_dot_oil(t)=0;
%   elseif Dist(t)>=0.01 & Dist(t)<=L-.630
%       V_dot_oil(t)=C*A_oil_orifice*sqrt((2*386*(P(t-1)-Poil_o)/rho));
%   else
%       V_dot_oil(t)=0;
%   end
%%%%%%%%%%
%%
%% Combustion Chamber
% Calculation of the Volume of the Combustion Chamber
%   Vg(t)=(Lc-srfd(t))*Ag;

% Calculation of the Combustion chamber Pressure (Adiabatic Compression)
%   if tim(t)<tims
%       xb(t)=0;
%       dQcdt(t)=0;
%   elseif tim(t)>=tims & tim(t)<=timd+tims
%       xb(t)=1-exp(-aw*((tim(t-1)-tims)/timd)^nw);
%       dQcdt(t)=(nw*aw*Qin/timd)*(1-xb(t))*((tim(t-1)-tims)/timd)^(nw-1); % Units are
BTU/s
%   else
%       xb(t)=1;
%       dQcdt(t)=0;
%   end
%   xb(t)=1-exp(-aw*((tim(t)-tims)/timd)^nw);
% Combustion Chamber Pressure
%   Pc(t)=Pc(t-1)+(dPcdt(t-1)*dt);
%   dPcdt(t)=(-gamma*(Pc(t)/Vg(t))*((Vg(t)-Vg(t-1))/dt)+(((gamma-
1)/Vg(t))*(5.40395*dQcdt(t-1))); % Conversion: 5.40395 psi-ft^3/BTU [overall units are
in PSI/s]

%   Pc(t)=Pc(t-1)*((Vg(t-1)/Vg(t))^gamma;
% Combustion Chamber Temperature
%   Tc(t)=Tc(t-1)*(((Pc(t))*Vg(t))/(Pc(t-1)*Vg(t-1)));
%%%%%%%%%%
%%

```

```

%% Hydraulic Cylinder
% If loop sets the position data for characteristics of the hydraulic
% cylinder during the stroke of the system
if Dist(t)<L-Lwd1;
    n=1;
    Cd=Cdn(n);
    Ao=Aoil-Aface;
    Voil(t)=(Aoil*(L-Dist(t)))+(V_dot_oil(t)*dt);
    Aoil=Aoil;
    length = 1.063;
elseif Dist(t)>=L-Lwd1 & Dist(t)<L-Lwd2;
    n=2;
    Cd=Cdn(n);
    Ao=Aoil2-Aface;
    Voil(t)=(Aoil2*(L-Dist(t)))+(V_dot_oil(t)*dt);
    Aoil=Aoil2;
    length = 1.063;
elseif Dist(t)>=L-Lwd2 & Dist(t)<L-Lwd3;
    n=3;
    Cd=Cdn(n);
    Ao=Aoil3-Aface;
    Voil(t)=(Aoil3*(L-Dist(t)))+(V_dot_oil(t)*dt);
    Aoil=Aoil3;
    length = 1.063;
elseif Dist(t)>=L-Lwd3 & Dist(t)<L-Lwd4;
    n=4;
    Cd=Cdn(n);
    Ao=Aoil4-Aface;
    Voil(t)=(Aoil4*(L-Dist(t)))+(V_dot_oil(t)*dt);
    Aoil=Aoil4;
    length = 1.063;
elseif Dist(t)>=L-Lwd4 & Dist(t)<L-L1;
    n=5;
    Cd=Cdn(n);
    Ao=Aoil4-Aface;
    Voil(t)=(Aoil4*(L-Dist(t)))+(V_dot_oil(t)*dt);
    Aoil=Aoil4;
    length = 0.893;
elseif Dist(t)>=L-L1 & Dist(t)<L-L2
    n=6;
    Cd=Cdn(n);
    Ao=Aoilpg-A4;
    Voil(t)=(Aoilpg*(L-Dist(t)))+(V_dot_oil(t)*dt);
    Aoil=Aoilpg;
    length = 0.551;
elseif Dist(t)>=L-L2 & Dist(t)<L-L3;

```

```

n=7;
Cd=Cdn(n);
Ao=Aoilpg-A3;
Voil(t)=(Aoilpg*(L-Dist(t)))+(V_dot_oil(t)*dt);
Aoil=Aoilpg;
length = 0.433;
elseif Dist(t)>=L-L3 & Dist(t)<L-L4;
n=8;
Cd=Cdn(n);
Ao=Aoilpg-A2;
Voil(t)=(Aoilpg*(L-Dist(t)))+(V_dot_oil(t)*dt);
Aoil=Aoilpg;
length = 0.314;
else
n=9;
Cd=Cdn(n);
Ao=Aoilpg-A1;
Voil(t)=(Aoilpg*(L-Dist(t)))+(V_dot_oil(t)*dt);
length=0.314;
Aoil=Aoilpg;
end

%%%%%%%%%%%%%%%%%%%%%%%%%%%%%%%%%%%%%%%%%%%%%%%%%%%%%%%%%%%%%%%%%%%%%%%%%%%%%%
%% %
T1(t)=((( -1*B*Cd*Ao)*(sqrt(((386*2*(P(t-1)-Po))/rho))))/Voil(t));
T2(t)=(B*Aface*(v(t))/Voil(t));
dpdt(t)=T1(t)+T2(t);
P(t)=P(t-1)+((dpdt(t))*dt);
del_P(t)=P(t-1)-Po;

% Pressure correction to avoid problems initially in the oil pressure due
% to dividing by zero
if P(t)<=Po
P(t)=Po;
Po=.9*P(t);
end
t=t+1;
end
% Static Equilibrium oil pressure at the initial state.
P(1)=((Pair(1)*Air)-(Pc(1)*Ag*tan(PHI(1))))/Aface;

```

Appendix B: CFD Simulation Ignition Delay Time Script

```
#!/usr/bin/python
# A Script to Determine the Ignition Delay Time, Compressed Temperature, and
Compressed
# Pressure for a group of Simulations
# Author: John Neuman
import os
import numpy as np
import glob

# Point to the folder containing the simulations:
head_dir=r'Z:\Converge_CFD\PRF65_Transient\Crevice_Piston'
os.chdir(head_dir)
# Point to the folder you would like to write the data out to:
out_dir=r'C:\Users\2554neumanj\Documents\Ignition_Delay_Data\PRF65_Crevice\1-22-
15'
out_file_name=r'Ignition_Delay_1-20-15.txt'
if os.path.exists(out_dir):
    print('Path Exists!')
else:
    os.mkdir(out_dir) # Make the output directory to store the data in.

# Create Summary Data File and Write Header Lines:
header='File Name:\t 1000/T [1000/K] \t Tao[ms] \t P_c [bar] \t Tao1[ms] \n'
if os.path.exists(out_dir+'\\'+out_file_name):
    out2=open(out_dir+'\\'+out_file_name,'a')
else:
    out2=open(out_dir+'\\'+out_file_name,'w')
    out2.writelines(header)
out2.close()

# Loop through all of the simulation directories:
for p_directory in glob.glob('CR*'):
    os.chdir(head_dir+'\\'+p_directory)
    print(p_directory)
    # For each directory in the head CR directory we would like to pull out
thermo.out data
    # and put it inside a new file of the same name _data.txt
    for directory in glob.glob('CR*'):
        os.chdir(head_dir+'\\'+p_directory+'\\'+directory)
        conv_done=head_dir+'\\'+p_directory+'\\'+directory+r'\\converge.done'
        print(directory)
        if os.path.exists(conv_done):
            input_file=head_dir+'\\'+p_directory+'\\'+directory+r'\\thermo.out'
```

```

if os.path.exists(input_file):
    output_file=out_dir+'\\'+directory+'_data.txt'
    if os.path.exists(output_file)==False:
        with open(input_file,'r') as i:
            data=i.readlines()[4:]
            for k in range(len(data)):
                out=data[k].split()
                tim=out[0]
                press=out[1]
                maxT=out[5]

                data[k]= tim+' '+press+'

'+maxT+'\n'

                o=open(output_file,'w')
                o.writelines(data)
                o.close()

# Once we have all of the pertinent data we need to operate on it to determine the
# ignition delay times:
os.chdir(out_dir) # Go into the directory that we created above.

# Loop through each file in the directory -there should be a file for each of the
# simulations:
for file in glob.glob('*_data.txt'):
    dPdt_out=[] # Initialize a numpy array for dPdt output data.
    file_i=out_dir+'\\'+file # Select the file.
    #print(file_i)
    # Load in the text files to calculate dPdt
    dt=np.loadtxt(file_i, usecols=[0])
    dP=np.loadtxt(file_i, usecols=[1])

    x=0
    # Loop through each line and write out the dPdt for that line in the numpy array.
    for x in range(len(dt)-1):
        dPdt=(dP[x+1]-dP[x])/(dt[x+1]-dt[x])
        x=x+1
        dPdt_out.append(dPdt)

# Open the data file created in the first loop above to get simulation information.
T=open(file_i,'r').readlines()
# Get information at TDC
if len(T)>=320:
    T1=T[320].split()
else:

```

```

    T1=T[-1].split()
# Pick off the Pressure and Temperature at TDC
T_TDC=1000/float(T1[2])
P_TDC=10*float(T1[1])

tao1=0.0
for j in range(322,550):
    if dPdt_out[j]>10:
        t_f1=T[j].split()
        t_f1=float(t_f1[0])
        tao1=1000*(t_f1-0.032)
        #print(file, tao1)
        break

tf=np.where(dPdt_out==dPdt.max()) # Picks out where max dPdt is
T_f=T[tf[0]+1].split() # Picks off the time at the location above
#print(T_f)

T_c=float(T_f[0]) # Float T_f for the time at Combustion

tao=1000*(T_c-0.032) # Total Ignition Delay

max_dPdt=dPdt.max()

output2=file+'t'+str(T_TDC)+'t'+str(tao)+'t'+str(P_TDC)+'t'+str(tao1)+'n'
#print(output2)

out3=open(out_dir+'\\'+out_file_name,'a')
out3.writelines(output2)
out3.close()

```

Appendix C: Script to Determine Ignition Delay Time from RCCEM Data

```

clear all, close all, clc
format shortG
filenames= uigetfile('*.txt','Multiselect','on');
% size(filenames,2)

if size(filenames,2) ~= 1 && size(filenames,2) ~= 18
    num_files = size(filenames,2);
else
    num_files = 1;
end

% Constants
p_i=1.1;
p_o=[p_i p_i p_i p_i p_i p_i];      % initial pressure [bar]
dt=1/100000;                        % time step
mu=10;
comp=13650;
post_ign=1000;
tau1_int=9000;
max_length = 40000;
maximumPall=31;
k=1;
n=1;
for k=1:num_files
    clear Pc time_Pc maxP t_RiseP t_maxP RiseP
    if num_files == 1
        filename=filenames
    else
        filename=filenames{k}
    end

    A=dlmread(filename,'\t');
    A=moving(A(:,1),23);
    minA=min(A(:,1));
    [maxP,t_maxP] = max(A(:,1));
    [Pc,t_Pc] = max(A(1:comp,1));

    [RiseP] = find(A(:,1) < 0.125);
    [HalfPc] = find(A(:,1) > 0.5*Pc);

```

```

sub = 1000;

if maxP < maximumPall/mu
    t1 = RiseP(end-sub):1:max_length-RiseP(end-sub);
    t1 = t1*dt*1000; %[ms]
    time_Pc = t_Pc*dt*1000; %[ms]
    t_RiseP = RiseP(end-sub)*dt*1000;%[ms]
    plot(t1-time_Pc,mu*(A(RiseP(end-sub):max_length-RiseP(end-sub),1)-
minA)+p_o(n),'LineWidth',2), hold all

% Calculate Pressure Drop Rate for non-reactive experiments
check = mu*A(max_length,1);
check2 = dt*1000*(t_Pc-max_length);
dpdt = (mu*(Pc-A(max_length,1)))/(dt*1000*(t_Pc-max_length));
Compressed_Press(k,5) = mu*A(max_length)+p_o(n);
Compressed_Press(k,6)= dpdt;

else

    t1 = RiseP(end-sub):1:t_maxP+post_ign;
    t1 = t1*dt*1000; %[ms]
    time_Pc = t_Pc*dt*1000; %[ms]
    t_RiseP = RiseP(end-sub)*dt*1000;%[ms]

%#####
#####
% The following can be used to calculate the ignition delay times:
%   for j = 1:t_maxP+post_ign
%       B(j)=(A(j+1)-A(j))/dt;
%   end
%
%   B=moving(B(:),347);
%   figure (1)
%   plot(t1-time_Pc,B(RiseP(end-sub):t_maxP+post_ign)), hold all
% %   axis([0 20 0 1200])
%   axis tight
%   [tau1_max,t_tau1]= max(B(t_Pc:t_Pc+tau1_int));
%   [tau2_max,t_tau2]= max(B(t_Pc:length(B)));
%   tau(k,1)= t_tau1*dt*1000;
%   tau(k,2)= t_tau2*dt*1000;
%   figure(3)
%   plot(B)

```

```

% figure(2)
%#####
#####
    plot(t1-time_Pc,mu*(A(RiseP(end-sub):t_maxP+post_ign,1)-
minA)+p_o(n),'LineWidth',2), hold all
    end

    Compressed_Press(k,1) = t_Pc*dt*1000-t_RiseP;    % Compression Time
    Compressed_Press(k,2) = (t_Pc-HalfPc(1))*dt*1000; % Time 1/2 Pc
    Compressed_Press(k,3) = p_o(n);    % Initial Pressure
    Compressed_Press(k,4) = mu*Pc+p_o(n); % Pressure at TDC
    n=n+1;
end

% Create xlabel
xlabel('Time [ms]','FontWeight','bold','FontSize',11,'FontName','Times');
% Create ylabel
ylabel('CC Pressure [bar]','FontWeight','bold','FontSize',11,'FontName','Times New
Roman');
set(gca,'FontSize',11,'FontName','Times New Roman');

% axis([0 70 0 65])
axis tight
% legend('\phi = 1.0','\phi = 0.9','\phi = 0.8', '\phi = 0.7','\phi = 0.55','Non-Reactive',
'location','best')
% legend('Model','RCCEM')
Compressed_Press = Compressed_Press
% tau = tau
% dlmwrite('press_drop.txt',Compressed_Press, 't')

```